

Technical University of Denmark



Segmentation-Driven Tomographic Reconstruction.

Kongskov, Rasmus Dalgas; Dong, Yiqiu; Knudsen, Kim

Publication date:
2018

Document Version
Publisher's PDF, also known as Version of record

[Link back to DTU Orbit](#)

Citation (APA):
Kongskov, R. D., Dong, Y., & Knudsen, K. (2018). Segmentation-Driven Tomographic Reconstruction. Technical University of Denmark (DTU). (DTU Compute PHD-2017, Vol. 457).

DTU Library
Technical Information Center of Denmark

General rights

Copyright and moral rights for the publications made accessible in the public portal are retained by the authors and/or other copyright owners and it is a condition of accessing publications that users recognise and abide by the legal requirements associated with these rights.

- Users may download and print one copy of any publication from the public portal for the purpose of private study or research.
- You may not further distribute the material or use it for any profit-making activity or commercial gain
- You may freely distribute the URL identifying the publication in the public portal

If you believe that this document breaches copyright please contact us providing details, and we will remove access to the work immediately and investigate your claim.

 **DTU Compute**
Department of Applied Mathematics and Computer Science

Segmentation-Driven Tomographic Reconstruction

Rasmus Dalgas Kongskov

Kongens Lyngby 2018



DTU Compute

Department of Applied Mathematics and Computer Science

Technical University of Denmark

Matematiktorvet

Building 303B

2800 Kongens Lyngby, Denmark

Phone +45 4525 3031

compute@compute.dtu.dk

www.compute.dtu.dk

PHD-2017-457

ISSN: 0909-3192

Abstract

The tomographic reconstruction problem is concerned with creating a model of the interior of an object from some measured data, typically projections of the object. After reconstructing an object it is often desired to segment it, either automatically or manually. For computed tomography (CT), the classical reconstruction methods suffer from their inability to handle limited and/or corrupted data. For many analysis tasks computationally demanding segmentation methods are used to automatically segment an object, after using a simple reconstruction method as a first step.

In the literature, methods that completely combine reconstruction and segmentation have been suggested, but these are often non-convex and have very high computational demand. We propose to move the computational effort from the segmentation process to the reconstruction process, and instead design reconstruction methods such that the segmentation subsequently can be carried out by use of a simple segmentation method, for instance just a thresholding method.

We tested the advantages of going from a two-stage reconstruction method to a one-stage segmentation-driven reconstruction method for the phase contrast tomography reconstruction problem. The tests showed a clear improvement for realistic materials simulations and that the one-stage method was clearly more robust toward noise. The noise-robustness result could be a step toward making this method more applicable for lab-scale experiments.

We have introduced a segmentation-driven reconstruction method which incorporates information about the main texture direction in an object. We proved that this method has mathematically desirable properties such as being convex and lower semi-continuous. We have also demonstrated the practical applicability of the method

within image denoising, image deblurring and CT reconstruction. In order to use the proposed method we also proposed efficient and robust methods for estimating the main direction in either corrupted images or from limited and corrupted CT-projection data.

For directional object we also proposed two different reconstruction methods that separates the directional parts in the object from the non-directional parts. These method could for example be used for objects consisting of fibres and cracks. The results can be categorized as either completely combined reconstruction and segmentation of the object, or as highly supporting for the following segmentation process.

Computed tomography is used within medical diagnosis, food science, materials science, production inspection, quality assessment, etc. Segmentation-driven reconstruction methods can help to improve both manual and automated segmentation processes that are used to analyze an object after the scanning. The results in this thesis are both of theoretical interest within regularization theory and directly applicable for image denoising, image deblurring and surely within tomographic reconstruction.

Resumé

Det tomografiske rekonstruktionsproblem omhandler dannelse af en model der beskriver det indre af et objekt ud fra målte data, typisk projektioner af objektet. Efter rekonstruktion af et objekt er det ofte målet at segmentere det, enten automatisk eller manuelt. For computer tomografi (CT) lider de klassiske rekonstruktionsmetoder under deres manglende evne til at håndtere begrænsede og/eller beskadigede data. For mange analyse formål benyttes beregningstunge metoder til automatisk at segmentere et objekt, efter at en simpel rekonstruktionsmetode er brugt som første skridt.

I litteraturen er der foreslået metoder der fuldstændig kombinerer rekonstruktion af segmentering, men disse ofte ikke konvekse og er beregningsmæssigt krævende. Vi forslår at flytte den beregningsmæssige behov til rekonstruktionsmetoden således at den efterfølgende segmentering kan udføres ved brug af en simpel segmenteringsmetode, fx blot en tærskling(thresholding).

Vi har testet fordelene ved at gå fra en to-stadie rekonstruktionsmetode til en et-stadie segmentering-drevet rekonstruktionsmetode for det fase-kontrast tomografiske rekonstruktionsproblem. Testene viste en klar forbedring i forbindelse med realistiske materiale simuleringer og at et-stadie metode var klart mere robust i forhold til støj. Støjrobustheds-resultatet kan være et skridt i retningen af at gøre denne metode mere anvendelig et laboratorie-skala eksperimenter.

Vi har introduceret en segmenterings-drevet rekonstruktionsmetode der inkorporerer information om et objekts tekstur-retning. Vi har bevist at denne metode har eftertragtede matematiske egenskaber såsom konveksitet og lower semi-continuity. Vi har også demonstreret den praktiske anvendelighed af metoden indenfor billed-denoising, billed-deblurring og CT-rekonstruktion. For at kunne benytte den fores-

låde metode har vi også foreslået effektive og robuste metoder til at estimere den dominerende retning i enten beskadigede billeder eller fra begrænsede og beskadigede CT-projektionsdata.

For retningsbestemte objekter har vi også foreslået to forskellige rekonstruktionsmetoder der separerer de retningsbestemte dele i objektet fra de ikke-retningsbestemte dele. Disse metoder kunne for eksempel bruges på objekter bestående af fibre med sprækker. Resultaterne kan enten kategoriseres som komplet kombineret rekonstruktion og segmentering af objektet, eller som væsentligt forberedende i forhold til den efterfølgende segmenterings process.

Computer tomografi bliver brugt til medicinske diagnoser, fødevarevidenskab, materialevidenskab, produktionsinspektion, kvalitetsvurdering, osv. Segmenterings-drevne rekonstruktionsmetoder kan hjælpe med at forbedre både manuelle og automatiske segmenteringsprocesser der benyttes til at analysere et objekt efter skanning. Resultaterne i denne afhandling er både teoretisk interessante indenfor regulariseringsteori og direkte anvendelige indenfor billed-denoising, billed-deblurring og naturligvis indenfor tomografisk rekonstruktion.

Preface

This thesis was prepared in partial fulfilment of the requirements for acquiring the PhD degree at the Technical University of Denmark (DTU). The work was carried out from September 2014 to August 2017 at the Section for Scientific Computing at the Department of Applied Mathematics and Computer Science under the supervision of Associate Professor Yiqiu Dong and Associate Professor Kim Knudsen.

From January 2016 to May 2016, the project was carried out at Institute for Mathematics and Scientific Computing, University of Graz. This visit was hosted by Univ.-Prof. Dr. Kristian Bredies, and partially sponsored by the Otto Mønsted foundation for which I am grateful.

This work was part of the project HD-Tomo funded by Advanced Grant No. 291405 from the European Research Council.

Kongens Lyngby, February 6, 2018

A handwritten signature in black ink, appearing to read 'RDK' with a stylized flourish at the end.

Rasmus Dalgas Kongskov

Acknowledgements

The three years work of this PhD thesis has not been carried out alone and I have a series of people to thank who participated in the work, who helped and inspired me, and who supported me throughout the project.

First I would like to thank my supervisors Yiqiu Dong and Kim Knudsen for guiding and supporting me, and for all the collaborative work we have done together. I would like to thank Per Christian Hansen and all of the current and past members of the HD-Tomo and the Hybrid-tomography groups. I learned many things from all of the members and their different projects, and from the many seminars that we have had. I will especially like to thank Jakob S. Jørgensen, Henrik Garde, Adrian Kirkeby, Federica Sciacchitano, Martin S. Andersen, Ekaterina (Katja) Sherina, Hari Om Agrawal and Marie F. Schmidt from whom I have learned a lot. I will also like to thank Jürgen Friel, Dimitri Boiroux, Stratos Staboulis, Martin Kjer, Morten Hagedrup, Lauri Harhanen, Sara Soltani, Mikhail (Mike) Romanov, Sazuan N. M. Azam, Bjørn C. S. Jensen, Kenan Sehic and Angeliki Xenaki.

I will like to thank the members of the two other CT-related projects in the Copenhagen area: CINEMA and P^3 , for their collaboration and sharing of material, problems and ideas. Furthermore I will like to thank the other employees from building 303 and all the other PhD's at the institute of Applied Mathematics and Computer Science that I met over these three years, for making DTU a nice place to work.

During my external stay in Graz, Austria, I was welcomed by Kristian Bredies and his excellent group: Martin Holler, Adrián Martín, David Vicente and Kamil S. Kazimierski. I am very grateful from all things I learned while I was visiting them.

I am also grateful to the Otto Mønsted Foundation for their financial support during

my external stay and conference trips.

Finally I will like to thank friends and family who have always been supportive and encouraging, which really has meant a lot to me. And above all I thank my girlfriend Sisse, who along this journey has also become my wife, for making every day better than the last, for always bringing back my positive mind and for reminding me about the most important things in life.

List of Symbols

I	Intensity of the X-ray source
f	continuous function
x	spatial coordinate
L	integration line CT
b	discrete sinogram with noise
\mathbf{b}	discrete sinogram with noise, on vector form
\mathcal{A}	continuous forward operator
g	continuous measured data
\mathcal{R}_T	Radon transform
M	pixels dimensions
N	sinogram dimensions
n	system matrix index (sinogram)
h	system matrix index (pixels)
a	system matrix element
A	system matrix or discrete linear operator
t	CT detector bin variable
ϕ	CT measurement angles
z	discrete function describing a functional parameter in an object
u, w	discrete function components for object splitting
\mathbf{z}	discrete function, on vector form
b	continuous function with noise
n_i	complex refractive index
β	absorption index

δ	refractive index decrement
B	absorption
ψ	phase shift
T	transmittance
P	Fresnel propagator
k	iteration number
\mathcal{R}	regularization operator
\mathcal{G}	data Fidelity term
λ	regularization parameter
\mathcal{J}	energy functional or objective function
∇	gradients operator
Ω	object or image domain
\mathbf{v}	dual function vector

Contents

Abstract	i
Resumé	iii
Preface	v
Acknowledgements	vii
List of Symbols	ix
Contents	xi
1 Introduction	1
2 Tomography	3
2.1 Computed tomography	4
2.2 Phase contrast tomography	7
2.3 Tomographic reconstruction	9
2.3.1 Filtered back-projection	9
2.3.2 Algebraic methods	10
2.3.3 Variational methods	10
2.3.4 Artifacts and noise	11
2.3.5 Picking a reconstruction method	12
3 Regularizing Inverse Problems	17
3.1 Inverse problems	17
3.2 Variational formulation with regularization	18

4	Numerical Aspects	25
4.1	Optimization	26
4.1.1	Requirements and choice of optimization method	26
4.1.2	Regularization parameter and stopping criteria	27
4.1.3	Implementation	28
4.2	Simulated experiments and quantification	29
5	Segmentation-Driven Reconstruction Methods	33
5.1	Image segmentation	34
5.1.1	Requirements	35
5.2	Combined methods	35
5.3	Aiding segmentation	36
6	Contributions	37
6.1	Phase contrast tomography	38
6.1.1	Context	38
6.1.2	Relevant paper	39
6.1.3	Outcome	39
6.2	Directional total generalized variation	40
6.2.1	Context	40
6.2.2	Relevant papers	40
6.2.3	Outcome	41
6.3	Tomographic reconstruction of directional objects	42
6.3.1	Context	42
6.3.2	Relevant paper	43
6.3.3	Outcome	43
7	Conclusions and Perspectives	47
A	Noise robustness of a combined phase retrieval and reconstruction method for phase-contrast tomography	49
B	Directional Total Generalized Variation Regularization	59
C	Directional Total Generalized Variation Regularization for Impulse Noise Removal	87
D	Tomographic Reconstruction Methods for Decomposing Directional Components	99
	Bibliography	115

CHAPTER 1

Introduction

The field tomography covers a wide range of methods for non-invasively investigating the interior of objects. Opposed to methods that are just based on analyzing single measurements or projections, the tomography methods tries to create a model of the interior by combining information from several measurements or projections. Within imaging, tomography has a long history, especially due to the very widely used computed tomography (CT). In this thesis, the work is mainly concerned two tomography techniques that are very similar, from a measurement set-up perspective, namely: CT and free-space propagation phase contrast tomography (PCT).

The process of calculating the interior from a set of measurements is usually called a reconstruction. For CT and PCT the most widely used 2D reconstruction method is a filtering method called *filtered back-projection* (FBP). This method well-studied, and it is efficient and reliable when sufficient data, that is not corrupted by noise and artifacts, is collected. Whenever the measured data is limited or corrupted, the filtering methods gives results that can be heavily deteriorated. Other reconstruction method that has been used a lot for CT reconstruction are the so called algebraic methods that basically tries to solve the problem as an algebraic system of linear equations. The tomographic reconstruction problem is fact part of a much larger class of problems called *inverse problems*. A lot of theory has been developed within the field of inverse problems, and since the CT reconstruction problem is a linear inverse problem, many solution strategies from this field can directly applied and further developed.

Throughout the last few decades well-established mathematical theory has been developed within the field of inverse problems. An inverse problem is said to be *ill-posed* if existence, uniqueness or stability cannot be shown for the solution of the problem.

The CT-reconstruction problem is a mildly ill-posed problem. For ill-posed problems we have to design solution strategies that can overcome the effects of ill-posedness, if we want to get meaningful results. One widely used way to solve ill-posed inverse problems is to use variational methods with regularization.

In the inverse problems community two regularization methods are particularly well-known: *Tikhonov* regularization and *Total Variation* regularization. Tikhonov regularization was the first regularization method to be widely used and studied. Total variation regularization has become a go-to standard for imaging and image processing since it is very good at removing noise, while still preserving edges, which are two highly desirable features for images. A typical rule for choosing a suitable regularization method is to choose it based on what prior we expect the object to follow.

Image segmentation is the task of separating an image into regions of different classes. Automated segmentation, using computational methods, is frequently used as post-processing within imaging. Such segmentation methods can either be very simple or highly computationally demanding. In this work the aim is to use the computational for image reconstruction or image restoration, rather than using it on segmentation. In order to do so we have developed and tested a series of methods, that like total variation, produces solutions that ease a subsequent segmentation process, i.e. *segmentation-driven methods*.

This PhD thesis is mainly based on scientific articles published, submitted or going to be submitted to peer-review journals or proceedings. The full-length of these articles can be found in the appendix of this thesis. The rest of the thesis is organized as follows: In [Chapter 2](#) I review tomography, CT and PCT in greater details. Reconstruction methods their advantages and disadvantages are also presented. In [Chapter 3](#) a deeper look into inverse problems, and the use of variational methods for solving them, is given. Some different classical regularization methods are presented together with their respective priors. After this brief introduction to variational methods, I give an overview of the numerical aspects for solving such problems in [Chapter 4](#). In [Chapter 5](#) I review classical and more recent segmentation methods. In this chapter desired features for segmentation is outlined and the idea of aiding a subsequent segmentation process, through the choice of a reconstruction method, is outlined in more details. After having established all of these different aspects that relates to segmentation-driven tomographic reconstruction methods, I review the work from the enclosed papers in [Chapter 6](#). Finally I briefly sum up the main conclusions of this thesis and look at the future perspectives of our work.

The notation in the papers might differ from the notation in the chapters of this thesis. This is due to a goal of having a unified notation in the thesis chapters, where the papers are just sought to be self-contained.

CHAPTER 2

Tomography

Imaging science covers a wide variety of techniques for non-invasive investigation of the interior of objects. Tomography is an imaging technique that encompasses methods where measurements are taken in slices or sections. For some technologies, such as X-ray computed tomography, each slice or projection could be used for analysis solely, but the target for a tomographic technique is to combine information from several measured sections. From the combined measured data, the target is to recreate the object of interest and its interior, such that it can be analyzed.

The list of different tomographic methods is too comprehensive to outline it in its entirety here, but I highlight some of the most well-established techniques instead. In [Table 2.1](#), there is a list of some tomography technologies and their electromagnetic sources. Beside these, classical ultrasound and Magnetic Resonance Imaging (MRI) should be mentioned as some of the most popular imaging methods, though these are not tomographic. Each of these imaging modalities have their application that justifies them and no method is superior for every task, although the modalities do overlap for some tasks.

Tomographic imaging techniques are highly popular due to their non-invasive nature, which is why they are now incorporated in conventional medical equipment all over the world at hospitals, at dentists, etc. Besides usage in the medical industry, tomographic methods are used for geophysical and seismic imaging, chemical imaging, archaeology, paleontology, materials science, in the production industry in general, e.g. in metrology or for failure and flaw detection, and within many other areas.

In our work we have focused on X-ray Computed Tomography (CT) and a Phase Contrast Tomography (PCT) method which is highly related to CT. Furthermore

the objects that are used as examples are all inspired by materials science. Much more on the use of tomography in materials science analysis can be found in [7].

Technology	Source
Computed Tomography (CT)	X-rays
Electrical Impedance Tomography (EIT)	Electrical current
Ultrasound Tomography (UST)	Ultrasound waves
Positron Emission Tomography (PET)	Positrons
Single-Photon Emission Tomography (SPECT)	Gamma rays
Seismic Tomography	Seismic waves
Optical Tomography	Light waves
Electron Tomography	Electron beam
Acoustic Tomography	Sound waves
Photoacoustic Tomography (PAT)	Laser
Thermoacoustic Tomography (TAT)	Radio waves

Table 2.1: Some tomography technologies and their respective sources.

2.1 Computed tomography

Computed Tomography (CT) was pioneered by G. Hounsfield and A. M. Cormack in the 60's. The first X-ray CT scan was carried out in 1969 by Hounsfield [20], followed by the first clinical scans in 1972. Since the first CT scanner the methodology has developed into a range of different scanner setups. Common for all of the scanners is the presence of an X-ray source, a detector, and some sort of rotation either of the object or of the source and detector. Due to the rotational scanning, the domain covered by the scanner will be circular, spherical, or cylindrical.

The first types of CT scanners are often referred to as *pencil beam* since they consist of a single X-ray source that emits a narrow beam and a single detector placed opposite to the source. The source and the detector are translated simultaneously along parallel lines, tangent to the circular domain. This series of parallel measurements are carried out for each discrete measurement angle, until a complete 180° rotation is reached. The method is mostly related to 2D scanning, though layered scans can be taken, thus making it a very cumbersome 3D method.

The *parallel beam* method is quite similar to the pencil beam method. For this method a series of sources and detectors are placed on opposite sides of the object and then rotated around the object. Therefore no translation is necessary, only the rotation. This method can both be a 2D and 3D method. A schematic drawing of source,

detectors, and the circular domain for the 2D version can be seen in [Figure 2.1](#). The 2D parallel beam method will be the method that I consider in this thesis. In paper [A](#) and [D](#) the parallel beam methods is also what is used.

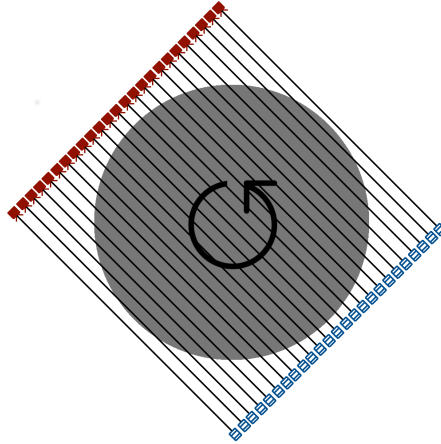


Figure 2.1: Schematic of the 2D parallel beam technology setup. Sources, detectors and circular domain.

Other scanning methods include the 2D *Fan Beam* method, where one source and a long array of detectors, in a line or an arch, is used. The *Cone Beam* and *Helical Beam* methods are purely 3D methods, hence the detector has a rectangular shape. For more on the different types of scanner technologies and their history see [\[20\]](#).

The use of CT in the medical industry has increased a lot over the last 20 years. An estimate from 2010 said 70 million annual scans in the US and an estimate from 2014 said 5 million annual scans in the UK with 10% annual increase, see [\[15\]](#) for more. There is no arguing that CT scanners are an enormous business within medical imaging. Within materials science research the use of CT has also been increasing over the last 20 years, especially due to the high quality scanning facilities called *synchrotrons*. At a synchrotron facility electrons are accelerated to a high speed, usually in a large ring, i.e. >10 m. The accelerated electrons are used to produce very high energy and highly coherent X-ray beams. This allows these facilities to scan materials which are not penetrable with a clinical CT setup. Furthermore synchrotrons can, opposed to standard hospital or lab-scale equipment, reach higher resolution, achieve a narrow energy spectrum and minimize the influence from scattering and other undesired physical effects.

Lambert-Beers law describes the attenuation of X-rays when they interact with matter if we only focus on the attenuation and disregard scattering and the energy spectrum of the X-rays. This model is widely used and well-established, see e.g. [\[97, 49, 69\]](#),

56, 37, 20, 67]. For a two-dimensional continuous function $f(\mathbf{x})$ that represents the attenuation coefficient at coordinate $\mathbf{x} = (x_1, x_2)$, Lambert-Beer's law states that the intensity attenuates exponentially as

$$I = I_0 e^{-\int_L f(\mathbf{x}) d\mathbf{x}}, \quad (2.1)$$

where I_0 denotes the X-ray intensity at the source, I denotes the intensity measured at the detector and L is the straight line from the source to one detector bin. The expression (2.1) can be rewritten to

$$\int_L f(\mathbf{x}) d\mathbf{x} = \log \left(\frac{I_0}{I} \right). \quad (2.2)$$

For one fixed angle the collection of all the integrals from the source to the detector bins is called the *projection* of the function. For each angle, every ray from source to detector bin is modeled as (2.2) and hence we have an integral equation, where we want to determine the integrand $f(\mathbf{x})$. If we model the right-hand side as a function, g , dependent on measurement angle and the detector position, we can define the so called continuous model as

$$\mathcal{A}(f) = g, \quad (2.3)$$

where \mathcal{A} is a functional that integrates a function as in (2.2) for each angle and detector position.

For measurement angle ϕ and detector bin position t the integral equation we need to solve corresponds to Radon transform, see [81], which can be written as

$$[\mathcal{R}_T f](\phi, t) = \int_{-\infty}^{\infty} f(t \cos \phi - \tau \sin \phi, t \sin \phi + \tau \cos \phi) d\tau. \quad (2.4)$$

The fact that the integral equation we want to solve is similar to a Radon transform is very fortunate since Radon already proposed a solution for such a problem 100 year ago (1917), see [81]. Unfortunately the exact solution can only be achieved if we know the Radon transform $\mathcal{R}_T f$ for continuous $\phi \in [0, \pi)$ and $t \in (-\infty, \infty)$ which is impossible to measure practically. For a $[0, 1] \times [0, 1]$ square 2D domain, where $f(\mathbf{x})$ has compact support in the inscribed circle, we "only" need to know the Radon transform for continuous $t \in [0, 1]$.

Determining $f(\mathbf{x})$ from the measured X-ray attenuation is often referred to as a *reconstruction* or a *tomographic reconstruction*. In practice measurements will be discrete and therefore a discrete model is a obvious necessity. We discretize the 2D domain into $M \times M$ pixels and model the X-ray source as a finite number of infinitely thin rays on a line. The measurements are naturally discretized by the finite number of detector bins N_t and the finite number of discrete measurement angles N_ϕ . Collecting

all the measurement data into a 2D array according to angle and detector position is usually called a *sinogram*. The discrete version of the function f is denoted by z and the discrete sinogram is denoted by b . The discrete CT-model used in this thesis is

$$\sum_h a_{n,h} z_h = b_n, \quad (2.5)$$

where $a_{n,h}$ describes the length of ray n through pixel h . By vectorizing z and b , to \mathbf{z} and \mathbf{b} , we can collect $a_{n,h}$ in the matrix A and we get the matrix-vector model

$$A\mathbf{z} = \mathbf{b}. \quad (2.6)$$

The continuous CT-model can be discretized in numerous ways, for more insight into the discretization of the CT-model see [20]. In general, the discrepancy between the discrete model, the continuous model, and the actual physical process of X-ray transmission is a very interesting topic which is outside the scope of this thesis, but more information can be found in e.g. [69, 56, 50, 67].

In this thesis all of the topics will be highly related to the reconstruction problem, either in the continuous (2.3) form or in the discrete (2.6) form. Before diving into some reconstruction methods I will present another tomographic technique, that paper A is concerned with, which is very similar to standard computed tomography.

2.2 Phase contrast tomography

There are many deviations between the classical CT-model presented in the previous section and actual physical process of X-ray transmission. Among other things the X-ray energy spectrum and the scattering effects can cause problems when solving the reconstruction problem. Phase contrast tomography (PCT) aims to account for some of the scattering effects that happens when X-rays interact with matter, and in fact utilize this behavior to gain more knowledge about an object.

Phase contrast imaging with X-rays covers a wide variety of measurement techniques developed by experimental physicists over the last ~ 50 years. A few of the more popular methods are: crystal interferometry, see [13], diffraction enhanced imaging, see [30], grating based methods, see [31, 75] or propagation based methods, see [2, 61]. For a more thorough introduction to phase contrast imaging and the different techniques see [61]. Common for all of these techniques is that they utilize the fact that electromagnetic waves are not only attenuated when they interact with matter, but the wave-phase is also altered.

All materials have a complex refractive index n_i which can be described by the refractive index decrement, δ , and the absorption index, β , as

$$n_i = 1 - \delta + i\beta, \quad (2.7)$$

for complex unit ι . Here β should not be confused with the absorption/attenuation coefficient from Lambert-Beers law which is proportional to the index through $z = \frac{4\pi}{\nu}\beta$, for X-ray wavelength ν , see [62]. For some objects the refraction contrast can be much larger than the absorption contrast, dependent on material type and X-ray energy. The higher contrast can be crucial when we want to distinguish between different materials, which is the main reason for trying to reconstruct both the absorption and the refraction for an object. The phase contrast method that we chose to focus on is the so called propagation method or *free-space* propagation method. For this technique the setup is very similar to CT, no further equipment is needed, the detector is simply just placed further away from the object than for classical CT. The increased distance ensures a propagation of the phase shift that makes it detectable. This propagation is illustrated in Figure 2.2 where the measured signal at a 2D detector is simulated. The simulated object consist of some purely absorbing cylinders and some purely refractive cylinders. As seen the refractive objects become visible at when the detector-distance is increased, which is the principle utilized in the free-space propagation method.

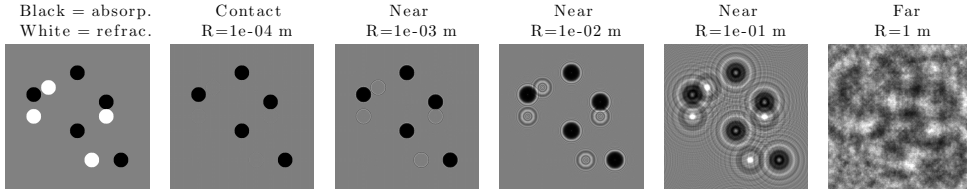


Figure 2.2: Simulated projections of cylinders measured at a detector for varying object-to-detector distance R .

Using the complex refractive index, the model from source to detector goes as follows: first the spatially dependent absorption index and refractive index decrement are projected

$$B(\phi, t) = \frac{2\pi}{\nu} \int_L \beta(\mathbf{x}) d\mathbf{x} \quad (2.8)$$

$$\psi(\phi, t) = -\frac{2\pi}{\nu} \int_L \delta(\mathbf{x}) d\mathbf{x}. \quad (2.9)$$

These projections can be considered as Radon transforms of the refractive and absorption indexes, scaled by a factor. We call the collection of all the projections the absorption B and the phase shift ψ . These two signals are not separated inside the object, and the mixture of the two signals is modelled by transmission

$$T(\phi, t) = e^{-B(\phi, t)} e^{\iota \psi(\phi, t)}. \quad (2.10)$$

In the Fresnel region, see [2, 62], the Fresnel propagator describes the final propagation

from the object to the detector

$$I^R(\phi, t) = |T(\phi, t) \star P(t)|^2, \quad P(t) = -\frac{t}{\nu R} e^{\frac{i\pi}{\nu R} |t|^2}, \quad (2.11)$$

where I^R is the intensity measured at the detector with distance R to the object, \star is a convolution operator and $|\cdot|$ is the Euclidean norm in 2D.

Taking angular projections, exactly as for parallel beam CT will give sinogram data that is the same as for standard CT if the object-to-detector distance is small, otherwise, the problem that we have to solve is a phase constant tomographic (PCT) problem. Classical reconstruction methods for PCT consist of two stages: A phase retrieval stage where the absorption β and phase shift ψ are retrieved from the intensity measurements followed by a reconstruction stage, where the absorption and refractive indexes are reconstructed. The reconstruction stage is exactly the same as for the CT problem and hence similar reconstruction methods can be used. The next section presents a series of standard reconstruction methods.

2.3 Tomographic reconstruction

In this section I will briefly present some of the most established and widely used image reconstruction techniques for computed tomography. Common problems that influences the reconstruction results, such as artifacts and noise, is also presented. Finally I will discuss advantages and disadvantages of the different reconstruction methods.

2.3.1 Filtered back-projection

The reconstruction method that is most widely used for solving the CT-reconstruction problem is also the oldest method. The method was introduced by Johan Radon 100 years ago, see [81], before any tomography techniques were even developed. The method is most commonly referred to as Filtered Back-Projection (FBP) and consist of two simple steps: a filtering of the measured signal, in the Fourier domain, and a back-projection from the sinogram-domain to the object-domain.

The method guaranties an exact reconstruction of the function assuming that we have continuous projection, $t \in [0, 1]$, for every angle in the continuous angle interval $\phi \in [0, \pi)$. Given a sinogram function $g(\phi, t)$ that fulfill the above requirements, the function is first filtered with a ramp filter

$$\begin{aligned} \widehat{g}(\phi, \omega) &= \int_0^1 g(\phi, t) e^{-2\pi i \omega t} dt, \\ \widetilde{g}(\phi, t) &= \int_{-\infty}^{\infty} \widehat{g}(\phi, \omega) |\omega| e^{2\pi i \omega t} d\omega, \end{aligned}$$

and then back-projected

$$f(x_1, x_2) = \int_0^\pi \tilde{g}(\phi, x_1 \cos \phi + x_2 \sin \phi) d\phi.$$

As mentioned previously the actual measured sinogram data will be discrete. With finely sampled projection data distributed all over the 180° the FBP method can still give very good reconstructions, even though the continuity requirements are not fulfilled. For the discrete case the filtering can be carried out by use of discrete Fourier transform and the back-projection by use of numerical integration.

2.3.2 Algebraic methods

The algebraic reconstruction methods essentially aim at solving the discrete linear problem (2.6). The most popular types of methods are the sequential methods, for instance the Algebraic Reconstruction Technique (ART), and the simultaneous methods, for instance the Simultaneous Iterative Reconstruction Technique (SIRT). Common for these methods is that they are iterative, i.e. we do not get the solution by a single back-projection, but the solution is sequentially altered until we stop the algorithm. Some kind of stopping criterion must therefore be chosen for these methods. In the literature there are many ways of choosing such criteria, see e.g. in [50].

ART, also called Kaczmarz method, is a row-action method, i.e. the algorithm sweeps over one row of the matrix A at a time as an inner loop of the algorithm. For an algorithm initialization \mathbf{z}^0 , e.g. a zero-vector, the algorithm simply consist of the following the solution update

$$\mathbf{z}^{k+1} = \mathbf{z}^k + \frac{\mathbf{b}_r - \mathbf{a}_r \cdot \mathbf{z}^k}{\|\mathbf{a}_r\|_2^2} \mathbf{a}_r, \quad (2.12)$$

where \mathbf{a}_r is the r 'th row of A .

The simultaneous reconstruction techniques does not include the inner loop that sweeps through the rows of A one at a time, but uses the entire matrix A and its transpose. One of the most widely used simultaneous methods is the SIRT method, see for instance in [52]. The simultaneous methods are known to converge slower than the sequential methods.

Simple constraints can easily be build into the iterative loop in the algebraic reconstruction methods, which makes them more flexible than FBP. In [52] one can get a more detailed introduction to the algebraic reconstruction methods.

2.3.3 Variational methods

Variational methods are widely used for inverse problems and imaging problems in particular. For an inverse problem, a variational method could be seen as a energy minimization method that tries to solve $\mathcal{A}(f) = g$ for some linear or non-linear operator \mathcal{A} , while incorporating a prior that describes what we expect or desire of f . This

is most often carried out by use of regularization which will be presented in greater depth in [Chapter 3](#). A very nice book on variational methods for imaging problems is [\[89\]](#) where the topic is elaborated upon with many details.

Using a variational method, with some regularizer \mathcal{R} , to solve the continuous CT reconstruction problem in [\(2.3\)](#) we end up with the following minimization problem

$$\text{minimize}_f \mathcal{G}(\mathcal{A}(f), g) + \lambda \mathcal{R}(f), \quad (2.13)$$

where \mathcal{G} is a so called data-fidelity term and $\lambda \in \mathbb{R}_{\geq 0}$ is the regularization parameter that balances the two terms. The data fidelity term is typically chosen based on the expected noise model. For white Gaussian noise the suited data fidelity term would just be the L^2 -norm, so

$$\mathcal{G}(\mathcal{A}(f), g) = \frac{1}{2} \|\mathcal{A}(f) - g\|_{L^2}^2, \quad (2.14)$$

in this case. The regularization term should be chosen based on expectations for f . Some regularization methods that has been used for the CT reconstruction problem are Tikhonov regularization, see [\[69\]](#), Total Variation (TV), see e.g. [\[94, 98, 93\]](#), Mumford-Shah, see [\[60\]](#), sparsity regularization, see e.g. [\[40, 55\]](#).

The advantages of using variational methods for solving the CT reconstruction problem is the possibility of choosing suitable noise-model while additionally including priors that can help to diminish undesired e.g. artifacts.

2.3.4 Artifacts and noise

When solving the CT reconstruction problem, one is likely to encounter undesired artifacts, unless much care is taken. Artifacts are structured elements in the reconstruction that are unrealistic, based on what we expect to see in an object. The artifacts mainly comes from the mismatch between the real physical phenomenons and the mathematical model, or from the reconstruction methods themselves.

Some typical artifacts in CT are ring- and motion-artifacts. Ring-artifacts are typically caused by mechanical problems such as malfunctioning detector bins or a miscalibration. Motion artifacts comes from motion of the object, which is a typical problem for medical imaging. The mathematical model assumes perfectly calibrated detector bins and a completely steady object which is why there is a mismatch.

Beam hardening, scatter and metal artifacts are all caused by the fact that an X-ray source is never completely monochromatic, but to some extend polychromatic. At synchrotrons it is possible to produce beams which are much more monochromatic than on laboratory and hospital equipment. Since the attenuation coefficients of different materials are not constant for different X-ray energy, a polychromatic source

can cause streak artifacts and intensity scaling. Streak artifacts can also be caused by materials that are so dense that the X-rays can not penetrate them.

Limited data artifacts comes from measurement set-ups where either an insufficient number of angular projections are taken or where the span of projection angles is less than 180° , or both. These artifacts are typically seen as streaks, intensity smearing and missing edges. Such effects are typically seen in FBP reconstructions, where it is hard to deal with them, other handling them in post-processing. Limited data artifacts can also occur for the algebraic and variational methods since a limited data a measurement set-up will give a non-trivial null-space of the forward operator.

Measurement noise is present within all imaging technologies. For CT problems the measurements are photon counts for each detector bin, and this process follows a Poisson distribution. For large photon count in the detector bins the process can be regarded as following a Gaussian distributions see [39, 53, 64]. Longer exposure-time will in practice increase the signal-to-noise ratio, but naturally also increase the X-ray dose and be more time consuming. Small noise perturbations can cause large variations in the reconstruction due to the CT problem being *ill-posed*, more on this in [Chapter 3](#). The FBP method is especially bad at handling this, since high-frequency signals, such as noise, are amplified. The algebraic methods does not amplify the noise, but still suffers from the fact that the reconstruction problem is ill-posed.

These are some of the most typical artifacts within CT and there are numerous ways to handle them suggested in the literature. For a more detailed overview of CT-artifacts and some ways handling them see e.g. [12, 41].

2.3.5 Picking a reconstruction method

No CT reconstruction method is completely superior to the others and here I briefly try to outline advantages and disadvantages for the different methods.

The FBP method is very easy to implement and computationally highly efficient since it is not iterative, and since Fast Fourier Transform (FFT) can be utilized. On the downside FBP has a hard time handling limited and corrupted data. The method requires a lot of projection data with low noise, which means increased measurement time and higher dose exposure. Furthermore it is difficult to include constraints or any other types of prior information when FBP is used.

The algebraic methods can handle limited data problems and it is possible to include some simple constraints for these methods. Some of the methods has a fast initial convergence which makes them very useful for getting a fast, but coarse reconstruction. Some disadvantages are: The risk of null-space artifacts, limited possibility of incorporation of more complicated prior information, their ability to handle and

diminish noise and the computational cost which is significantly higher than FBP if we want to achieve high resolution reconstructions.

The variational methods can handle both limited and noise-corrupted data, while also incorporating constraints and priors. But in order to solve the minimization problem, optimization methods that are much more complicated than FBP and the algebraic methods, are needed. There is a large risk of slow converge for these methods, and hence the computational demand is typically higher than for the algebraic methods. Furthermore the incorporation of prior information through regularization is often limited by the fact that we desire a convex model.

In order to make a small demonstration of some of the different reconstruction methods and their performance I show three different simulated sinogram measurements in [Figure 2.3](#) together with the original object. In [Figure 2.4](#) I then show reconstructions from these three sinograms using the methods: FBP, SIRT and a discrete version of L^2 -TV. The methods are all tuned to perform optimally for this sample. The methods have been timed for 100 random noise realizations, the FBP reconstructions took in range of 0.05-0.3 sec, the SIRT reconstructions took 50-120 sec, and the L^2 -TV reconstructions took 80-1000 sec. This test does in no way cover the entire complexity of reconstruction methods for CT, but merely serves as a demonstration of some of the methods reviewed in this section.

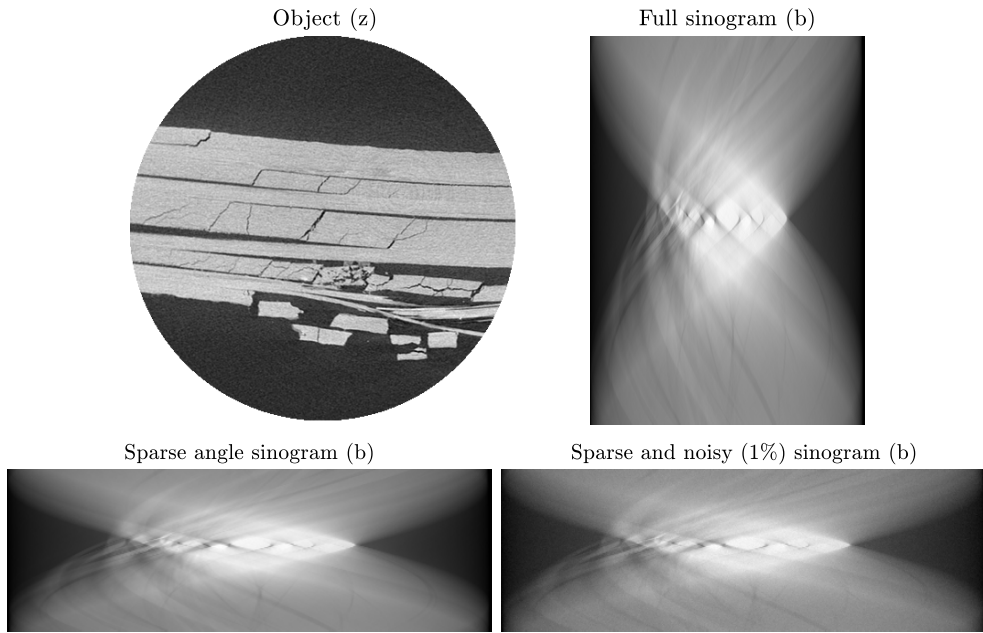


Figure 2.3: Carbon fibre object borrowed from [85] (top left). Sinogram data from 600 uniformly distributed projections angles (top right). Sparsely sampled sinograms from 142 uniformly distributed projection angles, with and without noise (bottom).

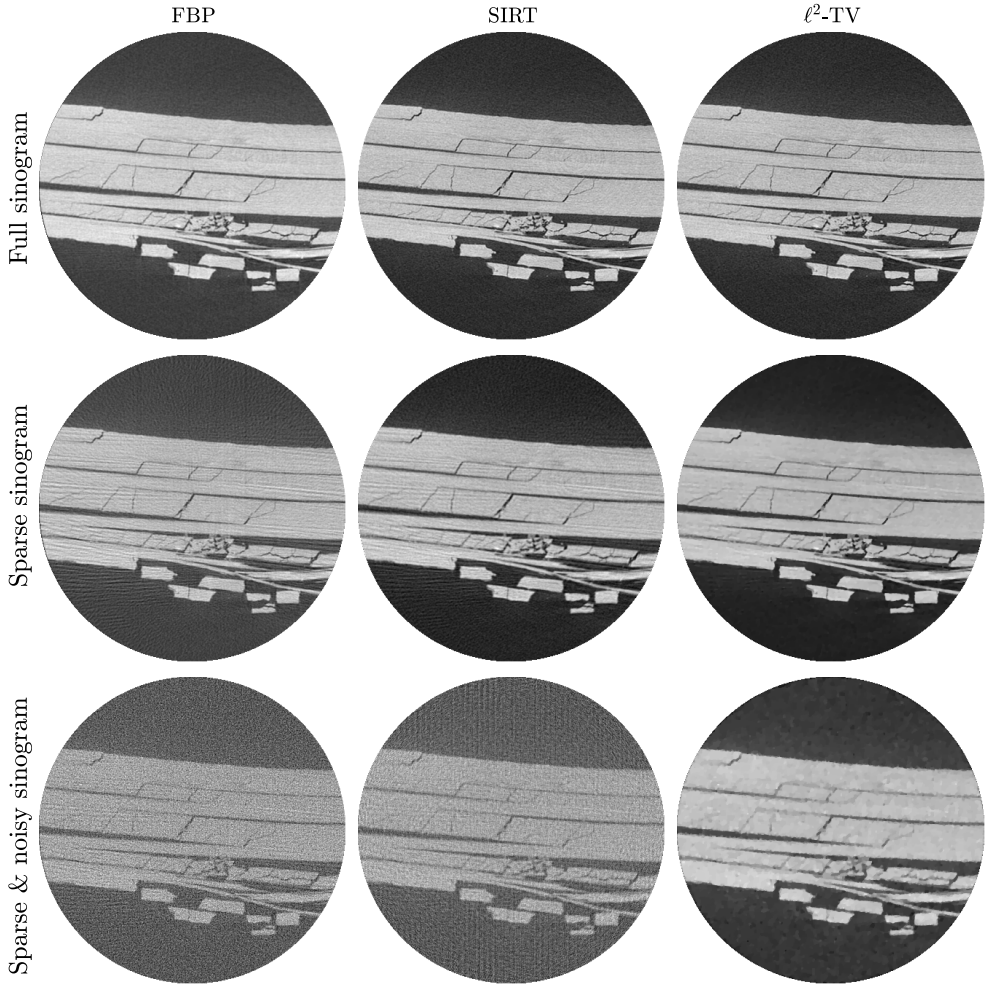


Figure 2.4: Reconstructions of the object in [Figure 2.3](#). Horizontal direction: Different reconstruction methods. Vertical direction: Different sinogram data-sets, see [Figure 2.3](#).

CHAPTER 3

Regularizing Inverse Problems

Inverse problems is a broad mathematical topic that, among other things, covers imaging methods. In this chapter I present and discuss the topic in general terms. Inverse problems are problems where we can only observe the object we want to analyze indirectly. Inverse problems include problems within medical imaging, see e.g. [66, 87, 14], geophysics, see e.g. [78], radar and astronomy, see e.g. [6], computer vision and machine learning, just to mention a few. Detailed mathematical theory about inverse problems can be found in [59].

A common obstacle for solving inverse problems is *ill-posedness*. I will elaborate a bit on this in order to highlight the problem, and to explain why we need a way to handle it. A common strategy for overcoming ill-posedness is by use of regularization. I review this strategy in more details together with some of the currently most used regularization techniques within imaging.

3.1 Inverse problems

Knowing a structural parameter for an entire object and a model, in form of some operator, the *forward problem* is going from the structural parameter to some observations through the model. The *inverse problem* is the opposite; determining some structural parameter based on a number of observations and some or all knowledge about the model. An example is the CT problem presented in the previous chapter. For this problem we go from the sinogram data, see Figure 2.3, to the reconstruction,

see Figure 2.4. For many inverse problems the forward model is assumed to be known and it is also assumed to be the case in this thesis. Whether or not this model is accurate for underlying the physical problem is an entirely different question which lies beyond the scope of this thesis.

A general inverse problem can be stated as follows: Determine function f , that describes some structural property of an object, based on

$$\mathcal{A}(f) = g, \quad (3.1)$$

where the forward model \mathcal{A} and the observed function g are known. Here g is often corrupted by some sort of noise.

Hadamard introduced the definition of a *well-posed* problem in 1923 in [48]. It is stated that a well-posed problem should fulfill three criteria:

- the problem should have a solution,
- the solution should be unique,
- and the solution should depend continuously on the data.

Related to these criteria are the well-known mathematical concepts of *existence*, *uniqueness* and *stability*. The opposite of a well-posed problem is indeed called an *ill-posed problem*. In the field of inverse problems ill-posedness is very common. Different magnitudes of ill-posedness exist and these are some times referred to as *slightly* ill-posed opposed to *strongly* ill-posed. The CT reconstruction problem is for example slightly ill-posed, see for instance [70].

These concepts are related to classical linear algebra matrix properties. For a linear discrete inverse problem on the form

$$Az = \mathbf{b}, \quad (3.2)$$

where A is the matrix representation of the forward operator, \mathbf{z} is the unknown object and \mathbf{b} is a noisy measured signal, no solution would exist if A has full rank while being overdetermined. If A is underdetermined then the null-space will be non-trivial and infinitely many solutions will exist. Finally if A has a large condition number, the system is ill-conditioned, and a relatively small amount of noise in the measured signal can therefore lead to large changes in the solution, hence it is unstable.

3.2 Variational formulation with regularization

Overcoming ill-posedness by regularization is elaborated upon in great details in e.g. [100, 35, 89, 50]. Some of the most widely used regularization techniques within

imaging are presented here together with their respective priors. Iterative methods, as the algebraic methods presented in [Section 2.3.2](#), or the Krylov subspace methods, are also considered to be regularization techniques, see [\[35, 50\]](#), but in this thesis I introduce regularization through a variational formulation. It is difficult to discuss regularization through variations method without mentioning the data fidelity term. I will therefore also touch upon the choice of data-fidelity term, which can be as important as the choice of the regularizer.

Variational methods were previously reviewed for solving the CT reconstruction problem in [2.3.3](#). Here I elaborate a bit more on these methods for inverse problems in general. A variational formulation for solving an inverse problem on the form [\(3.1\)](#) can be posed as the following minimization problem

$$\underset{f}{\text{minimize}} \mathcal{G}(\mathcal{A}(f), g) + \lambda \mathcal{R}(f) \quad (3.3)$$

The first term is the data fidelity term, the second term is the regularization term and λ is the regularization parameter balancing the influence of two terms. Here \mathcal{G} , typically a norm, measures the difference between $\mathcal{A}(f)$ and g . The data fidelity term is typically designed to fit the expected forward model. Since noise is inevitable in real life measurements, \mathcal{G} should be designed to accommodate the type of noise likely to be present in the measurements.

For expected additive Gaussian noise the squared L^2 -norm fits the distribution, so for such a case we should choose

$$\mathcal{G}(\mathcal{A}(f), g) = \|\mathcal{A}(f) - g\|_{L^2}^2.$$

The squared L^2 -norm is the most widely used data-fidelity term choice, especially if the noise-model is unknown. We use this data-fidelity term in the papers [A](#), [B](#) and [D](#).

For *impulse* noise the L^1 -norm should be chosen:

$$\mathcal{G}(\mathcal{A}(f), g) = \|\mathcal{A}(f) - g\|_{L^1}.$$

We use this norm in paper [C](#). Minimizing the L^1 -norm is usually also used to remove outliers from signal measurements, see [\[17\]](#). More on the L^1 -norm data-fidelity term for removing impulse noise can be found in [\[72\]](#).

If the noise is expected to follow a Poisson distribution, the data-fidelity term should be a generalized *Kullback-Liebler divergence* measure

$$\mathcal{G}(\mathcal{A}(f), g) = \int_{\Omega} \mathcal{A}(f) - g \log(\mathcal{A}(f)) \, dx \quad \text{where} \quad \mathcal{A}(f) \geq 0.$$

Where $\Omega \subset \mathbb{R}^N$. Further detail about Poisson noise and the data-fidelity term above can be found in [\[8, 38, 91, 103\]](#).

For more details and methods for handling other non-Gaussian noise models, such as Rician noise, multiplicative noise and Cauchy noise, see [90].

The main goal for using regularization in a variational formulation is to handle and reduce the undesired ill-posedness effects. These effects could for example be introduction of artifacts or magnification of measurement noise. As indicated in (3.3) regularization methods often targets the unknown function f , or some order derivative of f , but regularization methods that targets for example $\mathcal{A}(f)$ also exist. In this brief introduction to regularization I stick to regularization methods on the form $\mathcal{R}(f)$.

The choice of regularization method should, from a Bayesian point of view, be motivated by the features that we expect our unknown object to express. We usually say that the choice of regularization method should fit our prior for the unknown function.

The most widely used regularization method is also one of the first to be introduced. Like the most widely used data fidelity term, this regularization method is also based on the L^2 -norm. The L^2 -regularization method is typically referred to as *Tikhonov regularization*, see [79, 99] for the original works on this regularizer. Tikhonov regularization usually refers to a squared and weighted L^2 -norm

$$\mathcal{R}(f) = \int_{\Omega} |w(x)f(x)|^2 dx, \quad (3.4)$$

where $w(x)$ is a weight function, often just chosen to be $w(x) = 1$. Tikhonov regularization also refers to the squared L^2 -norm on the gradient of f :

$$\mathcal{R}(f) = \int_{\Omega} |\nabla f(x)|^2 dx. \quad (3.5)$$

It is very advantageous to use Tikhonov regularization together with the L^2 data fidelity term, since for this combination the variational problems has a closed form solution that can be determined using very efficient algorithms, see [51]. Tikhonov regularization is related to a prior that f or ∇f is smooth. The smoothing effect of Tikhonov regularization helps to suppress artifacts and noise, but for this prior is rarely satisfied by the objects we want to examine using imaging techniques.

Within imaging science and image processing a specific regularization method has gotten a lot of attention over the last two decades. That is the *Total Variation* (TV) regularization method introduced in [86]. The reason that this regularization method is so popular within imaging and image processing, is that it preserves edges and at the same time suppresses noise and artifacts. The prior for this regularization method is that f is piecewise constant. This prior fits to a much larger range of problems within imaging and within inverse problems in general. See [101, 32, 28, 33, 54, 84] for some applications of TV regularization for denoising, deconvolution, and tomographic

reconstruction problems. The dual formulation of TV is given as

$$\mathcal{R}(f) = \text{TV}(f) = \sup \left\{ \int_{\Omega} f \operatorname{div} \mathbf{v} \, dx \mid \mathbf{v} \in C_c^1(\Omega, \mathbb{R}^2), \mathbf{v}(x) \in B_2(0) \, \forall x \in \Omega \right\}, \quad (3.6)$$

where \mathbf{v} is the dual variable and $B_2(0)$ is the closed Euclidean unit ball centered at the origin. Another very typical way of introducing TV is by its primal formulation, though this requires $f \in C^1(\Omega)$. If that requirement is satisfied the regularizer can be written as

$$\mathcal{R}(f) = \int_{\Omega} |\nabla f(x)|_2 \, dx,$$

where $|\cdot|_2$ is the Euclidean norm.

Several modifications of TV has been proposed for various applications, I will mention a few of them here. A common drawback of TV is the so called stair-caising effect that occurs when regularizing with TV, while f is not piecewise constant, but piecewise affine or piecewise smooth. Higher order methods have been suggested to overcome this, see [88, 29, 92, 19]. Here most notably Total Generalized Variation (TGV), see [19], which has been the basis for regularization method that we have proposed and analyzed in paper B. Other examples of TV modifications are anisotropic TV [46], nonlocal TV [44], spectral TV [43], and structure tensor TV [63].

Another regularization method that is very popular within signal processing in general, is *sparsity* regularization. The great interest is related to the *compressed sensing* results that states that a signal can be recovered with less sampling than usually required, given knowledge about the sparsity of the signal, see more about this in [34, 22, 23]. Sparsity of a signal refers to the signal having few non-zero coefficients or being sparse through some transformation, e.g. in another basis or by a dictionary representation. In terms of regularization method, this method is mainly related to discrete problems, so I refer to the discrete inverse problem (3.2) when presenting this regularization method. The simplest sparsity regularizer is the so called 0-norm. For discrete signal \mathbf{z} the 0-norm is usually denoted $\|\mathbf{z}\|_0$ although it is not a norm. $\|\mathbf{z}\|_0$ counts the number of non-zero elements in \mathbf{z} . Solving the problem

$$\|\mathbf{z}\|_0 \quad \text{s.t.} \quad A\mathbf{z} = \mathbf{b} \quad (3.7)$$

is unfortunately not so easy, it is in fact NP-hard, see e.g. [18]. Therefore the 0-norm is usually relaxed to a 1-norm to achieve a solvable problem. A typically considered sparsity regularizer is therefore

$$\mathcal{R}(f) = \int_{\Omega} |f| \, dx \quad (3.8)$$

Within image processing sparsity regularization on a transformed version of f is also very typical, it could for example be a sparsity of f represented in a frame-basis such

as wavelets, see e.g. [47]. Other sparse regularization methods seek to find a sparse solution in a dictionary representation, which could be learned from expected object samples, see e.g. [95]. Total variation can also be seen as a regularization method that enforces sparsity of the gradient. In [55] sparsity regularization in general, and specifically for the CT reconstruction problem, is reviewed with a lot of analysis of sampling and recoverability guaranties.

Some of the regularization methods mentioned in this chapter are demonstrated for two simple denoising problems. The two phantoms, with and without noise, can be seen in Figure 3.1. The regularization methods are tuned to perform the best, according to the peak-signal-to-noise ratio, for the individual problems. The noise, in both cases, is simulated additive Gaussian noise, 10%, hence a L^2 data-fidelity term is used. In Figure 3.2 results of using different regularizers can be seen. The Tikhonov method is seen to be inferior to the other two methods for the grain phantom, whereas both Tikhonov and TV are inferior to TGV for the blob-phantom.

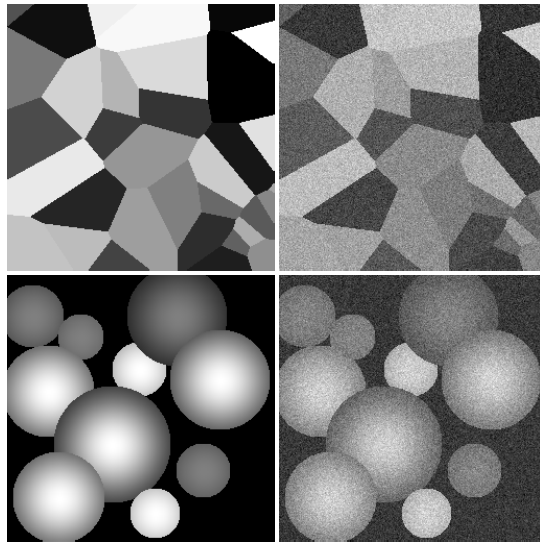


Figure 3.1: On top: Grain phantom from Airtools [52]. Bottom: Blob-phantom. Phantoms without noise to the left and phantoms with 10% additive Gaussian noise to the right.

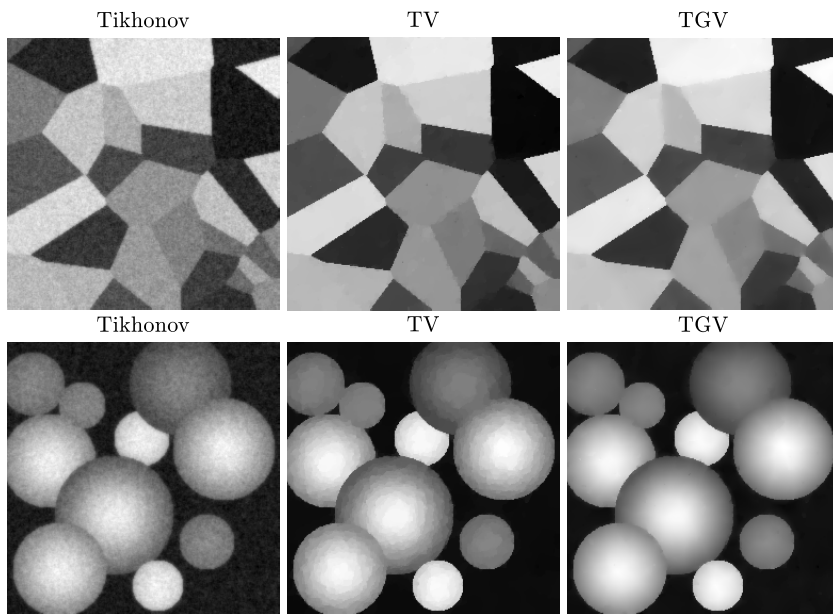


Figure 3.2: Denoising results of the two noisy images seen in [Figure 3.1](#), using different regularization methods.

CHAPTER 4

Numerical Aspects

All of the enclosed papers of this thesis makes use of variational methods and regularization. Using these methods requires solving an optimization problem. In this chapter I will discuss the requirements and choices of optimization methods that are necessary to consider when using variational methods for solving inverse problems. A recent and very thorough overview of optimization method for imaging problems is given in [27], which I will recommend for an in-depth introduction and discussion of important and recent work within this field. The optimization methods discussed in this chapter are based on solving discrete inverse problems on the form (3.2). For such a problem the corresponding discrete variational formulation is denoted as

$$\operatorname{argmin}_{\mathbf{z}} \mathcal{J}(\mathbf{z}) \tag{4.1}$$

$$\text{for } \mathcal{J}(\mathbf{z}) = G(A\mathbf{z}, b) + \lambda R(\mathbf{z}), \tag{4.2}$$

where G measures the difference between $A\mathbf{z}$ and \mathbf{b} , and R represents the choice of regularization method. In the enclosed papers the practical problems we solve are denoising, deblurring and CT reconstruction, I will in general refer to all of these problems as reconstruction problems.

Choosing the optimal value of the regularization parameter is an essential ingredient of variational methods. I will briefly review issues and methods related to the regularization parameter choice.

When comparing reconstruction methods it is highly useful to have a reference reconstruction that can be used for benchmarking. One way to achieve this is to simulate the measured data and the noise. In this thesis PCT/CT reconstruction, denoising, and deblurring are the inverse problems handled in the contributing papers. I briefly

discuss how the measurement data is simulated for these problems.

Having a ground truth, the next question that arise is how to quantify which reconstruction is "closest" to the ground truth. I present a few methods which are often used for measuring the similarity between two images.

4.1 Optimization

Optimization algorithms for solving variational problems comes in many forms, dependent on the properties of the specific minimization problem. Some important things to consider are: The size of the problem, i.e. the size of the matrix A . Whether or not the problem is convex and whether or not it is smooth. And the convergence rate of the algorithm is also significant for several applications.

For smooth problems, i.e. continuously differentiable, some classical and popular optimization methods are: Gradient descent, trust-region, conjugate-gradient, interior-point, etc. These methods has applicability for a large range of problem. More on these methods can for instance be found in [17, 73].

For non-smooth problems I will highlight the Primal-Dual method, see [3, 25, 71] and the Alternating Direction Method of Multipliers (ADMM) method, see [16]. Some popular fast methods for large systems are limited memory BFGS, see [21], the Fast Iterative Shrinkage-Thresholding Algorithm (FISTA), see [10], and the Primal-Dual-Hybrid-Gradient (PDHG) method, see [36, 26]. FISTA, ADMM and PDHG have gotten a lot of attention in the inverse problems community, and they are often used since they are adaptable, relatively fast, and relatively easy to implement.

All of the previously mentioned methods are aimed at convex problems. For non-convex problems the internal proximal algorithm (iPiano), see [74], and ADMM are often used.

4.1.1 Requirements and choice of optimization method

Here I list some considerations and requirements for optimization method choice in relation to variational methods.

One major reason for using variational methods is that they can be used to overcome the undesired effects of ill-posedness and noise. Minimizing a data-fitting term, instead of trying to find the exact solution to (3.2), is a way ensuring that the problem we are trying to solve has at least one solution. Choosing convex data-fitting and regularization terms are useful since uniqueness of the solution is desirable. Introduction of a regularization term can also fix instability issues and reduce the noise, though

some popular regularization terms are not smooth, e.g. total variation. Optimization methods that can handle non-smooth objective functions can therefore be desirable. Incorporation of constraints is also a valuable feature for an optimization algorithm, since additional constraints often occur when solving inverse problems. Finally a practical, but also very important, requirement is efficiency, related to both convergence within a desired time and reasonable memory allocation.

In all of the contributing papers of this thesis one specific algorithm has been used, and that is the PDHG algorithm from [26], sometimes called the *Chambolle-Pock* algorithm. The choice of this method is based on several considerations. First of all CT-reconstruction problems are in practice very large scale problems, for example for a 2D CT-reconstruction problem with a 256×256 reconstruction domain, 256 detector bins and 256 projections, the matrix A has more than $4 \cdot 10^9$ elements, and that is actually a relatively small 2D problem. This fact made us avoid second-order methods and also approximate second-order methods. Moreover, in the enclosed papers of this thesis we have proposed or used convex data-fitting and regularization terms to ensure necessary conditions for getting a unique solution. Several of the regularization terms we work with are non-smooth and hence we needed a method that could handle this. Another typical way to handle this is to smooth the functional, but this typically introduces another parameter, which we decided to avoid. For the FISTA method, incorporation of constraints are not that easy, and we therefore ruled out this method, which led to the choice of the PDHG method. The PDHG method is also easy to implement and to adapt to different types of variational formulations. The convergence rate for the PDHG method is reasonably good, but ADMM could seem to be faster for some types of problems according to [27].

4.1.2 Regularization parameter and stopping criteria

The regularization parameter plays a very important role for the solution of a variational problem. There is a certain point, a certain value of λ , that gives the 'optimal' solution. Of course that point depends on what 'optimal' means, and this is the first reason that picking the optimal λ is not a simple task. Regularizing an inverse problem too little, i.e. choosing a too small λ , can result in a solution corrupted by noise and artifacts. Regularizing a problem too much and the solution can lose features that are otherwise important for the further analysis.

Picking the exactly right regularization parameter will correspond to picking the parameter that gives exactly the solution we seek, the 'ground truth', which we obviously do not know in practice. Most of the strategies for picking the optimal λ are based on solving the problem (3.2) for a range of λ -values, and from these different solutions picking one that is most optimal based on some criteria. Methods that state how to define such criteria are for example the L-curve method and generalized cross validation. If we have some knowledge about the noise-level it can be utilized to de-

termine the optimal λ using Morozov’s discrepancy principle. In general, no method is superior to all others for arbitrary problem types. It is not the focus of the work in this thesis to test and compare different methods for picking the regularization parameter. In all of the contributing papers the regularization parameter has been chosen by comparing the results with the ground truth or by choosing visually preferable solutions. More on picking the optimal regularization parameter can be found in [50].

Another parameter to consider is the *tolerance* related to the stopping criterion. Iterative optimization method has be stopped at some point when a reasonable solution is reached. If we just stop after a fixed number of iterations, we have no guarantee that the solution has converged. Typical stopping criteria are based on the objective function that we are minimizing \mathcal{J} . In the simplest case it could be to stop the algorithm when the objective goes below some tolerance. Otherwise when the relative change of \mathcal{J} or the gradient of \mathcal{J} in some norm goes below a tolerance. The stopping criterion could be based to the first order optimality conditions or, due to simplicity, based on the relative change of the actual solution \mathbf{z} . For the PDHG methods the primal-dual gap can be calculated, see [17], and therefore this is often used to stop this algorithm.

4.1.3 Implementation

When implementing a chosen optimization algorithm there is also some choices to consider.

First of all, discretization of domains, functions and operators, such as the gradient and the divergence operators, can influence the final result. Since the papers of this thesis are related to denoising, deblurring and tomography problems the object domain is discretized into equidistant square pixels. In all of the enclosed papers the gradient and divergence operators are discretized using first order finite differences with symmetric boundary conditions.

Memory issues are still important, even though hardware improvement in computers has been increasing massively the last decades. As mentioned previously the matrix A can be enormous for tomography problems, and hence we do not want to store this on the hardware in its entirety. Fortunately this matrix is sparse and this can help for some types of problems, although some problem are so large that this is still a problem. Another solution to this problem, is to use a so called *matrix-free* implementation where the application of A on \mathbf{z} is calculated when it is needed in the algorithm. We used a matrix-free implementation of the CT forward operator in paper A and D. See more about the ASTRA toolbox that we used for this in [1].

Efficiency of the implementation is very important, especially for real practical prob-

lems. There are many ways of increasing the efficiency of an implementation. The ASTRA toolbox provides increased speed by use of GPU's when calculating projections, and this we have utilized. Parallelization will in many cases increase the speed of an algorithm. Other ways to achieve increased speed of an optimization algorithm is to use *preconditioning*, a qualified *initialization* or a so-called *warm start*.

In the contributing papers of this thesis, efficiency of the implementations has only been an aspect to the extent that it was possible to conduct experiments within reasonable time. For the large scale problems that would be solving one minimization problem in a matter of minutes.

4.2 Simulated experiments and quantification

In the papers of this thesis two aspects has been very important for the numerical experiments conducted: First and foremost, we strive to demonstrate new methods in best-case experiments with respect to simulation and parameter choices. We do this in order to avoid any bias of the results caused by the parameter choices, the noise simulations, etc. In order to make a fair comparison with respect to other reconstruction methods we did the same for these methods. Second, we always strive to demonstrate how failed assumptions and disadvantages of a method can influence a solution.

Simulating the reconstruction problems and the noise ourselves, gives us the advantage that we have a ground truth that we can compare our results to. Since we use variational methods, simulated experiments can also ensure that we choose the data-fidelity terms optimally, such that when we are testing the influence of a regularization method, the tests are not biased by the choice of the data-fidelity term.

Judging the quality of a reconstruction can be done by visual inspection or by quantitative measures. Given a ground truth \mathbf{z}^* and reconstruction \mathbf{z} a typical quantitative measure could be the relative 2-norm error, i.e

$$\frac{\|\mathbf{z}^* - \mathbf{z}\|_2}{\|\mathbf{z}^*\|_2}. \quad (4.3)$$

Another typically used error-measure, is the root means square error (rmse)

$$\text{rmse}(\mathbf{z}^*, \mathbf{z}) = \frac{1}{\sqrt{M}} \|\mathbf{z}^* - \mathbf{z}\|_2, \quad (4.4)$$

where M is the number of elements in \mathbf{z} .

Within the image processing community two error-measures are very often used, the peak-signal-to-noise (psnr) ratio and the structure similarity index (SSIM). The psnr

measure is a scaling of the rmse measure depending on the dynamic range of the pixels in \mathbf{z}^* . For maximum possible pixel intensity H the psnr measure is

$$\text{psnr}(\mathbf{z}^*, \mathbf{z}) = 20 \log_{10} \left(\frac{H}{\text{rmse}(\mathbf{z}^*, \mathbf{z})} \right)$$

The SSIM measure is an attempt to make an image quality measure that better describes what we as observers visually favor, opposed to e.g. psnr. This method depends on several tunable parameters, see more in [102].

A problem with these quantitative error-measures is that they are not really comparable across different images, but using them to compare different methods for a single image is still a relevant tool. We have used the psnr measure in the contributing papers of this thesis.

Having a ground truth and a quantitative error measure can also be used to exclude test-bias caused by parameter choices. We used the psnr measure to determine the optimal regularization parameter in the contributing papers, when possible. In this way we avoided choosing between the different regularization parameter picking methods mentioned above, since we base our λ -choice on ground truth comparison.

Some images with different types of simulated noise can be seen in [Figure 4.1](#). I listed the different error-measures below the images and I also included a zoom on a region of the noisy images.

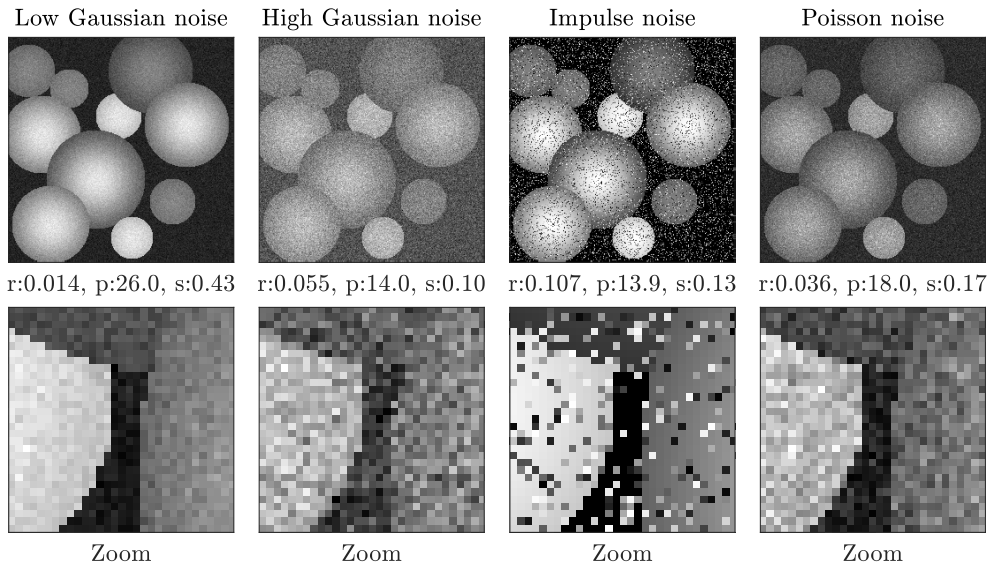


Figure 4.1: Comparison of different noise types and different error-measures. On top are noisy images with a description of noise-type above. In the middle error measures are written, where r denotes the relative 2-norm error, where p denotes the psnr error measure and s indicates SSIM. On the bottom row, zoom-ins of the noisy images are shown..

CHAPTER 5

Segmentation-Driven Reconstruction Methods

Image segmentation methods refers to a group of methods that aim to computationally partition images into two or more segments or classes. Historically segmentation methods have advanced from simple thresholding and clustering methods to much more complicated methods based on growing regions, active contours and variational methods.

Segmentation is a big topic within imaging science, but it covers a much larger range of practical applications. Segmentation technology becomes more and more popular in the industry. Today it is used in almost any kind of automation where cameras are involved. This could be within robot technology, medical diagnosis, production automation, surveillance, quality control, biometrics authentication, self-driving cars, etc. The range of applications is vast, and development of new mathematical methods in this field has also been increasing in the last few decades. In this chapter I will review a few segmentation methods and elaborate on the requirements for segmentation methods in general.

Pre-processing images before using a segmentation method is a very typical process, in fact many image segmentation methods include or suggest that denoising, e.g. by filtering, is carried out before using the segmentation method. This step is sometimes

referred to as image enhancement. Usually this segmentation aiding step is done by use of very simple methods that either does not remove all of the noise or leave artifacts, both of which can influence the quality of the subsequent segmentation.

Combining image reconstruction methods with image segmentation is an obvious idea that follows from pre-processing and segmentation preparing steps. I will mention some methods that has combined the segmentation and reconstruction into a single solvable problem in this chapter. I will also highlight some disadvantages that this strategy can have.

5.1 Image segmentation

The simplest image segmentation method is consist of thresholding an image based on the pixel-intensity information. The thresholding levels are parameters that can either be manually or automatically chosen, for instance from the histogram, or otherwise naturally given for some applications. Every pixel in the image is assigned to a class from the intensity solely. Otsu's method, see [77], is one of oldest methods for picking a thresholding level for an image. Otsu's method only separates an image into two segments, and in fact Otsu's method corresponds to $K = 2$ in K-means clustering, see [65]. Other classical segmentation methods are: The watershed method and region growing. The watershed method is presented in [11], and it separates regions by watershed lines based on an estimate of the local minima in an image. Region growing is similarly initiated by some seed point that are then grown, based on a specific criterion. These classical segmentation methods are relatively simple both in term of requirements and models, but also when considering their computational demand.

More advanced segmentation methods are for instance based on the use of Markov Random fields, see e.g. [42, 18]. These methods are graph based and they use neighborhood connectivity of the pixels. The level set methods are very popular segmentation methods and a lot of mathematical theory has been developed for these methods since they were first introduced in [76]. Active contour methods are based on deforming an initial contour around an object in the image, based on minimizing a specifically designed functional, see more in [57, 24].

Several variational methods have also been used for image segmentation, see [4] for an overview. Among these I will highlight the Mumford-Shah method introduced in [68]. This method regularizes an image by Tikhonov regularization, except along contours boundaries that are regularized by minimizing their length. In practice this model is difficult to minimize and instead many different relaxations of this model exist, e.g. [80]. The 0-norm regularization method mentioned in (3.7) is some times called the Potts-model, see [18], and can be regarded as a segmentation method. The Potts-model is related to the Mumford-Shah model, in fact it is sometimes called a

piecewise constant version of the Mumford-Shah model. As mentioned in [Section 3.2](#) solving the Potts-model problem is NP-hard and therefore a significant computational difficulty.

A great disadvantage of several of the above mentioned segmentation methods is that they are non-convex and hence uniqueness of the results are not guaranteed. Several of the methods, especially the simpler ones, also require some pre-processing for the methods work properly. Moreover, the segmentation methods has to deal with the typical mathematical modeling balance between complex and computationally heavy models and faster, but also inferior and sometimes insufficient models.

5.1.1 Requirements

The most basic requirement for segmentation methods is the intensity, which is typically given along with an image as it is. Another basic requirement for several segmentation methods is gradient information. If an image is corrupted, e.g. by noise, simply calculating a finite difference approximation of the gradient, and using this information for segmentation, could result in a highly unreliable segmentation. Neighborhood connectivity of pixels can also be a requirement. This is relatively simple to set-up, when a rule for how to choose a neighborhood is decided.

Initialization of the methods, e.g. of seed locations, can be crucial to final segmentation, especially when the methods are non-convex. Sometimes heuristic methods are used to initialize a segmentation method and the choice of the heuristic method can therefore have an essential impact on the segmentation result.

Another requirement, which is essential in some segmentation methods, is knowledge of the number of segments that is represented in an image, e.g. how many different materials types. Such information is not always naturally given, and it could cause a segmentation method to fail if it is specified wrongly.

5.2 Combined methods

Methods where segmentation is combined with other tasks, such as image reconstruction, are relatively new. The idea is to build a single model that connects the data directly to the segmented object, and solves the segmentation problem directly in this way. A typical reason for combining segmentation methods with other methods is to reduced segmentation errors due to propagation of artifacts. If a denoising method introduces an artifact in an image the subsequent segmentation could suffer from this, whereas a combined model problem could circumvent that the artifact was created in the first place. Reduced computational time can also be achieved by only having a single problem to solve. A disadvantage of the combined methods is that we might

not get the intermediate solution, which is also desired in some cases.

In the image processing community it was suggested to combine denoising and deblurring tasks with segmentation in [58]. Later structure-texture decomposition combined with denoising was introduced in [5, 45].

Within tomographic methods, manual segmentation is a typical pre-analysis step, and automation of this process is a big topic within segmentation. Therefore it is not surprising that several ways to combine segmentation and tomographic reconstruction is suggested in the literature. A combination of the Mumford-Shah segmentation with the CT-reconstruction method was suggested in [82]. A CT-reconstruction method, that only reconstructs a limited number discrete classes of an object is called the Discrete Algebraic Reconstruction Technique (DART), see more in [9]. A more recent method based on a combination of CT-reconstruction and the Potts segmentation model was introduced in [96]. Furthermore a method that reconstructs and segments the image simultaneously using Hidden Markov Radon Fields was introduced in [83].

The problem with these more advanced segmentation method is that they often become highly complex, and solving them requires a high computational cost, even considering parallelization and other efficiency improving techniques. Another disadvantage is that when we combine an otherwise convex reconstruction method with a non-convex segmentation method, we loose the desired uniqueness property.

5.3 Aiding segmentation

Thinking about image segmentation as a last step in a pipeline consisting of the steps: Image reconstruction, pre-processing and finally image segmentation, the idea of aiding the segmentation is similar to the idea behind the combined method. Instead of combining all of the steps, the first two steps, reconstruction and pre-processing, are combined while the computational effort is also moved from the segmentation to the reconstruction, but still having two separate steps. By doing so, the segmentation step could be reduced to a very simple step, possibly just a thresholding.

For such segmentation aiding, or *segmentation-driven*, methods, one can already include variational methods using TV-related regularizers. Also the Mumford-Shah combined with reconstruction can be seen as a segmentation-driven method. The segmentation-driven methods should drive the reconstruction in direction of the segmentation methods and hence supply one or more of the requirements listed in [Section 5.1.1](#). Other desired features of a segmentation-driven method are: Clear edges between regions and regions of constant intensity. In all of the papers contributing to this thesis, TV or TV-related regularization methods are proposed and used, therefore they can all be regarded as being segmentation-driven.

CHAPTER 6

Contributions

In this thesis, segmentation-driven reconstruction methods have been studied for different practical problems: tomographic reconstruction, image denoising and image deblurring. The proposed methods are segmentation-driven in the way that they reconstruct or restore objects and images such that the results have features that are desirable for simple segmentation methods.

The contributions of this thesis can be divided into three parts: The first part is related to phase contrast tomography. In this work we experimented and tested the advantages of going from a two stage reconstruction method to a one stage reconstruction method, in terms of the materials in the object and the amount of noise in the measurements. The reconstruction methods were regularized by total variation and hence most of the reconstruction results can be easily segmented using simple methods.

The main work of the second part is the proposal of a new regularization method that takes an offset from total generalized variation. The new method, *directional total generalized variation*, incorporates directional information about an object. We proved that this regularization method has the same desirable theoretical features as total generalized variation, and we furthermore demonstrated the advantages of using this segmentation-driven regularization method for deblurring and denoising different kinds of directional objects.

The third part of the contributions is based on decomposing or splitting a directional object simultaneously with a tomographic reconstruction. We proposed two reconstruction methods that directly segment or highly aid the segmentation process. We demonstrated how the two reconstruction methods perform and compare their on a

realistic sample consisting of fibres and cracks.

The articles that documents the work of this thesis are enclosed in the appendix. In this chapter I will give the context that is the foundation for our work for each of the three projects. After this I will describe the main outcomes and result and explain the impact of these results.

6.1 Phase contrast tomography

6.1.1 Context

Phase-Contrast Tomography (PCT) is an imaging method which in addition to the attenuation of X-rays utilizes the phase shift information of these electromagnetic waves. The extra information can be obtained in several ways, but the simplest method, *free-space propagation*, is very similar to CT. The only practical difference between free-space propagation PCT and CT is an increased object-to-detector distance.

PCT can provide a better contrast between materials that have very similar attenuation coefficients, i.e. that are usually difficult to distinguish from each other using standard CT. This is highly useful for many non-destructive materials science investigations. The contrast enhancing ability could also be used to reduce the X-ray dose, since a higher contrast can be attained from the phase shift information. PCT experiments has usually been restricted to synchrotron facilities, due to coherency requirements, but recent developments has made lab scale experiments possible, though with increased measurement noise and artifacts.

Reconstructing an object from phase contrast measurements is classically based on two stages. The first stage is a phase retrieval stage and the second stage is a tomographic reconstruction stage. In the phase retrieval stage the absorption and phase fields are retrieved for each projection from the measured intensity. The phase retrieval is typically carried out by linearizing the physical model and solving it by a simple inversion. The tomographic reconstruction is typically carried out by a filtered back-projection method.

Instead of having two separate stages, it has been suggested to combine these into a single stage. Furthermore using a segmentation-driven reconstruction method is also beneficial for many materials science experiments. Kostenko *et al* proposed to combine phase retrieval and reconstruction into a single problem, to be solved simultaneously by use of a TV-regularized variational method. This method was tested on simulated materials with artificial material indices and the combined method was not seen perform better than the two-stage method for noisy data. Therefore we found

it interesting to provide a rigorous test of this segmentation-driven reconstruction method for different realistic material types and of varying noise levels.

6.1.2 Relevant paper

Paper A: Noise robustness of a combined phase retrieval and reconstruction method for phase-contrast tomography

6.1.3 Outcome

In this work we carefully planned a comparison of the combined reconstruction method versus the two-stage method in physically realistic simulated experiments. The main goal of the comparison was to rule out as many influencing factors as possible, such that we could conduct a clear comparison between the two stage method and the combined one stage method.

The outcome of this work is threefold: First of all we demonstrated the performance of using PCT for low, medium and high absorbing phantoms, with material parts that have similar absorbing properties. The result of this test was a good performance for low to medium-low absorption. For highly absorbing objects the reconstructions were corrupted by artifacts and they had low distinguishability, which was expected since the linearization is only valid for low absorbing objects. Secondly we demonstrated that the combined method delivers results with less artifacts and better contrast between materials that have similar absorption properties. Finally we also demonstrated a very clear advantage of using the combined method for noisy data, where this reconstruction method was highly robust toward increasing noise.

In general, the combined method was seen to be as good or better for all the empirical tests, regardless of materials or the amount of noise. We believe that the artifacts that occur in the two-stage methods, and not in the combined method, were caused by errors introduced in the phase retrieval stage, but more investigation within this area is needed to bring more clarity.

The simulations with realistic material indices validates for which experiments phase contrast tomography is useful, and shows that a combined reconstruction method further enhances the reconstruction result. The noise robustness result of this work result could be of critical importance for pushing lab scale PCT experiments to real applications usage, since more artifacts and higher noise levels are typical there. Furthermore, the segmentation-driven regularization ensures reconstructions that are easily segmented by a simple thresholding.

6.2 Directional total generalized variation

6.2.1 Context

Regularization of inverse problems is a very useful technique for improving reconstructions within e.g. imaging science. Dozens of regularization methods has been developed from very general and widely applicable methods, to more specific and application-driven methods.

The choice of regularization method is typically based on prior information about the object that we regularize. Total variation (TV) is a very popular regularization method within image processing and imaging science and it is connected to a prior of piecewise constant objects. An extension to the TV regularization method is total generalized variation (TGV). The second order version of TGV is connected to a prior of piecewise affine objects. TGV of second order is more favorable than TV for natural images, and since piecewise constant objects are in fact also piecewise affine objects, second order TGV is superior to TV, though more computationally demanding. Moreover TV and TGV are convex and lower semi-continuous, which, from a variational problem perspective, are highly useful properties.

For many different practical applications directional texture is present. Seismic images and fibre materials are widely used and often have clear uni-directional texture. Applications of fibre materials are for example fuel cells with ceramic fibres, high speed communication cables with optical fibres and wind turbine blades constructed of glass fibres. This common feature of uni-directional texture is attainable and this can therefore be utilized by designing a regularization method that incorporates it.

Directional information has been incorporated in regularization methods such as TV in some cases by introducing an anisotropy in the discrete formulation of TV. The properties of corresponding continuous problem is interesting from a perspective of regularization theory and variational methods in general, but it has not yet been analyzed. Furthermore, advantages of incorporating directional information in higher-order derivatives have not been identified and documented.

6.2.2 Relevant papers

Paper B: Directional Total Generalized Variation Regularization

Paper C: Directional Total Generalized Variation Regularization for Impulse Noise Removal

6.2.3 Outcome

In this work the main focus is development of a new regularization method, directional total generalized variation (DTGV), that incorporates directional information as the name implies. We wanted to establish the mathematical theory of the functional itself and the theory related to using this as a regularizer. Moreover we wanted to demonstrate the improvement of using this regularizer for practical problems by a series of empirical experiments.

In paper [B](#) we have proposed a continuous extension of TV that incorporates directional information. This functional we have further generalized to any arbitrary integer order, by following steps similar to those that Bredies *et al* used to extend TV to TGV.

We have shown that DTGV possess the same properties as TGV, besides being isotropic. In paper [B](#) we have also shown that, based on some requirements of the noisy image and the forward operator, a unique solution exist for the variational problem consisting of an L^2 data-fitting term and second order DTGV as the regularization term.

In paper [C](#) we have proposed a robust and efficient method for estimating the main direction in images corrupted by Gaussian or impulse noise. The method is also demonstrated to work for images corrupted by both noise and blurring.

We proposed a discretized version of DTGV up to the second order, which is necessary in order to make the functional practically applicable for numerical experiments. Based on the discrete DTGV formulation we have conducted some empirical image restoration tests. In paper [B](#) we demonstrate the improvement of regularizing with DTGV opposed to TGV for denoising and deblurring directional objects corrupted by Gaussian noise. In paper [C](#) we show similar improvements when denoising and deblurring images corrupted by impulse noise.

The results of this work is a new regularization method, that has the same useful properties as well-established regularization methods for imaging problems. This regularization method delivers results that aid a subsequent segmentation, since it enforces objects that are directional and piecewise affine. We have given some examples of practical problems where this method can be useful and also empirically shown the significant improvements for several types of image restoration problems. This method is applicable for many other types of practical inverse problems and could, due to the desirable properties, also be useful within other fields where regularization is used, e.g. control.

6.3 Tomographic reconstruction of directional objects

6.3.1 Context

The use of computed tomography (CT) for non-invasively investigating the interior of objects has become omnipresent within technical sciences. Within materials science and product development there has been an increase in the use of CT for investigation and analysis.

The reconstruction process from X-ray attenuation measurements to a reconstructed object has been investigated a lot within the mathematics community. In the most basic case with a parallel beam measurement set-up, with a monochromatic X-ray source the problem is a mildly ill-posed linear inverse problem. This means, that not only filtered back-projection type methods are applicable for this problem, but in fact all kinds of methods for solving inverse problems.

Variational methods are widely used for solving inverse problems and they typically incorporate regularization as part of the method. Regularization methods are quite flexible and should be chosen according to what attainable prior information we have for the object. TV and TGV type regularization method has been shown to be highly useful for many different practical problems. Furthermore the directional regularization method mentioned above has been shown to be useful for objects with directional texture in general, for instance fibre materials.

Decomposition methods are examples of variational methods that aim to separate an object into different components according to different properties, for example it could be desirable to split oscillating texture parts from piecewise constant regions in an image. Infimal convolution is a way of decomposing an object into different parts using two, or more, functionals, e.g. some prior enforcing regularization terms. The idea is to choose two functionals that are different in terms of their connected priors such that each component will represent the part of the solution that best fits with each prior, and therefore also with the corresponding regularization method. Decomposition methods have previously been used for image denoising combined with simultaneous texture-cartoon decomposition. Decomposing of an object simultaneously with reconstruction it could be argued to be a highly segmentation-driven method.

Microlocal analysis of the CT problem has revealed that singularities in the object only propagate to the measured sinogram data if an X-ray is tangent to the singularity. This result is especially relevant for limited angle problems, where some singularities will be lost and some artificial singularities created, due to the limited scanning angles. This singularity propagation result could also be utilized to exclude singularities we do not want in a reconstruction.

Many different fibre materials are analyzed using CT, e.g. carbon fibre, glass fibres and optical fibres. A typical aim of non-destructive testing of fibres is crack-propagation investigation. In fibre materials, the cracks are often distinctive from the fibres and splitting these two components apart is an example of a practically useful decomposition challenge.

6.3.2 Relevant paper

Paper D: Tomographic Reconstruction Methods for Decomposing Directional Components

6.3.3 Outcome

We propose two CT reconstruction methods for reconstructing objects with texture along one main direction, but with parts that does not follow this prior. The aim of these methods are to handle both the object-parts that follow the main direction and also object parts the does not fulfil this prior. As a consequence of building a model that fulfill these requirements we propose to handle these different object parts by using different regularization terms for each of them.

The one method we proposed is based on the same strategy that has previously been used for combined image restoration and *decomposition*. We propose to decompose the object in two parts linearly and solve the minimization problem for both of these components simultaneously. The one component represents the directional texture and the prior for this component fits with a directional regularization method, e.g. directional total variation (DTV). The other component represents object parts that does not follow the main direction and in order to get a significant split of the components we make the assumption that this component follows the direction perpendicular to the main direction. If the first regularizer is DTV our empirical tests show that the difference between of using DTV in the perpendicular direction or just standard TV for the second regularizer are very similar. This means that the method is robust with respect to the width-parameter in the second DTV regularizer term, as long as the weight parameter is chosen according to the suggested bound. For fibres with cracks the regularizers should of course be chosen fittingly, but applications of this model goes beyond that example, since it could be applied to other directional object with non-directional parts. We desired that the model was convex and we therefore did not experiment with any non-convex regularizers for the second term.

The other reconstruction method we proposed, is based on *splitting* a directional object into a uni-directional part versus other all other parts in the object. For this method we split the data into two, according to measurement angles, and solve each part individually. The split is determined by the main direction of the object which should be known or estimated prior to using the method.

The advantage of this sinogram splitting method is that we leave out some data for each solution part, such that we only use data that include the singularities that we want to see. Since the problem is linear, the computational need is not increased by the split, but on the other hand it leaves us with two limited angle problems that we now have to handle. For such problems we typically need regularization in order to avoid artifacts, but we also tested with FBP for comparison. For the fibre-part we expected an object that is piecewise constant with texture along one main direction, so we used a DTV-regularized method to reconstruct it. For the example where we are looking for cracks in fibres, we chose to put no prior on the crack direction and therefore reconstructed it using a TV-regularized method. Furthermore we expected the cracks to be sparse and therefore we included L^1 -regularization on the crack part, besides TV-regularization.

For both methods the main texture direction is an essential parameter. We previously developed a method for determining the main direction in images, but we cannot use this on the sinogram data. In this work we therefore extended the idea to the CT-problem and proposed a noise-robust and efficient method for estimating the main direction in an object, only based on the sinogram data. We demonstrated the proposed direction estimation method and showed the noise robustness of this method for two different samples. We also demonstrated how DTV-regularization is advantageous to use for reconstruction of directional objects without the decomposition as an extra feature.

For both the sinogram splitting method and decomposition method we have shown different regularization results for an idealized fibre-crack-phantom. We used these tests to demonstrate how parameter choices of the two methods influence the solution. For the idealized phantom, the sinogram splitting method shows very promising results that clearly splits the fibre and all of the cracks in two parts. The results of using the decomposition method on the phantom are also very promising; The quality of the entire object reconstructions are better than the results achieved without the decomposition, and many of the cracks are present in the crack-component.

Finally we compared the two methods for a real phantom where we simulated the noisy measurements. For this carbon fibre sample the decomposition method was superior to the sinogram splitting method. Using the decomposition, opposed to the sinogram splitting, resulted in sharper edges, for both the fibres and the cracks, and furthermore the crack-part of the solution has a homogeneous background which makes subsequent crack-segmentation very easy.

The methods introduced in this work can be used in various types of testing where CT is used. Materials science is an obvious field where the outcome of our work can become highly useful tools. The demonstrations outline a fibre-crack sample where this for example could be used. Using any of the two reconstruction methods that we have proposed can be seen either as a directly combined reconstruction and segmenta-

tion or as highly segmentation-driven. The decomposition method is presented here in terms of CT-reconstruction, but it is not limited to this field, it could e.g. be used for image restoration or for a broad range of other inverse problems where directional objects are analyzed.

CHAPTER 7

Conclusions and Perspectives

Here I will sum up the most important results of this thesis and give some perspectives on a few interesting research topics that follows from our work.

For phase contrast tomography we demonstrated a clear advantage of going from a two-stage reconstruction method to a one-stage segmentation-driven reconstruction method. The one-stage combined method was seen to outperform the two-stage method in a series of realistic material simulations. Moreover, the combined method was seen to be significantly more robust toward high noise, which could be a big step toward making this technique more useful in lab-scale experiments.

In order to verify the results from these simulated experiments, real experiments, in either a synchrotron or using a special laboratory set-up, is needed. Furthermore, theoretical clarification that can explain why the combined one-stage reconstruction method outperforms the two-stage method could give a lot more insight and also be relevant for many other combined reconstruction methods. For the low photon count, i.e. high noise, problems it would be interesting to see if a more suitable data-fidelity term would further improve the results.

We proposed a regularization term that incorporates detectable directional information and can be used for segmentation-driven reconstruction methods. We demonstrated that this functional has desirable mathematical properties such as convexity and lower semi-continuity. This regularization method has been shown to be highly useful for directional objects, we demonstrated this in simulated experiments, where

images were corrupted by blurring and different types of noise. Incorporating the directional information improves the results significantly for denoising, deblurring and tomographic reconstruction tasks. We also proposed methods for detecting the main direction, both in images and directly from tomographic data.

Two extensions of this regularization method could be very interesting: An extension to locally varying directions, e.g. pixel-wise direction could make this method application for a much wider range of objects. Furthermore, a generalization of this technique to 3D would also be of use for many different practical problems. Incorporating directional information is not limited to the segmentation-driven total variation type methods. As we have shown the directional information can be incorporated through the divergence and gradient operators, and it can therefore easily be incorporated in e.g. Tikhonov regularization. In general, directional regularization has applicability for many other practical problems than the ones tested in this thesis, e.g. other image processing tasks such as inpainting and super-resolution or for other types of inverse problems.

The two reconstruction methods that we have proposed for computed tomography could be classified as either combined segmentation and reconstruction, or as highly segmentation-driven reconstruction methods. These reconstruction methods splits a directional object in two parts, according to the main texture-direction, simultaneously with reconstructing it. Based on the direction, estimated by our proposed method, either the data is split in two sets, or the object is split by an infimal-convolution type decomposition method. A clear application for this method could be splitting cracks from fibres. This is a typical analysis task for different types of fibre materials and our simulated experiments has shown very promising results for this application.

An extension of this method to 3D and real experiments with a ground truth phantom for comparison could be very interesting to verify the practical usefulness of the methods. Reducing the number of tunable parameter can highly improve these methods, but requires some analysis or some assumptions on the object. Both of the introduced reconstruction methods have advantages and disadvantages, so combining the best parts from each method, and creating a completely superior method, can be a very interesting future investigation.

APPENDIX **A**

Noise robustness of a combined phase retrieval and reconstruction method for phase-contrast tomography

In Journal of Optical Society of America A, vol. 33, 2016, pp. 447-454, Washington, DC, United States of America.
doi:[10.1364/JOSAA.33.000447](https://doi.org/10.1364/JOSAA.33.000447)

R. D. Kongskov, J. S. Jørgensen, H. F. Poulsen and P. C. Hansen

Copyright 2017 The Optical Society

Noise robustness of a combined phase retrieval and reconstruction method for phase-contrast tomography

RASMUS DALGAS KONGSKOV,^{1,*} JAKOB SAUER JØRGENSEN,¹ HENNING FRIIS POULSEN,² AND PER CHRISTIAN HANSEN¹

¹Department of Applied Mathematics and Computer Science, Technical University of Denmark, Richard Petersens Plads, Building 324, 2800 Kongens Lyngby, Denmark

²Department of Physics, Technical University of Denmark, Fysikvej, Building 311, 2800 Kongens Lyngby, Denmark

*Corresponding author: rara@dtu.dk

Received 4 September 2015; revised 19 January 2016; accepted 15 January 2016; posted 20 January 2016 (Doc. ID 249501); published 4 March 2016

Classical reconstruction methods for phase-contrast tomography consist of two stages: phase retrieval and tomographic reconstruction. A novel algebraic method combining the two was suggested by Kostenko *et al.* [Opt. Express 21, 12185 (2013)], and preliminary results demonstrated improved reconstruction compared with a given two-stage method. Using simulated free-space propagation experiments with a single sample-detector distance, we thoroughly compare the novel method with the two-stage method to address limitations of the preliminary results. We demonstrate that the novel method is substantially more robust toward noise; our simulations point to a possible reduction in counting times by an order of magnitude. © 2016 Optical Society of America

OCIS codes: (100.6950) Tomographic image processing; (100.5070) Phase retrieval; (100.3190) Inverse problems; (110.6960) Tomography; (000.3860) Mathematical methods in physics.

<http://dx.doi.org/10.1364/JOSAA.33.000447>

1. INTRODUCTION

With upcoming high-brilliance x-ray sources, new phase-contrast tomography (PCT) methods have gained widespread use [1]. Among these is the free-space propagation method [2,3], with the advantage that no additional optical elements such as analyzer crystals or gratings are required. Compared with conventional absorption contrast, phase contrast may provide adequate contrast at lower dose rates, thus allowing segmentation of objects comprising two or more materials with nearly the same electron density (e.g., [4]). For a comparison of variants of free-space propagation methods in general, see [5].

First experiments were performed using holo-tomography, requiring the combination of measurements from several sample-to-detector distances [6], but today highly successful reconstructions are often possible using a single distance, e.g., in the area of paleontology [7]. This is experimentally convenient but also remarkable, as the information content is obviously reduced. In fact, reconstruction with the single-distance setup is typically based on the work by Paganin *et al.* [8], assuming proportionality between the absorption and the phase shift. Research into the limitations of this so-called duality method will benefit experimental planning.

The standard approach to PCT reconstruction is a two-stage procedure. In the first stage, the phase and absorption fields are determined for each projection using a phase-retrieval algorithm. In the second stage, a classical algorithm is used to compute reconstruction based on the projection fields.

Recently, Kostenko *et al.* proposed a combined approach [9,10], which, in several of their simulated experiments with noise-free data, performs better in terms of reconstruction error. However, for simulated noisy data the combined method is outperformed by the two-stage method. Both methods are tested on simulated data with artificial material indices; therefore, it is unclear if the combined method performs better than the two-stage method for realistic samples, for different material types, and for varying noise levels.

In this paper, we provide a careful numerical simulation study of the combined duality method, comparing it with the two-stage approach. The use of regularization is key to obtaining high-quality reconstruction, and we focus on the use of total variation (TV) [11] as the regularizer. Many samples in materials science and geoscience comprise discrete objects (grains, fibers, cracks), and edges naturally lead to high phase contrast in the free-space propagation method. Using a polycrystal with small density variations as a phantom and with

simulated noise, our simulations aim to carefully compare the reconstruction capabilities of the two methods.

After a review of a classical PCT reconstruction method and the combined method, we present our numerical implementation. In simulations with realistic material parameters, we perform a comprehensive comparison of the two methods with respect to different material parameters of increasing difficulty and to the robustness toward noise.

Our results show that the combined method produces improved reconstructions across the range of low to high-absorption materials with small absorption contrast. Furthermore, as the simulated noise level is increased, reconstructions from the combined method show much greater robustness to the noise. This could be of critical importance in practical applications where noise is always a concern.

2. DEFINITIONS AND FORWARD MODEL

In this section, we briefly review the underlying definitions and models. To simplify the presentation and the numerical experiments, we consider only 2D problems.

Scalar functions are denoted with italic, e.g., u , B or φ . Vectors are denoted with subscript v , e.g., x_v or B_v . Matrices are denoted with bold uppercase, e.g., \mathbf{A} or \mathbf{F} , and operators with uppercase calligraphic letters, e.g., \mathcal{A} and \mathcal{F} . Throughout, $\|\cdot\|$ denotes the vector 2-norm.

A. Definitions

The Fourier transform \mathcal{F} of a 1D signal f is denoted with \hat{f} :

$$\hat{f}(\omega) = \mathcal{F}(f(x)) = \int_{-\infty}^{\infty} f(x) e^{-2\pi i \omega x} dx. \quad (1)$$

The independent frequency variable is ω , and the complex unit is denoted as $i = \sqrt{-1}$. The Radon transform \mathcal{R} of a 2D signal $f(x_1, x_2)$ is defined by

$$[\mathcal{R}f](t, \theta) = \int_{-\infty}^{\infty} f(t \cos(\theta) - \tau \sin(\theta), t \sin(\theta) + \tau \cos(\theta)) d\tau. \quad (2)$$

Here, θ is the angular variable and t is the translational variable, perpendicular to line integration direction, in other words, the coordinate variable on the 1D detector.

A discrete linear inverse problem can be formulated for absorption-based computed tomography (CT) by discretizing a 2D object into N by N square pixels with pixel values stacked into a vector u_v . The Radon transform is discretized using the line-intersection method and represented using a system matrix \mathbf{A} with elements a_{mn} of the path length of x-ray m through pixel n . Letting b_v denote the discrete projection data, the discrete linear inverse problem can be written

$$\mathbf{A}u_v = b_v. \quad (3)$$

For more details, see [12].

B. Free-Space Propagation Model

Different experimental PCT setups exist (see [1] for an overview). In the present work, we focus on the free-space propagation method, Fig. 1, which, in some sense, is the simplest because it does not require analyzer crystals, gratings, or likewise.

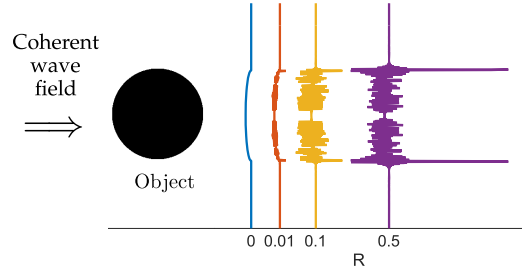


Fig. 1. 2D sketch of free-space propagation setup. The intensity profile is shown as function of increasing detector distance R . In the contact plane $R = 0$, only absorption contrast is visible. In the near-field region of interest here, both absorption and phase contrast contribute to the intensity.

The setup is similar to the standard CT scanning setup, with the added requirement that the x-ray source is partly coherent.

In free-space propagation PCT, phase shifts of x-ray waves are magnified as the object-to-detector distance increases. Based on intensity measurements at the detector, the task is to reconstruct the absorption index and the refractive index decrement of the object.

For free-space propagation PCT, the measured intensity data in the Fresnel region is related to the material properties through a nonlinear propagation model. For a 2D object with absorption index $\delta(x_1, x_2)$ and refractive index decrement $\beta(x_1, x_2)$, the corresponding projections $B(t, \theta)$ and $\varphi(t, \theta)$, here called *absorption* and *phase shift*, can be modelled as line integrals along the x-ray propagation [5]:

$$B_\theta(t) = \frac{2\pi}{\lambda} [\mathcal{R}\beta](t, \theta), \quad (4)$$

$$\varphi_\theta(t) = -\frac{2\pi}{\lambda} [\mathcal{R}\delta](t, \theta). \quad (5)$$

Here, λ is the x-ray wavelength and \mathcal{R} is the Radon transform. Based on the absorption and phase shift, the measured intensity I_θ^R is modeled as the squared absolute value of the convolution of the transmittance T_θ and the Fresnel propagator P^R :

$$T_\theta(t) = \exp(-B_\theta(t) + i\varphi_\theta(t)), \quad (6)$$

$$P^R(t) = -\frac{i}{\lambda R} \exp\left(\frac{i\pi}{\lambda R} |t|^2\right), \quad (7)$$

$$I_\theta^R(t) = |T_\theta(t) \star P^R(t)|^2. \quad (8)$$

Here, R is the object-to-detector distance, $|\cdot|$ the absolute value and \star the convolution operator.

Discretization of the domain, and, hence, the object of interest into $N \times N$ pixels, gives us discrete versions of the material parameters β and δ . A single index notation is introduced, $n = i + (N-1)j$, for $i, j = 1, 2, \dots, N$, so $n = 1, 2, \dots, N^2$, which gives two column vectors, β_v and δ_v , with element index n . Using the discrete Radon transform in Eq. (3), we define discretized versions of B_θ and φ_θ :

$$B_v = \frac{2\pi}{\lambda} \mathbf{A}\beta_v, \quad (9)$$

$$\varphi_v = -\frac{2\pi}{\lambda} \mathbf{A} \delta_v. \quad (10)$$

This leads to discrete versions of the transmittance and the Fresnel propagator and from those the intensity I_v^R :

$$T_v = \exp(-B_v + i\varphi_v), \quad (11)$$

$$P_v^R = -\frac{i}{\lambda R} \exp\left(\frac{i\pi}{\lambda R} |t_v|^2\right), \quad (12)$$

$$I_v^R = |T_v \star P_v^R|^2. \quad (13)$$

Here, \exp and $|\cdot|^2$ denote element-wise operations and \star denotes the discrete convolution. In practice, the discrete convolution is done in Fourier space.

3. RECONSTRUCTION METHODS

In this section, we review the two methods that we compare, namely, a classical two-stage method and a combined method presented by Kostenko *et al.* Both methods are equipped with TV regularization, which is described last.

A. Two-Stage Method

For absorption CT, the measured intensity data can be directly related to the material properties, i.e., the attenuation coefficient, by Lambert–Beer’s law [12]. For PCT, the intensity measurements are related to the material properties through the nonlinear propagation model Eqs. (4)–(8). The standard reconstruction process for PCT is a two-stage procedure, consisting of a *phase retrieval* stage and a *tomographic reconstruction* stage.

Different phase retrieval methods have been suggested and investigated in the literature. An introduction to, and a comparison of, some of them can be found in [5,13,14]. Following the work by Kostenko *et al.* [9,10,15], we focus on the contrast transfer function (CTF) method, which is based on an assumption of low absorption and which is derived from the expression of the intensity given in Eq. (8). Based on a Taylor expansion of the transmittance function Eq. (6), a CTF model that is linear in B and φ can be derived in Fourier space [6].

For the case of a single detector distance and the so-called duality version of the CTF model with proportionality constant $\sigma = -\delta/\beta$, we have

$$\hat{I}^R(\omega) \approx [2\sigma \sin(\pi\lambda R|\omega|^2) - 2 \cos(\pi\lambda R|\omega|^2)]\hat{B}(\omega) + \delta_{\text{Dirac}}(\omega). \quad (14)$$

Here, δ_{Dirac} is the Dirac delta function and ω denotes the spatial frequency. For p being the physical size of a detector pixel, the sampling distance becomes $F_s = 1/p$ and, hence, $\omega \in [-\frac{F_s}{2}, \frac{F_s}{2}]$. Introducing discrete frequency values ω_m , the CTF method can be formulated as a discrete linear inverse problem:

$$\hat{I}_v^R = \mathbf{W}_{\text{TSD}} \hat{B}_v, \quad (15)$$

$$\mathbf{W}_{\text{TSD}} = -2\mathbf{C}^R + 2\sigma\mathbf{S}^R, \quad (16)$$

where \mathbf{C}^R and \mathbf{S}^R are diagonal matrices with m th diagonal elements $\cos \psi_m$ and $\sin \psi_m$, respectively, with

$$\psi_m = \pi\lambda R|\omega_m|^2, \quad m = 1, 2, \dots, M. \quad (17)$$

For the two-stage method based on the CTF duality method, we use the name TSD.

The phase-retrieval stage of this method consists of solving Eq. (15) for \hat{B}_v , followed by an inverse Fourier transform and then solving Eq. (9) for β_v . Because β_v is assumed to be proportional to δ_v for this method, we can easily find δ_v afterward.

Following the phase-retrieval stage is a stage where a CT reconstruction method is used to compute the object of interest. Typically, CT reconstructions are carried out by using classical methods such as filtered backprojection (FBP) [12] or the algebraic reconstruction technique (ART) [16].

B. Algebraic Combined Method

Methods that combine the phase-retrieval stage and the reconstruction stage have been proposed with different aims. In [17] a filtered backprojection type algorithm is derived and tested while in [9] an *algebraic* combined model is presented and tested, showing promising preliminary results.

In [9], Kostenko *et al.* also suggested that the standard phase-retrieval techniques could benefit from using the redundancy within an entire sinogram rather than just being based on the individual projections.

The term “algebraic combined” in [9] refers to a combination of the linear operators, \mathbf{A} , describing the discrete Radon transform, \mathbf{F} , the discrete Fourier transform, and \mathbf{W}_{TSD} of the linear phase retrieval method, i.e.,

$$\mathbf{W}_{\text{ACD}} = \frac{2\pi}{\lambda} \mathbf{W}_{\text{TSD}} \mathbf{F} \mathbf{A}. \quad (18)$$

The discrete Fourier transform is introduced because it is computationally convenient to formulate the phase-retrieval model as a matrix multiplication in Fourier space. The algebraic combined method based on the duality version of the CTF method works on the resulting linear system:

$$\hat{I}_v^R = \mathbf{W}_{\text{ACD}} \beta_v. \quad (19)$$

This combined reconstruction method is called the algebraic combined duality method (ACD).

C. Total Variation Regularization

In absorption CT, TV regularization has been shown to be advantageous for objects with piecewise constant material parameters [18,19]. TV regularization preserves edges while smoothing away noise inside homogeneous regions. For the discrete linear problem in Eq. (3), we formulate TV regularization with regularization parameter $\alpha \in \mathbb{R}^+$ as

$$z_v^\alpha = \underset{u_v}{\operatorname{argmin}} \left\{ \|\mathbf{A}u_v - b_v\|^2 + \alpha \sum_{n=1}^{N^2} \|\mathbf{D}_n u_v\| \right\}. \quad (20)$$

Here, n is the pixel index, N^2 is the total number of pixels, assuming a square domain, and $\mathbf{D}_n u_v$ is the local finite difference gradient at pixel n .

Many objects from materials science, which would be desirable to analyze with PCT, have the property that they have approximately piecewise constant material parameters, e.g., in the form of grains. With this motivation Kostenko *et al.* proposed to incorporate TV regularization into both the TSD and ACD methods, i.e., in Eqs. (15) and (19).

In the present work, we also consider TV regularization for both methods, and in the remainder of the article by TSD and ACD, we refer to the TV-regularized problems. In a direct assessment of the effect of combining linear operators in ACD, and not the effect of TV regularization itself, we find it most appropriate to employ TV regularization also in TSD. We note that one motivation for ACD is precisely the use of regularization, which, through the combination of linear operators, regularizes the entire reconstruction problem including the phase-retrieval step. This is in contrast to the TV regularized two-stage method where only the latter reconstruction step is regularized, leaving the sensitive phase-retrieval stage unregularized.

4. OUR CONTRIBUTIONS

In [9], Kostenko *et al.* compared TV-regularized ACD and TSD and demonstrated improvements obtained by ACD in terms of root-mean-square error in most of their simulation experiments. We find that their pioneering results indicate a large potential for ACD; however, we also point to several aspects in which the provided numerical evidence of reconstruction improvements by ACD may be improved:

1. The positive results for ACD are for test images with one specific choice of material parameters that appears to not be motivated from physical materials. Thus, it remains open whether clear improvements can be seen for test images with physical material parameters.
2. The positive results for ACD are for noise-free data. In fact, in a simulation study with noisy data, Kostenko *et al.* find the TSD to be superior. Only one noise level is considered; thus, it remains unclear whether the combination of phase retrieval and reconstruction stages leads to a more noise-robust method.
3. In their implementation of the optimization algorithm to solve the TV-regularized problem, Kostenko *et al.* [9] describe that they stop the iterative algorithm when the relative change in the objective function value from one iteration to the next is smaller than 10^{-5} . This is an intuitive choice, however well-known in the field of optimization to be heuristic and not guarantee closeness to the solution. This is because the iterative algorithm may occasionally take short steps while still far from the solution. This means that we cannot be sure that the shown reconstructions are indeed accurate TV solutions but may be arbitrary intermediate images produced by the iterative algorithm. In fact, this problem might affect their conclusion that TSD is more robust to noise than ACD.

In the present work, we address all of these three problems. Regarding the third problem, we implement in our optimization algorithm a stopping criterion that does ensure convergence to the TV-regularized reconstruction, thereby removing any doubt whether the numerical solution returned by the algorithm is in fact the sought-after TV-regularized solution.

We address the first and second problems by providing two sets of carefully designed simulation experiments. The first set compares TSD and ACD on test images with a range of physical material parameters, while the second compares TSD and ACD with respect to increasing amounts of noise.

To make the most direct and fair comparison between TSD and ACD, we employ TV regularization for both and apply the same optimization algorithm with the same stopping criterion.

Before proceeding to the results of the comparisons, we describe in the next section our implementation details.

5. IMPLEMENTATION

The system matrix \mathbf{A} in Eqs. (9) and (10) is large and sparse. This means that it can often be stored in the memory of a standard modern laptop. For the ACD method, the dense matrix \mathbf{F} makes the combined system matrix dense, thus making it not feasible to store in memory. We circumvent the problem by a matrix-free implementation, in which the applications of the forward operator and its conjugate transpose are done without explicitly forming the matrices.

When solving the reconstruction problems in Eqs. (9), (10), and (19), we impose TV-regularization in Eq. (20). Solving such large-scale problems requires efficient algorithms. We chose to implement the Chambolle–Pock (CP) algorithm [20,21] because it was shown to converge faster than, e.g., the FISTA method [21], when solving problems of the form Eq. (3). Moreover, the CP algorithm can be well suited in the context of CT [22].

Our implementation is mainly based on algorithm 4 in [22], modified by the adaptive parameter approach presented in algorithm 2 in [23]. This modified approach introduces a primal residual $p^{(k)}$ and a dual residual $d^{(k)}$ for iteration k . As mentioned in [23], these residuals can also be used to define a stopping criterion because, for the CP algorithm, we have that

$$\lim_{k \rightarrow \infty} \|p^{(k)}\|^2 + \|d^{(k)}\|^2 = 0. \quad (21)$$

We implemented a stopping criterion of the form

$$\|p^{(k)}\|^2 + \|d^{(k)}\|^2 < \tau (\|p^{(1)}\|^2 + \|d^{(1)}\|^2) \quad (22)$$

for a user-defined tolerance τ . In all of our numerical experiments, τ was set to 10^{-6} .

The reconstruction stage of TSD involves multiplication with \mathbf{A} and its transpose in each iteration. The ACD method requires, in each iteration, additional FFTs and multiplications with the diagonal matrix \mathbf{W} , but both operations are much less computationally demanding than the multiplications with \mathbf{A} and, hence, the computational overhead in an ACD iteration, compared with TSD, is small.

All implementations and simulations are carried out in MATLAB, and the implemented code is available for download at [24]. We also use the function `phantomgallery` from the AIR Tools package, Version 1.3 [25], and the function `parbeam` from the Projector-Pack package, Version 0.2 [26].

6. SIMULATION RESULTS

We compare the TSD and ACD methods across different material parameters and increasing noise levels. The comparisons rely on simulated data, carefully modelled to resemble data from a real physical setup. Reconstructions are assessed in terms of achievable quality, compared with the ground truth and between the methods.

A. Experimental Setup

The simulated experiments are inspired by materials science where mappings of structures on a micrometer scale are desired.



Fig. 2. 2D phantom with a background material (black) and two different grain materials (gray and white).

For polycrystalline materials, the structures are made up of *grains*; to mimic this, we use a phantom that resembles grain structure consisting of three different materials. The phantom, which is shown in Fig. 2, consists of one background material and grains of two different materials, all of which are described by indices β and δ . Indices of the used materials are listed in Table 1. If nothing else is mentioned, polycarbonate is used for the background material.

Our setup allows us to simulate free-space propagation PCT experiments and compare reconstruction methods. In our simulations, we choose specific settings that are realistic for real physical experiments on a laboratory x-ray CT scanner. The chosen parameters are presented in Table 2. To make the simulated data more realistic, Poisson distributed noise is used to perturb the measured intensity.

In addition to the settings in Table 2, the duality method requires a qualified guess on the proportionality constant σ between β and δ . This has, for all simulations, been chosen as the exact proportionality for the grain material with the smallest β , e.g., for the first row in Fig. 3 $\sigma = -1.95 \cdot 10^4$. Experimental testing with different choices of σ have shown that the impact of changing σ , within $\pm 20\%$ from the exact value, was negligible.

In our simulations, we want to make a fair comparison between all the methods; therefore, the regularization parameter was always chosen empirically. The regularization parameter was chosen for each of the simulations in order to achieve the “best” possible reconstruction. The “best” reconstruction is in this work is measured by two different means: A relative error measure,

$$E = \|u - u^*\| / \|u^*\|, \quad u^* = \text{original}, \quad (23)$$

Table 1. Absorption Index β and Refractive Index Decrement δ for 40 keV X Rays for the Simulated Materials. From [27]

Material	β	δ
Polycarbonate ($\text{C}_{16}\text{H}_{14}\text{O}_3$)	$8.43 \cdot 10^{-12}$	$1.64 \cdot 10^{-7}$
Carbon (diamond)	$1.90 \cdot 10^{-11}$	$4.55 \cdot 10^{-7}$
Magnesium	$1.15 \cdot 10^{-10}$	$2.22 \cdot 10^{-7}$
Aluminium	$2.32 \cdot 10^{-10}$	$3.37 \cdot 10^{-7}$
Silicon	$2.68 \cdot 10^{-10}$	$3.01 \cdot 10^{-7}$
Iron	$6.42 \cdot 10^{-9}$	$9.54 \cdot 10^{-7}$
Copper	$9.96 \cdot 10^{-9}$	$1.06 \cdot 10^{-6}$

Table 2. Parameters Used in Simulations

Parameters	Settings
Object	2D and 200×200 pixels, pixel size $1 \mu\text{m}$
X ray	Energy 4 keV
Source	Wavelength $\lambda = 0.31 \text{ \AA}$
Photons	$N_0 = 10^5$ photons incident on object, average, per pixel, per projection
Distance	$R = 0.5 \text{ m}$
Detector	Pixel size of $1 \mu\text{m}$, 572 pixels
Projections	360 angles $\theta \in [0^\circ, 180^\circ]$

and a visual comparison where sharp edges are favored. In the figures with the reconstructions, we list the specific regularization parameter choices. Parameter-choice methods purely based on the data are well described in the literature (see, e.g., [28]).

The reconstructions are visualized as images using gray-scale color range $[0.9 \cdot \min(u^*), 1.1 \cdot \max(u^*)]$; intensity values outside are truncated to this range.

B. Effects of Material Properties

The simulated phantom is varied with materials ranging from low-absorbing material to higher absorbing material, i.e., from low β to higher β . The two-grain materials are chosen such that they have indices numerically close to each other because distinction between similar materials is the more challenging case in practical applications. Increasing the absorption will violate the low absorption assumption, which is part of the CTF model derivation; thus, higher absorption is also expected to increase the difficulty of the reconstruction problem. The reconstructions from our simulated experiments with materials of increasing absorption index are presented in Fig. 3.

For these four experiments the ACD method is generally seen to produce as good or better reconstructions than the TSD method, in terms of the error measure E . The TSD results are all visually more blurry and with less sharp edges compared with the ACD results, even though both methods utilize the same TV-regularization method. In the process of choosing the “best” regularized reconstruction from a series of reconstructions (not shown here), it became clear that the TSD reconstructions were corrupted by artifacts and/or noise to a higher degree than the ACD reconstructions. Of the four TSD reconstructions in Fig. 3, this is what causes the reconstructions to be more blurred because we gave more emphasis on the regularization term in order to compensate for noise and artifacts. We believe that the artifacts are due to the errors introduced in the phase retrieval stage.

For the experiments with low absorption, in the first row of Fig. 3, distinction between the different materials is clear for both methods. The ACD reconstruction has sharper edges and a lower error measure than the TSD reconstruction.

For the silicon-magnesium and the silicon-aluminium experiments, in the second and third row, materials with similar chemical structures are seen to be more difficult to distinguish, as expected. The ACD method again produces reconstructions with sharper edges and a lower error measure. For the silicon-aluminium reconstructions in row three, distinguishing between silicon and aluminium is difficult for both methods,

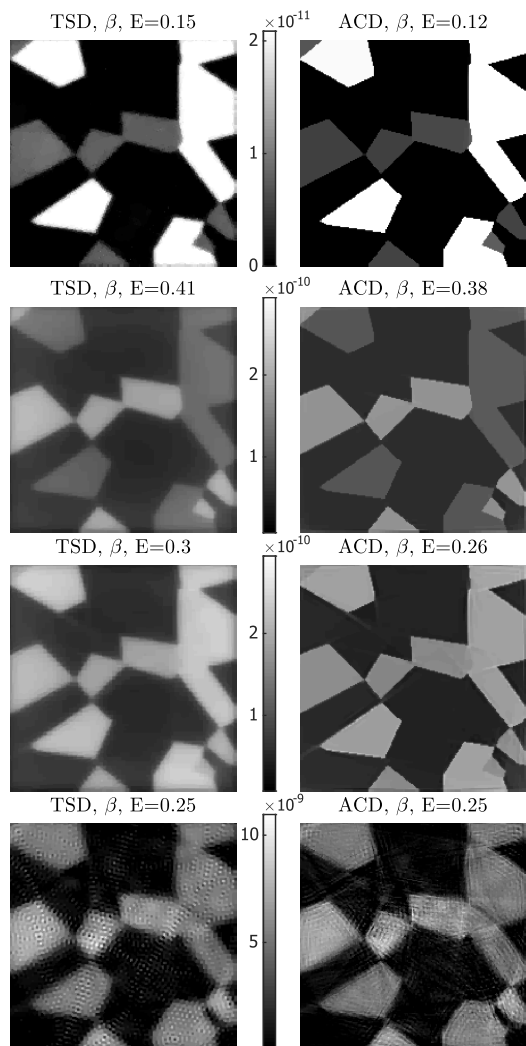


Fig. 3. Simulations with different materials. First row: nonabsorbing and nonrefracting background, grains of polycarbonate and carbon in diamond form (highest β) and regularization parameters $\alpha_{\text{TSD}} = 0.01$, $\alpha_{\text{ACD}} = 120$. Second row: grains of silicon (highest β) and magnesium and regularization parameters $\alpha_{\text{TSD}} = 0.1$, $\alpha_{\text{ACD}} = 110$. Third row: grains of silicon (highest β) and aluminium and regularization parameters $\alpha_{\text{TSD}} = 0.12$, $\alpha_{\text{ACD}} = 112$. Fourth row: grains of copper (highest β) and iron and regularization parameters $\alpha_{\text{TSD}} = 6$, $\alpha_{\text{ACD}} = 5$. The error measure E is defined in Eq. (23).

and alternative methods using measurements from two more or more distances could improve these results.

In the experiments with high absorbing materials, the reconstructions are highly affected by artifacts, such that distinction among background, grain, and artifact is difficult. In addition, the edges in the reconstructions are more blurry. Error measures of the form of Eq. (23)—no matter which norm is used—are

not well suited for measuring the quality of edges in a reconstruction (for example, a reconstruction with blurred edges can still have a low error E if the background is correctly reconstructed). For this reason, we also need the visual inspection of the reconstructions.

The ACD method is computationally more demanding than the TSD method because a larger number of iterations is needed to achieve the same solution accuracy. In the cases studied here, 1.4–6.5 times more iterations were needed for

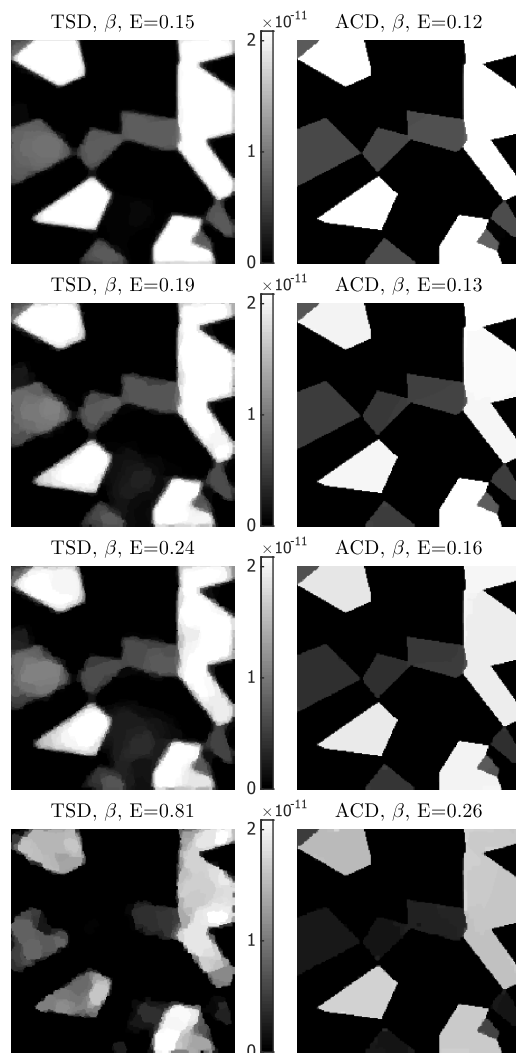


Fig. 4. Simulations for increasing data noise, i.e., decreasing number of photons N_0 . Nonabsorbing and nonrefracting background. Grains of polycarbonate and carbon in diamond form (highest β). First row $N_0 = 5 \times 10^4$, second row $N_0 = 10^4$, third row $N_0 = 5 \times 10^3$, and fourth row $N_0 = 10^3$, photons per pixel. Regularization parameter α for the TSD method from top to bottom were [0.03, 0.05, 0.08, 0.14] and for the ACD method [100, 140, 170, 300].

the ACD method when using the stopping criterion in Eq. (22).

C. Effect of Noise

The reconstructions from simulated experiments with a decreasing number of recorded photons, and hence increasing noise levels, are presented in Fig. 4. The error measure E is plotted for increasing N_0 (cf. Table 2) in Fig. 5. Using Otsu's simple thresholding segmentation method [29] on the reconstructions, the segmentation errors,

$$E_s = \text{\#misclassified pixels}/\text{\#pixels}, \quad (24)$$

are calculated and plotted against N_0 in Fig. 6.

The TSD reconstructions are seen to deteriorate as N_0 decreases (and the relative noise increases), where the grains of the lowest absorbing material closest to the object center become indistinguishable from the background (cf. the bottom row in Fig. 4). The edges become blurrier, and misclassification of the grains is likely to occur. The error measure increases drastically to a limit where the reconstructions are unreliable. We believe that errors, such as artifacts, from the first stage causes the second stage to produce these deteriorated results.

ACD reconstructions show much greater robustness to the noise: edges remain sharp, materials can be distinguished, and the error varies slowly with N_0 . For the problems with higher relative noise (smaller N_0), the polycarbonate grains can be visually difficult to distinguish from the background in the chosen

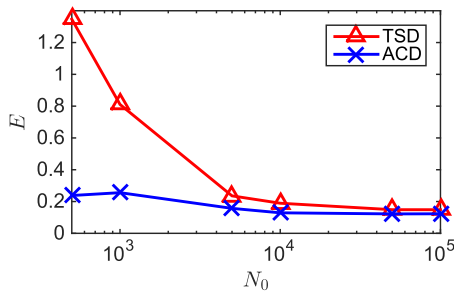


Fig. 5. Relative reconstruction error E for increasing number of photons N_0 , i.e., decreasing noise in the data.

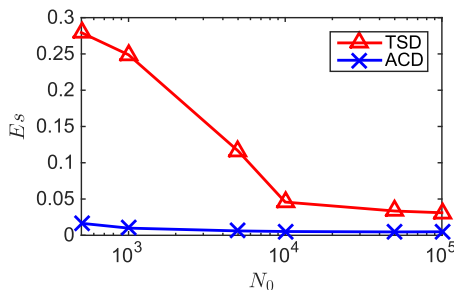


Fig. 6. Segmentation error E_s for increasing number of photons N_0 , i.e., decreasing noise in the data.

gray scale; though, numerically, the difference is still distinct as validated by the low segmentation errors in Fig. 6.

7. CONCLUSION

The simplicity of the geometry in the free-space propagation, one sample-detector distance approach makes it attractive for many experiments, including those where speed of data acquisition or dose is a limitation. Likewise, experience has shown that total variation (TV) regularization works well for absorption or phase contrast tomography on a large class of materials comprising disjunct phases, cracks, pores, etc.

The outcome of the simulations performed here is that the number of photons required to compute a reconstruction of a certain quality can be reduced substantially, and the combined reconstruction method is therefore of general interest to the x-ray (and neutron) imaging community. We emphasize that the suggested combined method is more computationally demanding than the classical two-stage method and, hence, less suitable for on-line or real-time processing.

Funding. European Research Council (ERC) (291321, 291405).

Acknowledgment. The authors thank A. Kostenko and J. Batenburg for insightful discussions and for sharing their work and code on phase-contrast tomography. We also thank M. S. Andersen for discussions related to numerical optimization and Y. Dong for discussions about image processing in general.

REFERENCES

1. A. Bravin, P. Coan, and P. Suortti, "X-ray phase-contrast imaging: from pre-clinical applications towards clinics," *Phys. Med. Biol.* **58**, R1–R35 (2013).
2. P. Cloetens, R. Barrett, J. Baruchel, J.-P. Guigay, and M. Schlenker, "Phase objects in synchrotron radiation hard X-ray imaging," *J. Phys. D* **29**, 133–146 (1996).
3. K. A. Nugent, T. E. Gureyev, D. F. Cookson, D. Paganin, and Z. Bamea, "Quantitative phase imaging using hard X-rays," *Phys. Rev. Lett.* **77**, 2961–2964 (1996).
4. L. Salvo, P. Cloetens, E. Maire, S. Zabler, J. J. Blandin, J. Y. Buffière, W. Ludwig, E. Boller, D. Bellet, and C. Josserrond, "X-ray microtomography an attractive characterisation technique in materials science," *Nucl. Instrum. Methods Phys. Res. Sect. B* **200**, 273–286 (2003).
5. M. Langer, P. Cloetens, J.-P. Guigay, and F. Peyrin, "Quantitative comparison of direct phase retrieval algorithms in in-line phase tomography," *Med. Phys.* **35**, 4556–4566 (2008).
6. P. Cloetens, W. Ludwig, J. Baruchel, D. Van Dyck, J. Van Landuyt, J. P. Guigay, and M. Schlenker, "Holotomography: Quantitative phase tomography with micrometer resolution using hard synchrotron radiation X-rays," *Appl. Phys. Lett.* **75**, 2912–2914 (1999).
7. P. Tafforeau, R. Boistel, E. Boller, A. Bravin, M. Brunet, Y. Chaimanee, P. Cloetens, M. Feist, J. Hoszowska, J.-J. Jaeger, R. F. Kay, V. Lazzari, L. Marivaux, A. Nel, C. Nemoz, X. Thibault, P. Vignaud, and S. Zabler, "Applications of X-ray synchrotron microtomography for non-destructive 3D studies of paleontological specimens," *Appl. Phys. A* **83**, 195–202 (2006).
8. D. Paganin, S. C. S. Mayo, T. E. Gureyev, P. R. Miller, and S. W. Wilkins, "Simultaneous phase and amplitude extraction from a single defocused image of a homogeneous object," *J. Microsc.* **206**, 33–40 (2002).

9. A. Kostenko, K. J. Batenburg, A. King, S. E. Offerman, and L. J. van Vliet, "Total variation minimization approach in in-line X-ray phase-contrast tomography," *Opt. Express* **21**, 12185–12196 (2013).
10. A. Kostenko, K. J. Batenburg, H. Suhonen, S. E. Offerman, and L. J. van Vliet, "Phase retrieval in in-line X-ray phase contrast imaging based on total variation minimization," *Opt. Express* **21**, 710–723 (2013).
11. L. I. Rudin, S. Osher, and E. Fatemi, "Nonlinear total variation based noise removal algorithms," *Phys. D* **60**, 259–268 (1992).
12. T. M. Buzug, *Computed Tomography-From Photon Statistics to Modern Cone-Beam CT* (Springer, 2008).
13. A. Burvall and U. Lundström, "Phase retrieval in X-ray phase-contrast imaging suitable for tomography," *Opt. Express* **19**, 10359–10376 (2011).
14. J. R. Fienup, "Phase retrieval algorithms: a comparison," *Appl. Opt.* **21**, 2758–2769 (1982).
15. A. Kostenko, "Phase-contrast X-ray tomography for soft and hard condensed matter," Ph.D. thesis (Technical University of Delft, 2013).
16. S. Kaczmarz, "Angenäherte Auflösung von Systemen linearer Gleichungen," *Bull. Int. Acad. Pol. Sci. Lett.* **35**, 355–357 (1937).
17. A. V. Bronnikov, "Theory of quantitative phase-contrast computed tomography," *J. Opt. Soc. Am. A* **19**, 472–480 (2002).
18. J. Bian, J. H. Siewerdsen, X. Han, E. Y. Sidky, J. L. Prince, C. A. Pelizzari, and X. Pan, "Evaluation of sparse-view reconstruction from flat-panel-detector cone-beam CT," *Phys. Med. Biol.* **55**, 6575–6599 (2010).
19. J. S. Jørgensen, "Sparse image reconstruction in computed tomography," Ph.D. thesis (Technical University of Denmark, 2013).
20. T. Pock and A. Chambolle, "Diagonal preconditioning for first order primal-dual algorithms in convex optimization," in *International Conference on Computer Vision (ICCV)* (2011), pp. 1762–1769.
21. A. Chambolle and T. Pock, "A first-order primal-dual algorithm for convex problems with applications to imaging," *J. Math. Imaging Vis.* **40**, 120–145 (2011).
22. E. Y. Sidky, J. H. Jørgensen, and X. Pan, "Convex optimization problem prototyping for image reconstruction in computed tomography with the Chambolle-Pock algorithm," *Phys. Med. Biol.* **57**, 3065–3091 (2012).
23. T. Goldstein, E. Esser, and R. Baraniuk, "Adaptive primal-dual hybrid gradient methods for saddle-point problems," *arXiv1305.0546* (2013).
24. R. D. Kongskov, "Phase-contrast simulator," 2015, <https://github.com/RasmusDalgas/Phase-Contrast-Simulator>.
25. P. C. Hansen and M. Saxild-Hansen, "AIR tools-A MATLAB package of algebraic iterative reconstruction methods," *J. Comput. Appl. Math.* **236**, 2167–2178 (2012).
26. J. S. Jørgensen, "Projector Pack, version 0.2," 2015, <http://github.com/jakobsj/Projector-Pack/releases/tag/v0.2>.
27. S. Kuznetsov, "X-ray optics calculator," IMT RAS, 2014, http://purple.ipmt-hpm.ac.ru/xcalc/xcalc_mysql/refractive.php.
28. P. C. Hansen, *Discrete Inverse Problems: Insight and Algorithms* (SIAM, 2010).
29. N. Otsu, "A threshold selection method from gray-level histograms," *IEEE Trans. Syst. Man. Cybern.* **20**, 62–66 (1979).

APPENDIX B

Directional Total Generalized Variation Regularization

Submitted to Journal of Scientific Computing
Available on <https://arxiv.org/pdf/1701.02675.pdf>

R. D. Kongskov, Y. Dong and K. Knudsen

Directional Total Generalized Variation Regularization

Rasmus Dalgas Kongskov* Yiqiu Dong* Kim Knudsen*

August 22, 2017

Abstract

In inverse problems, prior information and a priori-based regularization techniques play important roles. In this paper, we focus on image restoration problems, especially on restoring images whose texture mainly follow one direction. In order to incorporate the directional information, we propose a new directional total generalized variation (DTGV) functional, which is based on total generalized variation (TGV) by Bredies *et al.* [SIAM J. Imaging Sci., 3 (2010)]. After studying the mathematical properties of DTGV, we utilize it as regularizer and propose the L^2 -DTGV variational model for solving image restoration problems. Due to the requirement of the directional information in DTGV, we give a direction estimation algorithm, and then apply a primal-dual algorithm to solve the minimization problem. Experimental results show the effectiveness of the proposed method for restoring the directional images. In comparison with isotropic regularizers like total variation and TGV, the improvement of texture preservation and noise removal is significant.

1 Introduction

In the field of inverse problems, regularization techniques have been introduced to overcome the ill-posedness in order to obtain reasonable and stable solutions. For many image processing problems incorporating prior information through regularization techniques has attracted much attention. In this paper, we will study directional regularization for image restoration problems.

The image is given in the domain Ω , a connected bounded open subset of \mathbb{R}^2 with Lipschitz boundary, and given by a real-valued function $\hat{u} : \Omega \rightarrow \mathbb{R}$. The image is degraded through an operator $A \in \mathcal{L}(L^2(\Omega))$ and by additive white Gaussian noise η , and thus the degraded image f is given by

$$f = A\hat{u} + \eta. \quad (1)$$

We consider A as the identity operator (denoising problem) and A having the form of a blurring operator (deblurring problem). The analysis is based on the variational model for image restoration

$$\min_u \frac{1}{2} \|Au - f\|_{L^2(\Omega)}^2 + \lambda \mathcal{R}(u), \quad (2)$$

*Department of Applied Mathematics and Computer Science, Technical University of Denmark, 2800 Kgs. Lyngby, Denmark (rara@dtu.dk, yido@dtu.dk, kiknu@dtu.dk).



Figure 1: Left: A CT scan of uni-directional glass fibre (obtained from [26], see more in [25]). Right: A CT scan and 3D-model of an optical fibre with a cavity (obtained from [34]).

where \mathcal{R} is the regularization term, which incorporates prior information on \hat{u} , and $\lambda > 0$ is the regularization parameter, which controls the trade-off between the fit with the data f and the regularization.

Due to its capability of preserving sharp edges, total variation (TV) regularization proposed in [33] has been used for many image processing problems, e.g. in image denoising [42, 14, 15, 36], in blind deconvolution [12], in tomographic reconstruction [13, 27], etc. Although TV regularization is very effective for restoring piece-wise constant images, it has some shortcomings, and the most notable one is the appearance of staircasing artifacts in slanted regions [30, 32]. To overcome staircasing artifacts, higher-order derivatives have been used, see [35, 11, 37, 39]. In [8], total generalized variation (TGV) of order h , was proposed, which incorporates the first up to the h -th derivatives. When h equals 1, it yields the TV regularization.

In many applications related to fibers, the textures in images have very clear directionality. Examples include glass fibres in wind-turbine blades, optical fibres for communication, and ceramic fibres in fuel cells; see fig. 1. Another application with clear directional textures is seismic imaging. We call images with textures oriented mainly along one certain direction *directional images*. Achieving high-quality images is crucial for the analysis of these fibre materials, therefore imposing the directional information of the texture is highly desirable.

Directional regularization has been introduced for standard TV in [17, 5, 41, 19, 20] and in terms of shearlet-based TV in [16]. In [3] a type of directional TV is introduced for image denoising based on images with one main direction. This method is further developed to be spatially adaptive in [46] via pixel-specific angle-estimates. Moreover, the directional information through the structure tensor, defined in [43, 44], has been used to extend TV regularization. This new regularization method is called structure tensor total variation (STV), which has been applied in different imaging problems, see [28, 18]. The structure tensor has also been combined with second-order-derivative regularization in [23]. In [31, 21], anisotropic diffusion tensor has been applied only on the first-order-derivative term in the second-order TGV. All these directional regularization techniques are introduced for discretized problems, but the underlying continuous problems are not studied. Furthermore, it is in these previous work not clear if directional information can be incorporated in higher-order derivatives, e.g. through TGV regularizer.

The first goal of this paper is to formulate in a continuous setting regular-

ization terms that incorporate directionality. We first define the directional TV (DTV) functional and generalize it to higher orders, the so-called directional TGV (DTGV). We construct this generalization to higher orders such that the directional information is also incorporated in higher-order derivatives, which is different from the anisotropic TGV proposed in [31, 21]. Under the continuous setting we study the mathematical properties of the DTGV functional. Further, we utilize the DTGV functional as a regularizer in (2) and derive existence and uniqueness results for the minimization problem in (2). The second goal of the paper is to give a numerical implementation based on the primal-dual algorithm proposed in [10] to solve the minimization problem in (2), and through numerical experiments evaluate its performance. Since DTGV requires the input of the main direction we also propose a direction estimation algorithm.

The rest of the paper is organized as follows. In section 2 we define the directional total variation (DTV) functional. Through two equivalent definitions of DTV, we obtain a hint of how to incorporate directional information into TGV. In section 3, we propose the second order directional total generalized variation (DTGV_λ^2) functional, and extend it to higher orders. We study the mathematical properties of DTGV in section 4, and in section 5 we apply it as regularization in (2) to propose a new L^2 - DTGV_λ^2 model. The existence and uniqueness results for the L^2 - DTGV_λ^2 model is also provided. In section 6 we introduce a direction estimation algorithm in order to obtain the required main direction from the degraded images, and then apply a primal-dual algorithm for solving the minimization problem in our restoration model based on the work proposed in [10]. The numerical results shown in section 7 demonstrate the effectiveness of the direction estimation algorithm, the influence of the parameters in DTGV, and the performance of our restoration method. Finally, conclusions are drawn in section 8.

2 Directional Total Variation

The definition of total variation (TV) for $u \in \text{BV}(\Omega)$, the space of functions of bounded variation over the domain Ω , can be written as [2, 33]

$$\text{TV}(u) = \sup \left\{ \int_{\Omega} u \operatorname{div} \mathbf{v} \, dx \mid \mathbf{v} \in C_c^1(\Omega, \mathbb{R}^2), \mathbf{v}(x) \in B_2(0) \, \forall x \in \Omega \right\}, \quad (3)$$

where \mathbf{v} denotes the dual-variable and $B_2(0)$ denotes the closed Euclidean unit ball centered at the origin. In this section, we will introduce directional information into TV and define directional total variational (DTV). The idea of DTV was first proposed in [3] in the discrete case. Following a similar idea we will give the DTV definition in the continuous case. Through examples we demonstrate the differences between TV and DTV. More mathematical properties will be derived based on the extension to total generalized variation (TGV) in section 3.

TV is rotational invariant. In order to allow rotational variation, we restrict the dual variable \mathbf{v} in an ellipse instead of the unit ball. Define the closed elliptical set, $E^{a,\theta}(0)$, centered at the origin with the major semi-axis 1 oriented in direction

$(\cos \theta, \sin \theta)$ and the minor semi-axis $a \in (0, 1]$ by

$$E^{a,\theta}(0) = \left\{ \begin{pmatrix} x_1 \\ x_2 \end{pmatrix} \in \mathbb{R}^2 \left| \left(\frac{x_1 \cos \theta + x_2 \sin \theta}{1} \right)^2 + \left(\frac{-x_1 \sin \theta + x_2 \cos \theta}{a} \right)^2 \leq 1 \right. \right\}. \quad (4)$$

In fig. 2 the elliptical set $E^{a,\theta}(0)$ is depicted. We are now ready to define DTV:

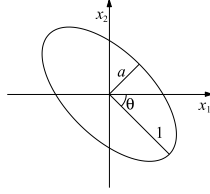


Figure 2: Sketch of the elliptical set $E^{a,\theta}(0)$. Here it is shown for $a = 0.5$ and $\theta = -\frac{\pi}{4}$.

Definition 2.1. The directional total variation (DTV) with respect to (a, θ) of a function $u \in \text{BV}(\Omega)$ is defined as

$$\text{DTV}(u) = \sup \left\{ \int_{\Omega} u \operatorname{div} \tilde{\mathbf{v}} \, dx \mid \tilde{\mathbf{v}} \in C_c^1(\Omega, \mathbb{R}^2), \tilde{\mathbf{v}}(x) \in E^{a,\theta}(0) \, \forall x \in \Omega \right\}.$$

Introduce the rotation matrix R_{θ} and the translation matrix Λ_a by

$$R_{\theta} = \begin{pmatrix} \cos \theta & -\sin \theta \\ \sin \theta & \cos \theta \end{pmatrix} \quad \text{and} \quad \Lambda_a = \begin{pmatrix} 1 & 0 \\ 0 & a \end{pmatrix}.$$

Then

$$\tilde{\mathbf{v}}(x) = R_{\theta} \Lambda_a \mathbf{v}(x) \in E^{a,\theta}(0) \quad \Leftrightarrow \quad \mathbf{v}(x) = \Lambda_{\frac{1}{a}} R_{-\theta} \tilde{\mathbf{v}}(x) \in B_2(0). \quad (5)$$

Further, we define the directional divergence for $\mathbf{v}(x) \in B_2(0)$

$$\widetilde{\operatorname{div}} \mathbf{v}(x) = \operatorname{div} R_{\theta} \Lambda_a \mathbf{v}(x) = \operatorname{div} \tilde{\mathbf{v}}(x). \quad (6)$$

Using the relations in (5) and the definition in (6) we give another equivalent definition for DTV.

Definition 2.2. For a function $u \in \text{BV}(\Omega)$, its DTV is defined as

$$\text{DTV}(u) = \sup \left\{ \int_{\Omega} u \widetilde{\operatorname{div}} \mathbf{v} \, dx \mid \mathbf{v} \in C_c^1(\Omega, \mathbb{R}^2), \mathbf{v}(x) \in B_2(0) \, \forall x \in \Omega \right\}.$$

This definition is very similar to the one for TV in (3); the only difference is the change on the divergence operator in the integral. Here we provide three examples on comparisons of DTV with TV:

Example 2.3. For $u \in C_c^\infty(\Omega)$ we have using integration by parts

$$\begin{aligned} \text{TV}(u) &= \|\nabla u\|_{L^1(\Omega)}, \\ \text{DTV}(u) &= \left\| \begin{pmatrix} D_\theta u \\ a D_{\theta^\perp} u \end{pmatrix} \right\|_{L^1(\Omega)} \end{aligned}$$

where $D_\theta u$ denotes the directional derivative of u in the direction $(\cos \theta, \sin \theta)$ and $\theta^\perp = \theta + \pi/2$.

The above example shows that $\text{DTV}(u)$ is an anisotropic total variation functional. The next example demonstrates the difference between DTV and TV .

Example 2.4. Define $u_1 = \chi_{B_2(0)}$, the characteristic function of the unit disk. The total variation of such a characteristic function is given by the length of the perimeter, i.e. $\text{TV}(u_1) = 2\pi$. The calculation of $\text{DTV}(u_1)$ is according to definition 2.2: by using the divergence theorem with \mathbf{n} denoting the outward unit normal vector we have for any $\mathbf{v} \in C_c^1(\Omega, \mathbb{R}^2)$

$$\begin{aligned} \int_\Omega u_1 \widetilde{\text{div}} \mathbf{v} \, dx &= \int_{B_2(0)} \text{div} R_\theta \Lambda_a \mathbf{v} \, dx \\ &= \int_{\partial B_2(0)} (R_\theta \Lambda_a \mathbf{v}) \cdot \mathbf{n} \, ds \\ &= \int_{\partial B_2(0)} \mathbf{v} \cdot (\Lambda_a R_{-\theta} \mathbf{n}) \, ds. \end{aligned}$$

The integrand is maximized among unit vector fields for $\mathbf{v} = (\Lambda_a R_{-\theta} \mathbf{n}) / |\Lambda_a R_{-\theta} \mathbf{n}|$ thus yielding

$$\begin{aligned} \text{DTV}(u_1) &= \int_{\partial B_2(0)} |\Lambda_a R_{-\theta} \mathbf{n}| \, ds \\ &= \int_0^{2\pi} (\cos^2(\tau - \theta) + a^2 \sin^2(\tau - \theta))^{1/2} d\tau \\ &= \int_0^{2\pi} (\cos^2 \omega + a^2 \sin^2 \omega)^{1/2} d\omega, \end{aligned} \tag{7}$$

which is by the way the length of the perimeter of the elliptical set $E^{a,\theta}(0)$.

Example 2.5. Take now instead the characteristic function $u_2 = \chi_{pE^{b,0}(0)}$ of the elliptical set $pE^{b,0}(0)$ with $0 < b < 1$. By choosing p such that

$$p \int_0^{2\pi} (b^2 \cos^2 \tau + \sin^2 \tau)^{1/2} d\tau = 2\pi$$

the length of the ellipse perimeter is $\text{TV}(u_2) = 2\pi$ as before.

Let us compute $\text{DTV}(u_2)$ for the two different orientations given by $\theta = 0$ and $\theta = \pi/2$. First fix $\theta = 0$ and $0 < a < 1$. The outward unit normal to $pE^{b,0}(0)$ at point $(p \cos \tau, pb \sin \tau)$ is

$$n(\tau) = \frac{1}{(b^2 \cos^2 \tau + \sin^2 \tau)^{1/2}} \begin{pmatrix} b \cos \tau \\ \sin \tau \end{pmatrix} \tag{8}$$

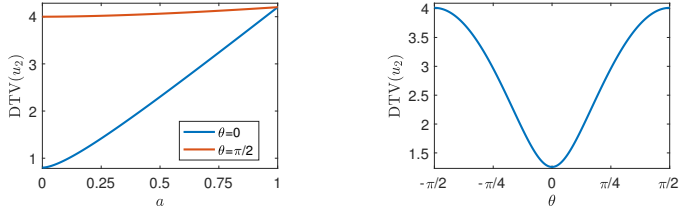


Figure 3: For u_2 with $b = 0.2$. Left: $\text{DTV}(u_2)$ as a function of a and three choices of θ . Right: $\text{DTV}(u_2)$ as a function of θ and $a = 0.5$.

and then with $\theta = 0$ calculate

$$\begin{aligned} \int_{\partial_p E^{b,0}(0)} (R_\theta \Lambda_a \mathbf{v}) \cdot \mathbf{n} \, ds &= \int_0^{2\pi} (\mathbf{v} \cdot \Lambda_a R_{-\theta} \mathbf{n}) |x'(\tau)| \, d\tau \\ &= p \int_0^{2\pi} \left(\mathbf{v} \cdot \begin{pmatrix} b \cos \tau \\ a \sin \tau \end{pmatrix} \right) d\tau. \end{aligned} \quad (9)$$

The integrand is maximized with the unit vector field

$$\mathbf{v}(\tau) = \frac{1}{(b^2 \cos^2 \tau + a^2 \sin^2 \tau)^{1/2}} \begin{pmatrix} b \cos \tau \\ a \sin \tau \end{pmatrix}$$

and thus we obtain

$$d_0 = \text{DTV}(u_2) = p \int_0^{2\pi} (b^2 \cos^2 \tau + a^2 \sin^2 \tau)^{1/2} d\tau \quad (10)$$

By using Maple to estimate the integration numerically, we compare (7) and (10), and find that while $\text{TV}(u_1) = \text{TV}(u_2)$, $\text{DTV}(u_2) < \text{DTV}(u_1)$.

Next, we compute $\text{DTV}(u_2)$ with $\theta = \frac{\pi}{2}$ and $0 < a \leq 1$. In this case, according to (9) by using (8) we get

$$\int_{\partial_p E^{b,0}(0)} (R_\theta \Lambda_a \mathbf{v}) \cdot \mathbf{n} \, ds = p \int_0^{2\pi} \left(\mathbf{v} \cdot \begin{pmatrix} -\sin \tau \\ ab \cos \tau \end{pmatrix} \right) d\tau.$$

Its maximum is reached at

$$\mathbf{v}(\tau) = \frac{1}{(\sin^2 \tau + a^2 b^2 \cos^2 \tau)^{1/2}} \begin{pmatrix} -\sin \tau \\ ab \cos \tau \end{pmatrix}$$

and we obtain

$$d_{\pi/2} = \text{DTV}(u_2) = p \int_0^{2\pi} (\sin^2 \tau + a^2 b^2 \cos^2 \tau)^{1/2} d\tau \quad (11)$$

By using Maple to estimate the integration numerically, we compare (10) and (11), and find $d_0 \leq d_{\pi/2}$.

In example 2.5 we illustrate the dependency of DTV on θ and a . The left plot shows that for fixed θ , $\text{DTV}(u_2)$ is monotonically increasing with a . Moreover, independent of the value of a , a smaller and more correct choice of θ , i.e. closer

to the main direction of the object, gives a lower $\text{DTV}(u_2)$. However, for $a = 1$ the values of $\text{DTV}(u_2)$ agree, since in that case DTV is equivalent to the rotationally invariant TV . The right plot suggests that $\text{DTV}(u_2)$ depends as a scaled and translated sine function with a minimum obtained when the rotation angle θ in DTV coincides with the main direction of the object (i.e. $\theta = 0$).

As a side remark we note that the extension of TV to DTV is based on knowledge (or estimates of) one global direction. Extensions of the presented work to the important case of spatially dependent directions is left for future work.

In imaging problems a common artifact caused by TV regularization is staircasing, which is a classical example of a mismatch between prior knowledge and the reality, i.e., smooth regions are approximated by piece-wise constant regions. One way to overcome the staircasing effect is to use higher order derivatives in the regularization; this is the topic of the next section.

3 Directional Total Generalized Variation

Total Generalized Variation (TGV) is a generalization of TV to a functional, which takes derivatives of order $h > 0$ into account, and the first order TGV , i.e., $h = 1$, is identical to TV . It turns out that for natural images, TGV regularization for denoising is often superior to TV regularization, and the staircasing effect is well avoided [8].

For a 2-by-2 symmetric matrix-valued function

$$V(x) = \begin{pmatrix} v_{11}(x) & v_{12}(x) \\ v_{12}(x) & v_{22}(x) \end{pmatrix} \in \text{Sym}^2(\mathbb{R}^2)$$

define

$$(\text{div } V)^\top = \begin{pmatrix} \frac{\partial v_{11}}{\partial x_1} + \frac{\partial v_{12}}{\partial x_2} \\ \frac{\partial v_{12}}{\partial x_1} + \frac{\partial v_{22}}{\partial x_2} \end{pmatrix}, \quad \text{div}^2 V = \frac{\partial^2 v_{11}}{\partial x_1^2} + \frac{\partial^2 v_{22}}{\partial x_2^2} + 2 \frac{\partial^2 v_{12}}{\partial x_1 \partial x_2}.$$

Define further the second order unit sphere $B_{2 \times 2}(0)$ consisting of matrices $V = (v_{i,j})_{i,j=1}^2$ with rows $(v_{i1}, v_{i2})^\top \in B_2(0)$ and columns $(v_{1i}, v_{2i})^\top \in B_2(0)$ for $i = 1, 2$. We write $W \in \lambda_0 B_{2 \times 2}(0)$ if $W/\lambda_0 \in B_{2 \times 2}(0)$ with $\lambda_0 > 0$, leaving $\|W\|_2 \leq \lambda_0$. Then we can for a function $u \in L^1(\Omega)$ define the second order TGV for $\lambda = (\lambda_0, \lambda_1)$ by

$$\text{TGV}_\lambda^2(u) = \sup \left\{ \int_\Omega u \text{div}^2 W \, dx \mid W \in C_c^2(\Omega, \text{Sym}^2(\mathbb{R}^2)), W(x) \in \lambda_0 B_{2 \times 2}(0), (\text{div } W(x))^\top \in \lambda_1 B_2(0) \forall x \in \Omega \right\}. \quad (12)$$

(Note that in [8] higher order TGV is defined equivalently using the Frobenius norm.)

In order to include directional information in TGV_λ^2 we replace higher order balls by higher order elliptical sets. Denote by $E_{2 \times 2}^{a,\theta}(0)$ the space of matrices $V = (v_{i,j})_{i,j=1}^2$ with rows $(v_{i1}, v_{i2})^\top \in E^{a,\theta}(0)$ and columns $(v_{1i}, v_{2i})^\top \in E^{a,\theta}(0)$ ($i = 1, 2$). Then we can define the second order directional TGV (DTGV):

Definition 3.1. The second order directional total generalized variation, DTGV_λ^2 , of a function $u \in L^1(\Omega)$ is defined as

$$\text{DTGV}_\lambda^2(u) = \sup \left\{ \int_\Omega u \operatorname{div}^2 \widetilde{W} \, dx \right\} \quad (13)$$

$$\widetilde{W} \in C_c^2(\Omega, \operatorname{Sym}^2(\mathbb{R}^2)), \widetilde{W}(x) \in \lambda_0 E_{2 \times 2}^{a, \theta}(0), (\operatorname{div} \widetilde{W}(x))^\top \in \lambda_1 E_2^{a, \theta}(0) \, \forall x \in \Omega \Big\}.$$

Remark 3.2. In [24], TGV has been extended to the infimal convolution of a number of TGV type functionals with arbitrary norms. Our definition of DTGV_λ^2 in (13) can be considered as a special case under this general definition with norm defined by particular ellipses.

Next, we will provide a characterization of DTGV_λ^2 , which has the same feasible set as in (12). To do so we need the second order generalization of (5)

$$\widetilde{V}(x) = R_\theta \Lambda_a V(x) \Lambda_a R_{-\theta} \in E_{2 \times 2}^{a, \theta}(0) \quad \Leftrightarrow \quad V(x) \in B_{2 \times 2}(0), \quad (14)$$

which follows easily from the definitions. In addition, we define for $W \in C_c^2(\Omega, \operatorname{Sym}^2(\mathbb{R}^2))$ the directional divergence

$$\widetilde{\operatorname{div}} W(x) = \operatorname{div} R_\theta \Lambda_a W(x) \quad (15)$$

and the second order directional divergence

$$\widetilde{\operatorname{div}}^2 W(x) = \operatorname{div}^2 \widetilde{W}(x) \quad \text{with} \quad \widetilde{W}(x) = R_\theta \Lambda_a W(x) \Lambda_a R_{-\theta}. \quad (16)$$

The characterization of DTGV_λ^2 is now as follows:

Theorem 3.3. *With the directional divergence and the second order directional divergence defined in (15) and (16), for $u \in L^1(\Omega)$*

$$\text{DTGV}_\lambda^2(u) = \sup \left\{ \int_\Omega u \widetilde{\operatorname{div}}^2 W \, dx \right\} \quad (17)$$

$$W \in C_c^2(\Omega, \operatorname{Sym}^2(\mathbb{R}^2)), \|W(x)\|_2 \leq \lambda_0, \|(\widetilde{\operatorname{div}} W(x))^\top\|_2 \leq \lambda_1 \, \forall x \in \Omega \Big\}.$$

Proof: Let $\widetilde{W} \in C_c^2(\Omega, \operatorname{Sym}^2(\mathbb{R}^2))$ with $\widetilde{W}(x) \in \lambda_0 E_{2 \times 2}^{a, \theta}(0)$ and $(\operatorname{div} \widetilde{W}(x))^\top \in \lambda_1 E_2^{a, \theta}(0)$ for any $x \in \Omega$. Due to (14) we have for any $x \in \Omega$

$$W(x) = \Lambda_{\frac{1}{a}} R_{-\theta} \widetilde{W}(x) R_\theta \Lambda_{\frac{1}{a}} \in \lambda_0 B_{2 \times 2}(0),$$

and hence $\|W(x)\|_2 \leq \lambda_0$. In addition, since $(\operatorname{div} \widetilde{W}(x))^\top \in \lambda_1 E_2^{a, \theta}(0)$, we obtain according to (5) that

$$\Lambda_{\frac{1}{a}} R_{-\theta} (\operatorname{div} \widetilde{W}(x))^\top = \Lambda_{\frac{1}{a}} R_{-\theta} (\operatorname{div} R_\theta \Lambda_a W(x) \Lambda_a R_{-\theta})^\top = (\widetilde{\operatorname{div}} W(x))^\top \in \lambda_1 B_2(0),$$

i.e. $\|(\widetilde{\operatorname{div}} W(x))^\top\|_2 \leq \lambda_1$. Hence, we have proven that the feasible set in (17) is equivalent to the one in (13), and the result follows from (16). \square

To close the section we extend the definition of DTGV_λ^2 to arbitrary order $h \in \mathbb{N}$. Recall from [8] the higher order TGV defined for any $h \in \mathbb{N}$, $\lambda = (\lambda_0, \lambda_1, \dots, \lambda_{h-1})$ by

$$\text{TGV}_\lambda^h(u) = \sup \left\{ \int_\Omega u \operatorname{div}^h \mathbf{w} \, dx \mid \mathbf{w} \in C_c^h(\Omega, \operatorname{Sym}^h(\mathbb{R}^2)), \|\operatorname{div}^l \mathbf{w}(x)\|_2 \leq \lambda_l, \forall x \in \Omega \text{ and } l = 0, \dots, h-1 \right\}, \quad (18)$$

where $\operatorname{Sym}^h(\mathbb{R}^2)$ denotes the space of symmetric h -tensors in \mathbb{R}^2 . For any $x \in \Omega$, $\mathbf{w}(x)$ is a symmetric h -tensor. The operator div^l on $\mathbf{w}(x)$ is defined as

$$(\operatorname{div}^l \mathbf{w}(x))_b = \sum_{\gamma \in N_l} \frac{l!}{\gamma!} \frac{\partial^l \mathbf{w}(x)_{b+\gamma}}{\partial x^\gamma} \quad \text{for each component } b \in N_{h-l}$$

where $N_h = \left\{ b \in \mathbb{N}^2 \mid |b| = \sum_{i=1}^2 b_i = h \right\}$. In addition, $\|\cdot\|_2$ on a symmetric h -tensor is defined as

$$\|\mathbf{w}(x)\|_2 = \left(\sum_{b \in N_h} \frac{h!}{b!} (\mathbf{w}(x))_b^2 \right)^{1/2}.$$

For further details of the h -tensors we refer the readers to [8].

To take the directional information into account, we first define two tensor fields:

$$\underbrace{B_{2 \times \dots \times 2}}_{m \text{ times}}(0) = \left\{ \xi \in \operatorname{Sym}^m(\mathbb{R}^2) : \xi(e_{p_1}, \dots, e_{p_{i-1}}, \cdot, e_{p_{i+1}}, \dots, e_{p_m}) \in B_2(0) \right. \\ \left. \text{for any } i \in \{1, \dots, m\} \text{ and } p \in \{1, 2\}^m \right\}, \quad (19)$$

$$\underbrace{E_{2 \times \dots \times 2}^{a, \theta}}_{m \text{ times}}(0) = \left\{ \xi \in \operatorname{Sym}^m(\mathbb{R}^2) : \xi(e_{p_1}, \dots, e_{p_{i-1}}, \cdot, e_{p_{i+1}}, \dots, e_{p_m}) \in E_2^{a, \theta}(0) \right. \\ \left. \text{for any } i \in \{1, \dots, m\} \text{ and } p \in \{1, 2\}^m \right\}, \quad (20)$$

where e_1 and e_2 denote the two standard basis vectors in \mathbb{R}^2 . Similar as in (6) and (16) we define l -directional divergence, $\widetilde{\operatorname{div}}^l$ for any order $l \leq h$ as

$$\widetilde{\operatorname{div}}^l \mathbf{w}(x) = \operatorname{div}^l \tilde{\mathbf{w}}(x),$$

where $\mathbf{w}(x) \in \underbrace{B_{2 \times \dots \times 2}}_{h \text{ times}}(0)$, and we can obtain $\tilde{\mathbf{w}}(x) \in \underbrace{E_{2 \times \dots \times 2}^{a, \theta}}_{l \text{ times}}(0) \otimes \underbrace{B_{2 \times \dots \times 2}}_{h-l \text{ times}}(0)$ referring to the relations in (5) with \otimes as the tensor product. Then as in (13), we give the definition of DTGV_λ^h as follows:

Definition 3.4. The h 'th-order directional total generalized variation, DTGV_λ^h , of a function $u \in L^1(\Omega)$ is defined as

$$\text{DTGV}_\lambda^h(u) = \sup \left\{ \int_\Omega u \operatorname{div}^h \mathbf{w} \, dx \mid \mathbf{w} \in C_c^h(\Omega, \operatorname{Sym}^h(\mathbb{R}^2)), \operatorname{div}^l \mathbf{w}(x) \in \lambda_l \underbrace{E_{2 \times \dots \times 2}^{a, \theta}}_{h-l \text{ times}}(0), \forall x \in \Omega \text{ and } l = 0, \dots, h-1 \right\}. \quad (21)$$

Following the similar idea as the proof of theorem 3.3, we obtain a characterization of DTGV_λ^h .

Theorem 3.5. For $u \in L^1(\Omega)$

$$\text{DTGV}_\lambda^h(u) = \sup \left\{ \int_\Omega u \widetilde{\text{div}}^h \mathbf{w} \, dx \mid \mathbf{w} \in C_c^h(\Omega, \text{Sym}^h(\mathbb{R}^2)), \|\widetilde{\text{div}}^l \mathbf{w}(x)\|_2 \leq \lambda_l, \forall x \in \Omega \text{ and } l = 0, \dots, h-1 \right\}. \quad (22)$$

Clearly $\text{DTGV}_1^1(u) = \text{DTV}(u)$.

4 Properties of DTGV

In this section, we will derive some properties of DTGV_λ^h on the space of *Bounded Generalized Variation* of order h (BGV^h), which is defined as

$$\text{BGV}^h(\Omega) = \left\{ u \in L^1(\Omega) \mid \text{TGV}_\lambda^h(u) < \infty \right\}.$$

When $\text{BGV}^h(\Omega)$ is equipped with the norm

$$\|u\|_{\text{BGV}^h(\Omega)} = \|u\|_{L^1(\Omega)} + \text{TGV}_\lambda^h(u),$$

it is a Banach space [8]. In the following two propositions we will show that by replacing TGV_λ^h with DTGV_λ^h we get an equivalent norm on $\text{BGV}^h(\Omega)$.

Proposition 1. $\text{DTGV}_\lambda^h : \text{BGV}^h(\Omega) \rightarrow \mathbb{R}$ is a semi-norm.

Proof: Based on the definition of DTGV_λ^h , it is obvious that $\text{DTGV}_\lambda^h(u) \geq 0$. Further, with the linearity of the integral we have

$$\text{DTGV}_\lambda^h(tu) = |t| \text{DTGV}_\lambda^h(u).$$

Define the feasible set of the supremum problem in (22) as:

$$K_D = \left\{ \mathbf{w} \in C_c^h(\Omega, \text{Sym}^h(\mathbb{R}^2)) \mid \|\widetilde{\text{div}}^l \mathbf{w}(x)\|_2 \leq \lambda_l, \forall x \in \Omega \text{ and } l = 0, \dots, h-1 \right\}.$$

Then, we have that for $u_1, u_2 \in \text{BGV}_\lambda^h$

$$\begin{aligned} \text{DTGV}_\lambda^h(u_1 + u_2) &= \sup_{\mathbf{w} \in K_D} \int_\Omega (u_1 + u_2) \widetilde{\text{div}}^h \mathbf{w} \, dx \\ &\leq \sup_{\mathbf{w} \in K_D} \int_\Omega u_1 \widetilde{\text{div}}^h \mathbf{w} \, dx + \sup_{\mathbf{w} \in K_D} \int_\Omega u_2 \widetilde{\text{div}}^h \mathbf{w} \, dx \\ &= \text{DTGV}_\lambda^h(u_1) + \text{DTGV}_\lambda^h(u_2). \end{aligned}$$

In addition, according to the definition of DTGV_λ^h we have $\text{DTGV}_\lambda^h(u) = 0$ for any constant function u . Therefore, we conclude that DTGV_λ^h is a semi-norm on $\text{BGV}^h(\Omega)$. \square

Proposition 2. For a function $u \in L^1(\Omega)$, we have

$$a^h \frac{\min_{l \in \{0, h-1\}} \lambda_l}{\max_{l \in \{0, h-1\}} \lambda_l} \text{TGV}_\lambda^h(u) \leq \text{DTGV}_\lambda^h(u) \leq \text{TGV}_\lambda^h(u). \quad (23)$$

Proof: Define the feasible sets of the supremum problems in the definitions of DTGV in (21) and TGV in (18) respectively as

$$K_E = \left\{ \mathbf{w} \in C_c^h(\Omega, \text{Sym}^h(\mathbb{R}^2)) \mid \text{div}^l \mathbf{w} \in \lambda_l \underbrace{E_{2 \times \dots \times 2}^{a, \theta}}_{h-l \text{ times}}(0), l = 0, \dots, h-1 \right\}.$$

$$K_B = \left\{ \mathbf{w} \in C_c^h(\Omega, \text{Sym}^h(\mathbb{R}^2)) \mid \text{div}^l \mathbf{w} \in \lambda_l \underbrace{B_{2 \times \dots \times 2}}_{h-l \text{ times}}(0), l = 0, \dots, h-1 \right\}.$$

Since $a \leq 1$ implies $E_{2 \times \dots \times 2}^{a, \theta}(0) \subseteq B_{2 \times \dots \times 2}(0)$ we see that $K_E \subset K_B$ and hence by the definitions that $\text{DTGV}_\lambda^h(u) \leq \text{TGV}_\lambda^h(u)$.

If we shrink the set K_B to

$$K_{\tilde{B}} = \left\{ \mathbf{w} \in C_c^h(\Omega, \text{Sym}^h(\mathbb{R}^2)) \mid \text{div}^l \mathbf{w} \in a^h \lambda_l \underbrace{B_{2 \times \dots \times 2}}_{h-l \text{ times}}(0), l = 0, \dots, h-1 \right\},$$

then we have $K_{\tilde{B}} \subset K_E$. Further, we obtain the inequality

$$\sup_{\mathbf{w} \in K_{\tilde{B}}} \int_{\Omega} u \text{div}^h \mathbf{w} \, dx \leq \sup_{\mathbf{w} \in K_E} \int_{\Omega} u \text{div}^h \mathbf{w} \, dx,$$

that is, $\text{TGV}_{a^h \lambda}^h(u) \leq \text{DTGV}_\lambda^h(u)$. Based on the third statement in proposition 3.3 in [8], we have the relation between TGV-functionals with different weights as:

$$c \text{TGV}_\lambda^h(u) \leq \text{TGV}_{a^h \lambda}^h(u) \quad \text{with} \quad c = a^h \frac{\min_{l \in \{0, h-1\}} \lambda_l}{\max_{l \in \{0, h-1\}} \lambda_l}.$$

Hence, $c \text{TGV}_\lambda^h(u) \leq \text{DTGV}_\lambda^h(u)$. \square

There are two straightforward consequences from proposition 2. First of all $\text{BGV}^h(\Omega)$ can equivalently be equipped with the norm

$$\|u\|_{\text{BGV}_\lambda^h(\Omega)} = \|u\|_{L^1(\Omega)} + \text{DTGV}_\lambda^h(u).$$

Second, the kernel of DTGV_λ^h can be characterized:

Corollary 1. $\text{DTGV}_\lambda^h(u) = 0$ if and only if u is a polynomial of degree less than h .

Proof: The kernel of $\text{TGV}_\lambda^h = 0$ consists of polynomials of degree less than h , see [8]; hence the conclusion follows from (23). \square

In the next proposition we will derive further properties of DTGV_λ^h .

Proposition 3. $\text{DTGV}_\lambda^h : \text{BGV}^h \rightarrow \mathbb{R}^+ \cup \{0\}$ is convex and lower semi-continuous.

Proof: For $u_1, u_2 \in L^1(\Omega)$ and $t \in [0, 1]$ we have

$$\begin{aligned} \text{DTGV}_\lambda^h(tu_1 + (1-t)u_2) &= \sup_{\mathbf{w} \in K_E} \int_{\Omega} (tu_1 + (1-t)u_2) \widetilde{\text{div}}^h \mathbf{w} \, dx \\ &\leq t \sup_{\mathbf{w} \in K_E} \int_{\Omega} u_1 \widetilde{\text{div}}^h \mathbf{w} \, dx + (1-t) \sup_{\mathbf{w} \in K_E} \int_{\Omega} u_2 \widetilde{\text{div}}^h \mathbf{w} \, dx \\ &= t \text{DTGV}_\lambda^h(u_1) + (1-t) \text{DTGV}_\lambda^h(u_2). \end{aligned}$$

Hence, DTGV_λ^h is convex.

By use of Fatou's lemma we can show the lower semi-continuity of DTGV_λ^h . Let $\{u_n\}_{n \in \mathbb{N}}$ be a Cauchy sequence in $\text{BGV}^h(\Omega)$ such that $u_n \rightarrow u$ in $L^1(\Omega)$. Based on the definition of DTGV_λ^h in (21) and Fatou's Lemma, for any $\mathbf{w} \in K_E$ we have

$$\liminf_{n \rightarrow \infty} \text{DTGV}_\lambda^h(u_n) \geq \liminf_{n \rightarrow \infty} \int_{\Omega} u_n \text{div}^h \mathbf{w} \, dx \geq \int_{\Omega} \liminf_{n \rightarrow \infty} u_n \text{div}^h \mathbf{w} \, dx = \int_{\Omega} u \text{div}^h \mathbf{w} \, dx.$$

Taking the supremum over all \mathbf{w} in K_E thus yields

$$\text{DTGV}_\lambda^h(u) \leq \liminf_{n \rightarrow \infty} \text{DTGV}_\lambda^h(u_n),$$

which means that DTGV_λ^h is indeed lower semi-continuous. \square

In the end of this section we give another similar equivalent definition as in Theorem 3.1 in [9] but for DTGV_λ^2 , which is highly attractive in the numerical implementation.

Theorem 4.1. *For $u \in L^1(\Omega)$ we have*

$$\text{DTGV}_\lambda^2(u) = \min_{v \in \text{BD}(\Omega)} \lambda_1 \|\tilde{D}u - v\|_{\mathcal{M}} + \lambda_0 \|\tilde{\mathcal{E}}v\|_{\mathcal{M}},$$

where $\text{BD}(\Omega)$ denotes the space of vector fields of Bounded Deformation [40], $\|\tilde{D}u\|_{\mathcal{M}} = \int_{\Omega} d|\tilde{D}u| = \text{DTV}(u)$, the directional symmetrized derivative $\tilde{\mathcal{E}}$ is the adjoint operator of $\widetilde{\text{div}}$ for a vector field.

Since the proof of theorem 4.1 is following the same lines as the proof of Theorem 3.1 in [9] except the change on the divergence operator, for more details we refer the readers to this paper. In addition, in section 6.1 we give definitions of all operators in the discrete case.

5 L^2 - DTGV_λ^2 Model

In this section we consider (2) with the regularization term given by DTGV_λ^2 , i.e.

$$\min_{u \in \text{BGV}^2(\Omega)} \mathcal{J}(u) \quad (24)$$

with

$$\mathcal{J}(u) = \frac{1}{2} \|Au - f\|_{L^2(\Omega)}^2 + \text{DTGV}_\lambda^2(u).$$

We call this the L^2 - DTGV_λ^2 model. Based on the properties of DTGV_λ^2 and $\text{BGV}^2(\Omega)$, we prove the existence and uniqueness of a solution to (24).

Theorem 5.1. *Suppose that f is in $L^2(\Omega)$ and $A \in \mathcal{L}(L^2(\Omega))$ is injective on the space of affine functions $\mathcal{A}^1(\Omega)$. Then the L^2 -DTGV $_{\lambda}^2$ model defined in (24) has a solution. Moreover, the solution is unique.*

Proof: Since \mathcal{J} is bounded from below, we can choose a minimizing sequence $\{u_n\}_{n \in \mathbb{N}} \subset \text{BGV}^2(\Omega)$ for (24). Thus both $\{\|Au_n - f\|_{L^2(\Omega)}\}$ and $\{\text{DTGV}_{\lambda}^2(u_n)\}$ with $n = 1, 2, \dots$ are bounded.

Let $P : L^2(\Omega) \rightarrow \mathcal{A}^1(\Omega)$ be a linear projection onto the space of affine functions on Ω , $\mathcal{A}^1(\Omega)$. Based on the result in proposition 4.1 in [9], we can find a constant $C > 0$ such that

$$\|u\|_{L^2(\Omega)} \leq C \text{TGV}_{\lambda}^2(u)$$

for any u in $\ker P \subset L^2(\Omega)$. Then from (23) we have

$$\|u\|_{L^2(\Omega)} \leq \tilde{C} \text{DTGV}_{\lambda}^2(u) \quad \forall u \in \ker P \subset L^2(\Omega),$$

with $\tilde{C} = \frac{C \max\{\lambda_0, \lambda_1\}}{a^2 \min\{\lambda_0, \lambda_1\}}$. By using corollary 1 and the triangle inequality on the semi-norm DTGV_{λ}^2 we obtain $\text{DTGV}_{\lambda}^2(u) = \text{DTGV}_{\lambda}^2(u - Pu)$. Hence, we have that $\{u_n - Hu_n\}_{n \in \mathbb{N}}$ is bounded in $L^2(\Omega)$.

Since A is injective on the finite-dimensional space $\mathcal{A}^1(\Omega)$, there is a $C_1 > 0$ such that $\|Pu\|_{L^2(\Omega)} \leq C_1 \|APu\|_{L^2(\Omega)}$. Further,

$$\begin{aligned} \|Pu_n\|_{L^2(\Omega)} &\leq C_1 \|APu_n\|_{L^2(\Omega)} \\ &\leq C_1 (\|Au_n - f\|_{L^2(\Omega)} + \|A(u_n - Pu_n) - f\|_2) \leq C_2, \end{aligned}$$

for some $C_2 > 0$. It implies that $\{u_n\}$ bounded in $L^2(\Omega)$.

Therefore, there exists a subsequence of $\{u_n\}$ that converges weakly to a $u^* \in L^2(\Omega)$. Based on the lower semi-continuity and convexity of DTGV_{λ}^2 stated in proposition 3 we obtain that u^* is a minimizer of \mathcal{J} and hence a solution of the model (24).

Based on proposition 3, the functional \mathcal{J} is convex. Furthermore, combining with the result in corollary 1 and A is injective on $\mathcal{A}^1(\Omega)$, (24) is strictly convex, thus its minimizer has to be unique [1]. \square

6 Algorithms

In this section we will introduce the algorithms needed for the following numerical simulations. First we will give the notations and discretization of the different operators that our algorithms will require. To keep the notation simple, we re-use the same symbols as in continuous case in the previous sections for the discrete case. Then, we will propose a method for estimating the main direction in images. In the end of the section, we will propose a primal-dual based algorithm for solving the minimization problem in the L^2 -DTGV $_{\lambda}^2$ model.

6.1 Notation and discretization

The domain Ω is discretized as an M -by- M equidistant pixel-grid with pixel-size 1×1 . We use (i, j) to denote a pixel index with $1 \leq i, j \leq M$, such that $u_{i,j}$ gives the pixel value at (i, j) . Here, for the sake of simplicity we stick to a square pixel-grid, but all proposed algorithms can be easily generalized to any rectangular discretization.

For $u \in \mathbb{R}^{M \times M}$, the discrete gradient operator $\nabla : \mathbb{R}^{M \times M} \rightarrow \mathbb{R}^{2M \times M}$ is defined as

$$\nabla u = \begin{pmatrix} \nabla_{x_1}^+ u \\ \nabla_{x_2}^+ u \end{pmatrix},$$

where $\nabla_{x_1}^+$ and $\nabla_{x_2}^+$ are obtained by applying a forward finite difference scheme with symmetric boundary condition, i.e.,

$$(\nabla_{x_1}^+ u)_{i,j} = \begin{cases} u_{i+1,j} - u_{i,j}, & \text{if } i < M, \\ 0, & \text{if } i = M, \end{cases} \quad \text{and} \quad (\nabla_{x_2}^+ u)_{i,j} = \begin{cases} u_{i,j+1} - u_{i,j}, & \text{if } j < M, \\ 0, & \text{if } j = M. \end{cases}$$

The divergence operator is defined as the adjoint operator of ∇ , i.e., we have $\text{div} = -\nabla^* = (\nabla_{x_1}^-, \nabla_{x_2}^-)$, where $\nabla_{x_1}^-$ and $\nabla_{x_2}^-$ utilize the backward finite difference scheme.

Moreover, based on the relation in (6), the directional divergence for a tensor \mathbf{v} with $\mathbf{v}_{i,j} = (v_{i,j}^1, v_{i,j}^2)^\top$ and $1 \leq i, j \leq M$ can be obtained by calculating

$$(\widetilde{\text{div}} \mathbf{v})_{i,j} = (\text{div } \widetilde{\mathbf{v}})_{i,j} \quad \text{with} \quad \widetilde{\mathbf{v}}_{i,j} = R_\theta \Lambda_a \mathbf{v}_{i,j}.$$

The corresponding directional gradient operator is $(\widetilde{\nabla} u)_{i,j} = \Lambda_a R_{-\theta} (\nabla u)_{i,j}$.

For a tensor W with $W_{i,j} = \begin{pmatrix} w_{i,j}^{11} & w_{i,j}^{12} \\ w_{i,j}^{12} & w_{i,j}^{22} \end{pmatrix}$ and $1 \leq i, j \leq M$, its divergence can be expressed as

$$(\text{div } W)_{i,j} = \begin{pmatrix} (\nabla_{x_1}^+ w^{11})_{i,j} + (\nabla_{x_2}^+ w^{12})_{i,j} \\ (\nabla_{x_1}^+ w^{12})_{i,j} + (\nabla_{x_2}^+ w^{22})_{i,j} \end{pmatrix}.$$

Based on the definition in (15), the directional divergence, $\widetilde{\text{div}}$, can be obtained by calculating

$$(\widetilde{\text{div}} W)_{i,j} = (\text{div } \widetilde{W})_{i,j} \quad \text{with} \quad \widetilde{W}_{i,j} = R_\theta \Lambda_a W_{i,j}.$$

In addition, the directional symmetrized derivative of the tensor \mathbf{v} defined above is given by

$$(\widetilde{\mathcal{E}} \mathbf{v})_{i,j} = \frac{1}{2} \left[\Lambda_a R_\theta \begin{pmatrix} (\nabla_{x_1}^- v^1)_{i,j} & (\nabla_{x_1}^- v^2)_{i,j} \\ (\nabla_{x_2}^- v^1)_{i,j} & (\nabla_{x_2}^- v^2)_{i,j} \end{pmatrix} + \begin{pmatrix} (\nabla_{x_1}^- v^1)_{i,j} & (\nabla_{x_2}^- v^1)_{i,j} \\ (\nabla_{x_1}^- v^2)_{i,j} & (\nabla_{x_2}^- v^2)_{i,j} \end{pmatrix} R_\theta^\top \Lambda_a \right]$$

Note that for tensors it still holds that $\widetilde{\text{div}} = -\widetilde{\mathcal{E}}^*$.

6.2 Detecting the main direction in images

In order to apply DTGV as regularization, the parameters a and θ have to be specified. In this paper, we focus on the case that the texture in images is mainly along one direction. By estimating this main direction, we will obtain the parameter θ . The parameter a somehow shows the confidence on the angle estimation. For image restoration, the main direction can be estimated directly from the degraded images. Some classical methods to estimate angles or directions in images could be used here, e.g., 2D Fourier transform and the arctangent function with two arguments. There are also more advanced techniques for angle estimation. Here we list a few of them: the quadrature filter [22], the boundary tensor [22],

and the structure tensor [45]. Most of these methods estimate the direction pixel-wisely, but in our case we aim for only one main direction for the whole image. In this section, based on our single direction assumption, we will introduce another method for estimating the main direction.

Our direction estimator is inspired by [38], and is mainly composed of three steps. First, we smooth the degraded image in order to reduce the influence of noise. Then, a pixel-wise angle estimation is calculated as

$$\Theta_{i,j} = \begin{cases} 0, & \text{if } |(\nabla f^\sigma)_{i,j}|_2 < 10^{-3}, \\ \arccos\left(\frac{(\nabla_{x_1}^+ f^\sigma)_{i,j}}{|(\nabla f^\sigma)_{i,j}|_2}\right), & (\nabla_{x_2}^+ f^\sigma)_{i,j} \geq 0 \text{ and } |(\nabla f^\sigma)_{i,j}|_2 < 10^{-3}, \\ 2\pi - \arccos\left(\frac{(\nabla_{x_1}^+ f^\sigma)_{i,j}}{|(\nabla f^\sigma)_{i,j}|_2}\right), & \text{otherwise,} \end{cases} \quad (25)$$

where f^σ denotes the smoothed image from the first step. After that, we smooth the estimated angles in order to remove outliers and features due to noise. At the same time, we introduce the new period for the angles. Note that in [38] the focus is on restoring rectangular shapes, therefore $\pi/2$ -period is used. But in our case, we need a π -period estimate. Moreover, we only need the main direction in the image, which is obtained by calculating the mean over the pixel-wise angles. In algorithm 1 the details of the main direction estimation method are outlined. It should be noted that if we do not calculate the mean of the angles, we will have pixel-wise angle estimates, which can be utilized for restoring images with multiple angles in the future. Since in this paper we mainly focus on the analysis of DTGV under continuous setting and its extension to spatially varying angles is not trivial, the applications on restoring images with multiple angles are outside the scope of this work.

Algorithm 1 Main Direction Estimation Method

- 1: Input smoothing parameter μ and the degraded image f .
 - 2: Smooth the degraded image by implementing Gaussian blur: $f^\sigma = G_\sigma f$, where G_σ denotes Gaussian blurring operator with mean 0 and variance σ^2 .
 - 3: Estimate pixel-wise direction Θ^u according to (25).
 - 4: Introduce $\frac{\pi}{2}$ -period to the angles and smooth them:
2mm $c_{i,j}^u = \cos(4\Theta_{i,j}^u)$,
5: $s_{i,j}^u = \sin(4\Theta_{i,j}^u)$,
 - 6: $(c^v, s^v) = \arg \min_{c^v, s^v} \sum_{i,j} |(\nabla f)_{i,j}|_2^2 \left| \begin{pmatrix} c_{i,j}^u \\ s_{i,j}^u \end{pmatrix} - \begin{pmatrix} c_{i,j}^v \\ s_{i,j}^v \end{pmatrix} \right|_2^2 + \mu \left(|(\nabla c^v)_{i,j}|_2^2 + |(\nabla s^v)_{i,j}|_2^2 \right)$.
 - 2mm The smoothed pixel-wise angles, Θ^v , are obtained by implementing (25) with $\begin{pmatrix} c^v \\ s^v \end{pmatrix}$ instead of ∇f^σ as input.
 - 7: Calculate the main direction: $\theta = \frac{1}{|\Omega|} \sum_{i,j} \Theta_{i,j}^v$.
 - 8: Transform into π -periodic angle according to
 - 9: $\theta \leftarrow \begin{cases} -\theta, & \text{if } (\nabla_{x_1}^+ f^\sigma) : (\nabla_{x_2}^+ f^\sigma) \leq 0, \\ \frac{\pi}{2} - \theta, & \text{otherwise,} \end{cases}$
 - 10: where “ \cdot ” denotes the Frobenius inner product. **return** θ .
-

6.3 The Chambolle-Pock algorithm

Corresponding to (24) we formulate the discrete L^2 -DTGV $_{\lambda}^2$ model as

$$\min_{u \in \mathbb{R}^{M \times M}} \mathcal{J}(u) := \frac{1}{2} \|Au - f\|_F^2 + \text{DTGV}_{\lambda}^2(u), \quad (26)$$

where $f \in \mathbb{R}^{M \times M}$ and $A : \mathbb{R}^{M \times M} \rightarrow \mathbb{R}^{M \times M}$ denotes the identity operator (denoising problem) or a blurring operator (deblurring problem). Since the minimization problem in (26) is convex, many optimization algorithms could be used to solve it, e.g. Nesterovs method [29], the FISTA algorithm [4], the alternating direction method with multipliers (ADMM) [6], and any of the many primal-dual-based methods. Here, due to the simplicity of the implementation, we utilize the Chambolle-Pock primal-dual (CP) algorithm [10] to solve our problem.

Referring to the algorithm proposed in [7], we can rewrite the data-fitting term in (26), $\mathcal{F}(u) = \frac{1}{2} \|Au - f\|_F^2$, as

$$\mathcal{F}(u) = \max_{q \in \mathcal{U}} \langle Au, q \rangle - \frac{1}{2} \|q\|_F^2 - \langle f, q \rangle, \quad (27)$$

where $\mathcal{U} = \mathbb{R}^{M \times M}$. Combining with the result in theorem 4.1, we obtain the primal-dual formulation of (26)

$$\min_{u \in \mathcal{U}, \mathbf{v} \in \mathcal{V}} \max_{q \in \mathcal{U}, \mathbf{p} \in \mathcal{P}, W \in \mathcal{W}} \langle Au, q \rangle - \frac{1}{2} \|q\|_F^2 - \langle f, q \rangle + \langle \tilde{\nabla} u - \mathbf{v}, \mathbf{p} \rangle + \langle \tilde{\mathcal{E}} \mathbf{v}, W \rangle$$

where $\mathcal{V} = \mathbb{R}^{2M \times M}$, $\mathcal{P} = \{\mathbf{p} : \Omega \rightarrow \mathbb{R}^2 \mid \|\mathbf{p}_{i,j}\|_2 \leq \lambda_1 \text{ for } \forall (i,j) \in \Omega\}$, $\mathcal{W} = \{W : \Omega \rightarrow \text{Sym}^2(\mathbb{R}^2) \mid \|W_{i,j}\|_F \leq \lambda_0 \text{ for } \forall (i,j) \in \Omega\}$. This is a generic saddle-point problem, and we can apply the CP algorithm proposed in [10] to solve it. The algorithm is summarized in Algorithm 2.

In algorithm 2, η and τ denote the dual and primal step-sizes, respectively. In addition, \mathcal{S}_{λ} is a set-projection operator defined as

$$[\mathcal{S}_{\lambda}(\xi)]_{i,j} = \frac{\xi_{i,j}}{\max\left(1, \frac{|\xi_{i,j}|}{\lambda}\right)}.$$

If $\xi \in \mathcal{P}$, then $|\xi_{i,j}|$ is with 2-norm; and if $\xi \in \mathcal{W}$, then $|\xi_{i,j}|$ is with Frobenius norm. Here, we use the relative changes of the objective function in (26) to define the stopping criterion, since the objective function is essentially what we desire to minimize and it is simple to calculate.

7 Numerical Experiments

In this section, we provide numerical experiments to study the behavior of our method. First, we examine the direction estimation method proposed in algorithm 1 for a series of noisy images, ranging from low- to high-level noise. Since the directional regularization requires additional parameters (θ, a) , we then empirically examine how these parameters influence the solution of (26). In the end, we compare DTGV $_{\lambda}^2$ - and DTV-regularization with TGV $_{\lambda}^2$ - and classical TV-regularization for some denoising and deblurring problems, where the blurring and noise have been simulated. Based on the balance between the computational complexity and restoration improvement, the second order of TGV is

Algorithm 2 The CP algorithm for solving L²-DTGV_λ²

- 1: Require f, A, λ, a, θ and tol.
- 2: Estimate Lipschitz constant L , e.g. using power-method for A .
- 3: Initialize $u^0 = \bar{u}^0 = 0, v^0 = 0, q^0 = 0, p^0 = \bar{p}^0 = 0, w^0 = 0, e^0 = 0, \eta < \frac{1}{\sqrt{L}}, \tau < \frac{1}{\sqrt{L}}$.
- 4: Run loop until stopping criterion is met:
- 5: **while** $e^k > \text{tol}$ **do**

$$\mathbf{p}^{k+1} = \arg \max_{\mathbf{p} \in \mathcal{P}} \langle \tilde{\nabla} \bar{u}^k - \bar{\mathbf{v}}^k, \mathbf{p} \rangle - \frac{1}{2\eta} \|\mathbf{p} - \mathbf{p}^k\|_F^2$$

$$= \mathcal{S}_{\lambda_1} \left(\mathbf{p}^k + \eta \left(\tilde{\nabla} \bar{u}^k - \bar{\mathbf{v}}^k \right) \right)$$

$$W^{k+1} = \arg \max_{W \in \mathcal{W}} \langle \tilde{\mathcal{E}} \bar{\mathbf{v}}^k, W \rangle - \frac{1}{2\eta} \|W - W^k\|_F^2$$

$$= \mathcal{S}_{\lambda_0} \left(W^k + \eta \tilde{\mathcal{E}} \bar{\mathbf{v}}^k \right)$$

$$q^{k+1} = \arg \max_{q \in \mathcal{U}} \langle A \bar{u}^k, q \rangle - \frac{1}{2} \|q\|_F^2 - \langle f, q \rangle - \frac{1}{2\eta} \|q - q^k\|_F^2$$

$$= \frac{1}{1 + \eta} \left(q^k + \eta (A \bar{u}^k - f) \right)$$

$$u^{k+1} = \arg \min_{u \in \mathcal{U}} \langle Au, q^{k+1} \rangle + \langle \tilde{\nabla} u, \mathbf{p}^{k+1} \rangle + \frac{1}{2\tau} \|u - u^k\|_F^2$$

$$= u^k + \tau \left(\widetilde{\text{div}} \mathbf{p}^{k+1} - A^* q^{k+1} \right)$$

$$\mathbf{v}^{k+1} = \arg \min_{\mathbf{v} \in \mathcal{V}} -\langle \mathbf{v}, \mathbf{p}^{k+1} \rangle + \langle \tilde{\mathcal{E}} \mathbf{v}, W^{k+1} \rangle + \frac{1}{2\tau} \|\mathbf{v} - \mathbf{v}^k\|_F^2$$

$$= \mathbf{v}^k + \tau \left(\mathbf{p}^{k+1} + \widetilde{\text{div}} W^{k+1} \right)$$

$$\bar{u}^{k+1} = 2u^{k+1} - u^k$$

$$\bar{\mathbf{v}}^{k+1} = 2\mathbf{v}^{k+1} - \mathbf{v}^k$$

$$e^{k+1} = \frac{|\mathcal{J}(u^k) - \mathcal{J}(u^{k+1})|}{\mathcal{J}(u^k)}$$

end while

- 6: **return** u^{k+1} .
-

mostly widely used, so in our numerical experiments we only investigate DTGV_λ^2 and compare it with TGV_λ^2 . To simplify the notations, we refer to TGV_λ^2 and DTGV_λ^2 as TGV and DTGV in this section. In addition, same as in [8] we fix the ratio between the two regularization parameters, i.e., $\frac{\lambda_0}{\lambda_1} = 2$, which commonly yields good restoration results for images. The tolerance in the algorithm 2 has been chosen as 10^{-6} and all simulated experiments are implemented in Matlab R2016a.

7.1 Robustness of direction-estimation

Since the estimation of the main direction plays an important role in our method, we first demonstrate the performance of the presented direction-estimation method in algorithm 1. Here, we use one simulated image and one real image for numerical experiments, and test our direction-estimation method on the images with up to 50% Gaussian noise. In all tests, we set $\sigma = 10$ for the smoothing step, i.e., Step 2 in algorithm 1. The numerical results are shown in fig. 4. It is clear that for both test images, until the noise level (nl) reaching to 20%, our method provides estimates within $\pm 15^\circ$ of the main direction. Especially for the real image, even with 50% noise, the estimation is still very accurate.

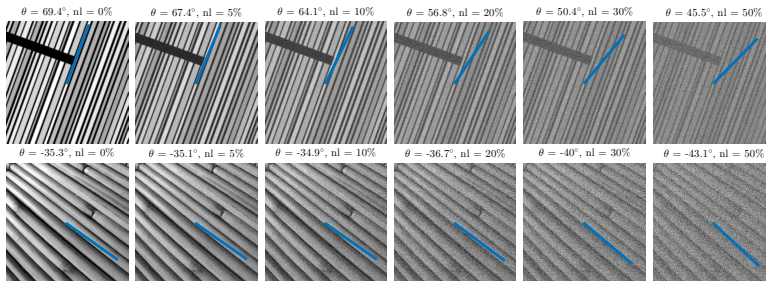


Figure 4: Estimating main direction in test images with increasing noise-level (nl). The top image size is 512×512 and bottom one is 253×253 . Main direction estimate θ is written in degrees and visualized on top of the noisy images with a blue line from the center.

7.2 Role of DTGV parameters

In the DTGV functional, besides the parameters $\lambda_{0,1}$ there are another two important parameters: θ and a , where θ is an angle and a determines the ratio of anisotropy. If $a = 1$, DTGV becomes identical to the rotation invariant TGV. In this section, we will test the influence of these two parameters when DTGV is used as a regularizer, and also seek the robustness of the L^2 - DTGV solutions with respect to the parameter choices.

In order to study the influence from a and θ solely, in each test with fixed values for (a, θ) we adjust the regularization parameter λ and pick the one that provides the highest peak signal-to-noise ratio (PSNR) value. The test images used for our numerical algorithm consist of two simulated images and two natural images as shown in fig. 5. Since the test image in fig. 6 is piece-wise constant,

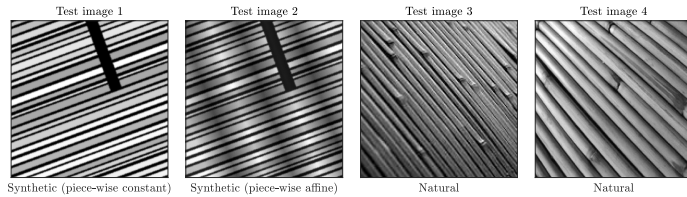


Figure 5: Ground truth images used in the numerical tests.

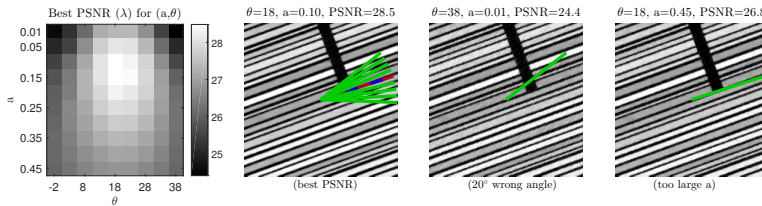


Figure 6: Test image 1: piece-wise constant image with size 256-by-256. DTV-regularized denoising problem. Lines mark specific angles: **tested angles**, **estimated angle** and **best angle**.

DTV is used as regularizer instead of DTGV. All test images are corrupted by 10% Gaussian noise, and the operator A is set as the identity. In fig. 6-9, we visualize the PSNR values for different choice of (a, θ) , where we test $a \in [0.01, 0.45]$ and $\theta \in [\bar{\theta} - 20^\circ, \bar{\theta} + 20^\circ]$ with $\bar{\theta}$ as the estimated main direction by algorithm 1. In addition, for each test image we also show three restoration results: the best one, according to PSNR, one with $\theta = \bar{\theta} + 20^\circ$ and small a , and one with $\theta = \bar{\theta}$ and large a .

Obviously, the use of directional regularization improves the PSNR values significantly when θ coincides with the main direction of the image. Moreover, with a good direction estimation the highest PSNR values are usually achieved by choosing a relatively small a . From the restored images we can see that with incorrect θ and a small a there are some line artifacts along the direction of θ . The reason is that with a small a the textures in the images are forced to be restored along the incorrect direction. With correct θ and a large a the restored results look very similar to the TV- or TGV-regularized results. Especially in the last figure of fig. 6, staircasing artifacts start to appear.

When DTGV is used as the regularizer to penalize the textures that are not oriented along the main direction of the images, we take θ as the main direction and choose a depending on how much to penalize the textures that are not along θ . Hence the selection of (θ, a) only depends on the orientation of the textures and not on the noise level. In order to empirically confirm the noise robustness, in fig. 10 we give an example similar to the one in fig. 9, but now with the image corrupted by 20% additive Gaussian noise. In this test, we still adjust the regularization parameter λ and pick the one that provides the highest PSNR value. Note that λ controls the trade-off between a good fit to the noisy image and the smoothness from DTGV, so it varies due to the different noise level. We

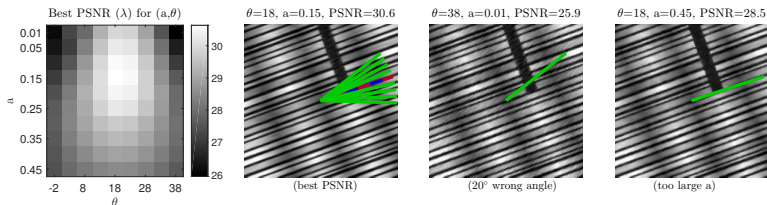


Figure 7: Test image 2: piece-wise affine image with size 256-by-256. DTGV-regularized denoising problem. Lines mark specific angles: **tested angles**, **estimated angle** and **best angle**.

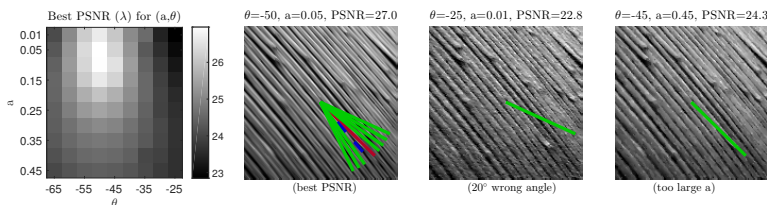


Figure 8: Test image 3: real image with size 145-by-145. DTGV-regularized denoising problem. Lines mark specific angles: **tested angles**, **estimated angle** and **best angle**.

can see that the PSNR figure with respect to (a, θ) in fig. 10 is very similar to the one in fig. 9 except the different range of the PSNR values, which demonstrates that the choice of (a, θ) is independent on the noise levels.

The tests in fig. 6-10 can also serve as robustness tests for our method. They show that our method is robust with respect to the parameters for $a \in [0.1, 0.2]$ and θ within $[\bar{\theta} - 5^\circ, \bar{\theta} + 5^\circ]$. So in the following numerical experiments, we will use algorithm 1 to estimate θ and fix a to 0.15.

7.3 Image denoising

To show the improvement of imposing the direction prior into the regularizer we empirically compare DTGV and DTV with TGV and TV for image denoising problems. We use four different test images with 10% and 20% Gaussian noise respectively. In all tests, after many experiments with different choices of the regularization parameter λ , the ones that give the best PSNRs are presented here.

Comparing the results from the four different regularization techniques in fig. 11 and fig. 12, we see that both visually and quantitatively in terms of PSNR the improvement by directional regularizers is evident. Especially the PSNR values of the results from solving the L^2 -DTGV model are at least 2.2dB higher than the ones from the L^2 -TGV results. The textures in the images are obviously much better preserved by using DTV and DTGV than by using the two isotropic regularizers, i.e., TV and TGV. Note that in both results from TV and DTV for the second test image, the staircasing artifact is observable along the main

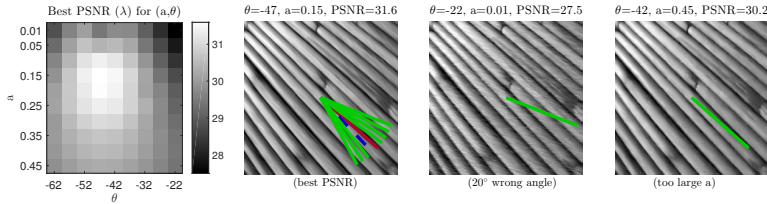


Figure 9: Test image 4: real image. DTGV-regularized denoising problem. Lines mark specific angles: **tested angles**, **estimated angle** and **best angle**.

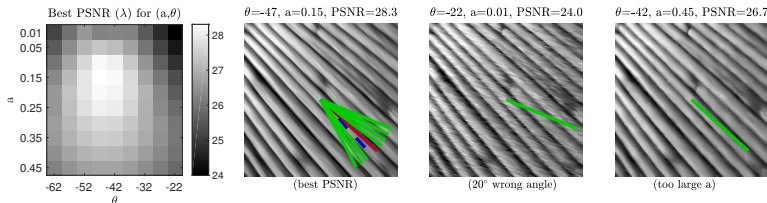


Figure 10: Test image 4: real image. DTGV-regularized denoising problem (with 20% Gaussian noise). Lines mark specific angles: **tested angles**, **estimated angle** and **best angle**.

direction. This is due to the test image being piece-wise affine, while the TV and DTV regularizers are based on an assumption of piece-wise constant images. In this case, by using DTGV as regularizer the artifacts are successfully removed and the textures are well preserved. Hence, these tests demonstrate the advantages of including directional information in the regularizer when dealing with directional images.

In the first two simulated test images, we specially add a dark region perpendicular to the main direction in order to demonstrate the potential artifacts from the directional regularizers. We can see that near the boundary of the dark region some artifacts in the restored results by DTV and DTGV appear. These artifacts are due to the diffusion of the different intensities along the main direction. In addition, the similar artifacts can be observed in the results from DTV and DTGV for restoring the two real images, especially for lines that are close to perpendicular to the main direction. In order to clearly show these artifacts, in fig. 13 we zoomed in on the center of the last test image and show the comparison of the four restorations. These artifacts mainly occur when the direction prior is not met, e.g. a part of the image textures do not follow the main direction.

In the DTGV_λ^2 regularizer, the directional information is introduced both in the first and second-order derivatives. To demonstrate the advantage of this we compare our method with the anisotropic TGV method, ITGV, proposed in [31, 21]. In ITGV, a diffusion tensor is estimated from the noisy image and used only in the first-order derivative term. Since in this paper we only consider the case of textures with one global direction, in order to have a fair comparison in fig. 14 we give the result from ITGV method with the same direction estimation as ours; we mark this result by the name DITGV. Since in ITGV the diffusion tensor

is highly influenced by noise, its performance is limited. Comparing the results from DITGV and DTGV, we can clearly see that the advantage of including the directional information also in the second-order derivative terms.

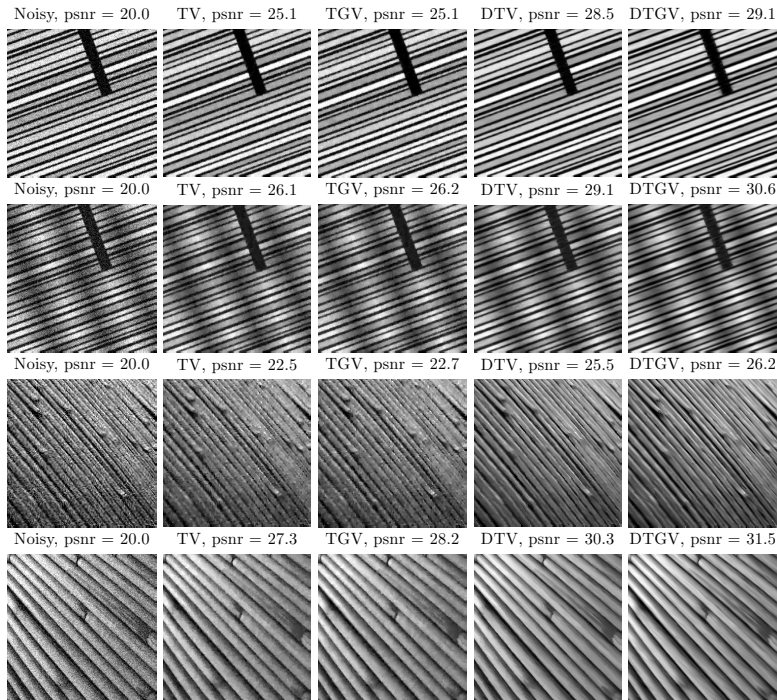


Figure 11: Comparison of TV, TGV, DTV and DTGV regularizers for four different denoising problems with 10% Gaussian noise.

7.4 Image deblurring and denoising

In order to test directional regularization on a more complicated problem, we consider the restoration of noisy blurred images. In our experiment, the blurring operator is set as Gaussian blur with a standard deviation of 2. Further, after being blurred, the test image is corrupted by 10% Gaussian noise. In our method, we still use algorithm 1 to estimate the main direction in the image.

In fig. 15, we show the degraded image and the restored results by using TV, TGV, DTV and DTGV regularizers. It is clear that both TV and TGV cannot help to restore the edges correctly, while the methods with the directional regularizers are much better at restoring the textures and removing the noise. In addition, the DTV result is heavily influenced by staircasing artifacts, since this test image is piece-wise affine which does not fit with the piece-wise constant assumption for the method. Due to the use of higher order derivatives, those artifacts do not appear in the DTGV result, as expected. Quantitatively, the

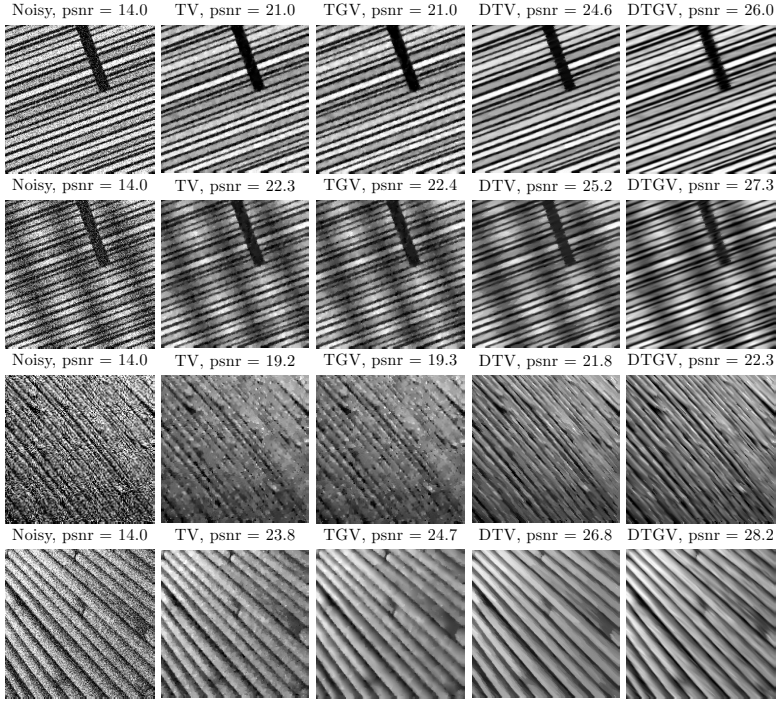


Figure 12: Comparison of TV, TGV, DTV and DTGV regularizers for four different denoising problems with 20% Gaussian noise.

PSNR value is increased by at least 2.5dB when the directional regularizer is utilized.

8 Conclusion

In this paper, we propose a new directional functional, directional total generalized variation (DTGV), and study its mathematical properties. Then we combine DTGV with the least-squares data-fitting term and propose a new variational model, L^2 -DTGV, for restoring images whose textures mainly follow one direction. We prove the existence and uniqueness of a solution to our proposed model, and apply a primal-dual algorithm to solve the minimization problem. Since the new proposed DTGV functional requires the input of the main direction of the images, we also propose a direction estimation algorithm, which can be easily extended to spatially varying direction estimation. Numerical results show that the direction estimation algorithm is reliable and the improvement for restoring directional images by using DTGV as regularizer is significant compared to using isotropic regularizers. In addition, we also try to discover the potential artifacts from DTGV. In order to reduce the artifacts from DTGV, we intend to extend

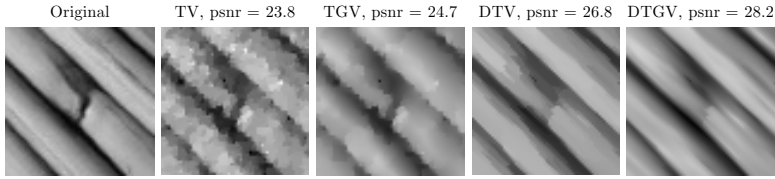


Figure 13: The zoomed-in regions of the restored results shown in the last row of fig. 12.

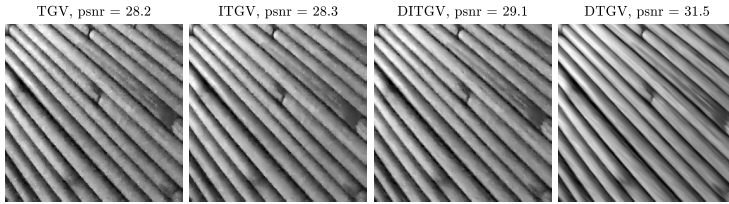


Figure 14: Comparison of TGV, ITGV, DITGV and DTGV regularizers for denoising problem with 10% Gaussian noise.

our method to deal with multi-directions or spatially varying directions in the future.

Acknowledgements

The work was supported by Advanced Grant 291405 from the European Research Council and grant no. 4002-00123 from the Danish Council for Independent Research Natural Sciences.

References

- [1] H. Attouch, G. Buttazzo, and G. Michaille. *Variational Analysis in Sobolev and BV Spaces: Applications to PDEs and Optimization*. Number 1. 2006.
- [2] G. Aubert and P. Kornprobst. *Mathematical problems in image processing: partial differential equations and the calculus of variations*. 2006.
- [3] I. Bayram and M. E. Kamasak. A directional total variation. *Eur. Signal Process. Conf.*, 19(12):265–269, 2012.
- [4] A. Beck and M. Teboulle. A fast iterative shrinkage-thresholding algorithm for linear inverse problems. *SIAM J. Imaging Sci.*, 2(1):183–202, jan 2009.
- [5] B. Berkels, M. Burger, M. Droske, O. Nemitz, and M. Rumpf. Cartoon extraction based on anisotropic image classification. *Proc. Vision, modeling and visualization*, pages 293–300, 2006.

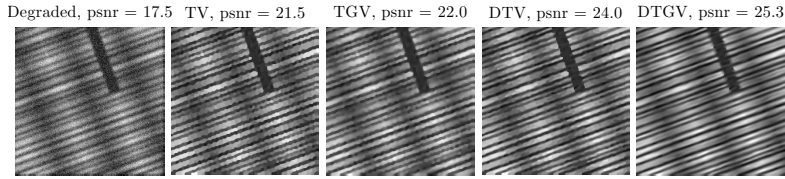


Figure 15: Comparison of TV, TGV, DTV and DTGV regularizers for a piece-wise affine noisy blurred image.

- [6] S. Boyd, N. Parikh, E. Chu, B. Peleato, and J. Eckstein. Distributed optimization and statistical learning via the alternating direction method of multipliers. *Found. Trends® in Mach. Learn.*, 3(1):1–122, 2010.
- [7] K. Bredies. *Recovering piecewise smooth multichannel images by minimization of convex functionals with total generalized variation penalty*, pages 44–77. Springer Berlin Heidelberg, Berlin, Heidelberg, 2014.
- [8] K. Bredies, K. Kunisch, and T. Pock. Total generalized variation. *SIAM J. Imaging Sci.*, 3(3):492–526, 2010.
- [9] K. Bredies and T. Valkonen. Inverse problems with second-order total generalized variation constraints. *Int. Conf. Sampl. Theory Appl.*, pages 1–4, 2011.
- [10] A. Chambolle and T. Pock. A first-order primal-dual algorithm for convex problems with applications to imaging. *J. Math. Imaging Vis.*, 40(1):120–145, dec 2011.
- [11] T. Chan, A. Marquina, and P. Mulet. High-order total variation-based image restoration. *SIAM J. Sci. Comput.*, 22(2):503–516, 2000.
- [12] T. Chan and C. K. Wong. Total variation blind deconvolution. *IEEE Trans. Image Process.*, 7(3):370–5, 1998.
- [13] A. H. Delaney and Y. Bresler. Globally convergent edge-preserving regularized reconstruction: An application to limited-angle tomography. *IEEE Trans. Image Process.*, 7(2):204–221, 1998.
- [14] Y. Dong, M. Hintermüller, and M. Neri. An efficient primal-dual method for L^1 TV image restoration. *SIAM J. Appl. Math.*, 2(4):1168–1189, 2009.
- [15] Y. Dong and T. Zeng. A convex variational model for restoring blurred images with multiplicative noise. *SIAM J. Appl. Math.*, 6(3):1598–1625, 2013.
- [16] G. R. Easley, D. Labate, and F. Colonna. Shearlet-based total variation diffusion for denoising. *IEEE Trans. Image Process.*, 18(2):260–268, 2009.
- [17] S. Esedoglu and S. J. Osher. Decomposition of images by the anisotropic Rudin-Osher-Fatemi model. *Commun. Pure Appl. Math.*, 57(12):1609–1626, 2004.

- [18] V. Estellers, S. Soatto, and X. Bresson. Adaptive regularization with the structure tensor. *IEEE Trans. Image Process.*, 24(6):1777–1790, 2015.
- [19] X. Fei, Z. Wei, and L. Xiao. Iterative directional total variation refinement for compressive sensing image reconstruction. *Signal Process. Lett. IEEE*, 20(11):1070–1073, 2013.
- [20] C. Fernandez-Granda and E. J. Candes. Super-resolution via transform-invariant group-sparse regularization. *2013 IEEE Int. Conf. Comput. Vis.*, pages 3336–3343, 2013.
- [21] D. Ferstl, C. Reinbacher, R. Ranftl, M. Ruether, and H. Bischof. Image guided depth upsampling using anisotropic total generalized variation. *Proc. IEEE Int. Conf. Comput. Vis.*, pages 993–1000, 2013.
- [22] G. H. Granlund and H. Knutsson. *Signal Processing for Computer Vision*. Springer-Science+Business Media Dordrecht, 1995.
- [23] D. Hafner, C. Schroers, and J. Weickert. Introducing maximal anisotropy into second order coupling models. *Ger. Conf. Pattern Recognit.*, 9358:79–90, 2015.
- [24] M. Holler and K. Kunisch. On infimal convolution of total variation type functionals and applications. *SIAM J. Imaging Sci. J. Imaging Sci.*, 7(4):2258–2300, 2014.
- [25] K. M. Jespersen, J. Zangenberg, T. Lowe, P. J. Withers, and L. P. Mikkelsen. Fatigue damage assessment of uni-directional non-crimp fabric reinforced polyester composite using X-ray computed tomography. *Compos. Sci. Technol.*, 136:94–103, 2016.
- [26] K. M. Jespersen, J. Zangenberg, T. Lowe, P. J. Withers, and L. P. Mikkelsen. X-ray CT Data: Fatigue Damage in Glass Fibre/polyester Composite Used for Wind Turbine Blades [Data-set], 2016.
- [27] E. Jonsson, T. Chan, and S.-C. Huang. Total variation regularization in positron emission tomography. Technical report, Dept. Mathematics, Univ. California., Los Angeles., 1998.
- [28] S. Lefkimmiatis, A. Roussos, P. Maragos, and M. Unser. Structure tensor total variation. *SIAM J. Imaging Sci.*, 8(2):1090–1122, 2015.
- [29] Y. Nesterov. A method of solving a convex programming problem with convergence rate $O(1/k^2)$. *Sov. Math. Dokl.*, 27(2):372–376, 1983.
- [30] M. Nikolova. Local strong homogeneity of a regularized estimator. *SIAM J. Appl. Math.*, 61(2):633–658, 2000.
- [31] R. Ranftl, S. Gehrig, T. Pock, and H. Bischof. Pushing the limits of stereo using variational stereo estimation. *IEEE Intell. Veh. Symp. Proc.*, (1):401–407, 2012.
- [32] W. Ring. Structural properties of solutions to total variation regularization problems. *ESAIM: M2AN*, 34(4):799–810, 2000.

- [33] L. I. Rudin, S. Osher, and E. Fatemi. Nonlinear total variation based noise removal algorithms. *Phys. D Nonlinear Phenom.*, 60(1-4):259–268, 1992.
- [34] S. R. Sandoghchi, G. T. Jasion, N. V. Wheeler, S. Jain, Z. Lian, J. P. Wooler, R. P. Boardman, N. K. Baddela, Y. Chen, J. R. Hayes, E. N. Fokoua, T. Bradley, D. R. Gray, S. M. Mousavi, M. N. Petrovich, F. Poletti, and D. J. Richardson. X-ray tomography for structural analysis of microstructured and multimaterial optical fibers and preforms. *Opt. Express*, 22(21):26181, 2014.
- [35] O. Scherzer. Denoising with higher order derivatives of bounded variation and an application to parameter estimation. *Computing*, 60(1):1–27, 1998.
- [36] F. Sciacchitano, Y. Dong, and T. Zeng. Variational approach for restoring blurred images with Cauchy noise. *SIAM J. Appl. Math.*, 8(3):1894–1922, 2015.
- [37] S. Setzer and G. Steidl. Variational methods with higher order derivatives in image processing. *Approx. Theory XII San Antonio 2007*, pages 360–385, 2008.
- [38] S. Setzer, G. Steidl, and T. Teuber. Restoration of images with rotated shapes. *Numer. Algorithms*, 48(1-3):49–66, 2008.
- [39] S. Setzer, G. Steidl, and T. Teuber. Infimal convolution regularizations with discrete ll-type functionals. *Commun. Math. Sci.*, 9(3):797–827, 2011.
- [40] R. Temam. *Mathematical Problems in Plasticity*. Gauthier-Villars, 1985.
- [41] E. Turgay and G. B. Akar. Directionally adaptive super-resolution. *2009 16th IEEE Int. Conf. Image Process.*, (1):1201–1204, 2009.
- [42] C. R. Vogel and M. E. Oman. Iterative methods for total variation denoising. *SIAM J. Sci. Comput.*, 17(1):227–238, 1996.
- [43] J. Weickert. Anisotropic diffusion in image processing. *Image Rochester NY*, 256(3):170, 1998.
- [44] J. Weickert. Coherence-enhancing diffusion filtering. *Int. J. Comput. Vis.*, 31(2):111–127, 1999.
- [45] J. Weickert, B. M. T. H. Romeny, and M. A. Viergever. Efficient and reliable schemes for nonlinear diffusion filtering. *IEEE Trans. Image Process.*, 7:398–410, 1998.
- [46] H. Zhang and Y. Wang. Edge adaptive directional total variation. *J. Eng.*, (October):1–2, 2013.

APPENDIX

Directional Total Generalized Variation Regularization for Impulse Noise Removal

In Scale Space and Variational Methods in Computer Vision 2017, 6667, pp. 221–231, 6th International Conference, SSVM 2017, Kolding, Denmark, June 4–8, 2017, Proceedings.

doi:[10.1007/978-3-319-58771-4](https://doi.org/10.1007/978-3-319-58771-4)

R. D. Kongskov and Y. Dong

Copyright 2017 Springer International Publishing AG

Directional Total Generalized Variation Regularization for Impulse Noise Removal

Rasmus Dalgas Kongskov^(✉) and Yiqiu Dong

Applied Mathematics and Computer Science at Technical University of Denmark,
Kongens Lyngby, Denmark
rara@dtu.dk

Abstract. A recently suggested regularization method, which combines directional information with total generalized variation (TGV), has been shown to be successful for restoring Gaussian noise corrupted images. We extend the use of this regularizer to impulse noise removal and demonstrate that using this regularizer for directional images is highly advantageous. In order to estimate directions in impulse noise corrupted images, which is much more challenging compared to Gaussian noise corrupted images, we introduce a new Fourier transform-based method. Numerical experiments show that this method is more robust with respect to noise and also more efficient than other direction estimation methods.

Keywords: Directional total generalized variation · Impulse noise · Variational methods · Regularization · Image restoration

1 Introduction

The use of variational methods is a successful way to improve image restoration by incorporating prior information through regularization, see e.g. [18, 20, 23, 25]. For images corrupted by blurring and impulse noise, ℓ^1 -fidelity-based variational models are effectively demonstrated their success as seen in [3, 5, 16, 17, 19, 20]. In this paper, we will study restoration of impulse noise corrupted directional images.

An image $u \in \mathbb{R}^{N \times N}$ is assumed to be degraded as

$$f = \mathcal{N}(Au),$$

where A is a known blurring operator, \mathcal{N} indicates degradation with impulse noise, and $f \in \mathbb{R}^{N \times N}$ is the degraded image. Impulse noise often appears due to e.g. transmission errors or malfunctioning pixels. Impulse noise is known for not degrading all image pixels, but only a part of them. The two most common types of impulse noise are salt-and-pepper noise and random-valued impulse noise. Let $\rho \in [0, 1]$ be the noise-level. The model for impulse noise degradation at pixel (i, j) is

$$f_{i,j} = \begin{cases} b_{i,j}, & \text{with probability } \rho, \\ (Au)_{i,j}, & \text{with probability } 1 - \rho. \end{cases}$$

We assume the intensity range as $[0, 1]$. For salt-and-pepper noise, we have $b_{i,j} \in \{0, 1\}$ for all (i, j) , while for random-valued impulse noise, $b_{i,j}$ is random and uniform distributed in $[0, 1]$. A variational model for restoring the impulse noise corrupted image takes the form

$$\min_u \|Au - f\|_1 + \mathcal{R}(u).$$

The choice of regularization term \mathcal{R} should reflect what prior knowledge we have for the image u .

Total Variation (TV) is a very popular used regularization in image processing, which corresponds to a piecewise constant prior [23]. The combination of ℓ^1 data-fitting and TV-regularization has been investigated for impulse noise in [5, 7, 16, 20]. A drawback for TV-regularized methods is the so called stair-casing effect, which can be successfully overcome by regularization with higher-order derivatives, e.g. Total Generalized Variation (TGV) regularization proposed in [2].

In series of applications, processing of images with a distinct main direction is typical. This could for example be different fibre materials such as carbon, glass optical fibres, see [13, 24, 27]. Images with a the texture following one main direction we dub directional images. Including the directional information in an image processing setting can highly improve the image quality and hence improve the material analysis.

TV-regularization has been combined with directional information for several applications and in various aspects, see [1, 8–10, 15, 26]. Directionality has also been combined with second-order derivative regularization in [12] and with the first-order information of second-order TGV, see [11, 22]. Recently in [14] a regularization method for restoring directional images has been introduced, which combines TGV with directional information estimated from the images. In [14] directional TGV (DTGV) is demonstrated to improve the quality of restorations in the case of Gaussian noise.

In this paper, we investigate DTGV-regularized variational methods for restoring impulse noise corrupted images. Under impulse noise, how to estimate the main direction is a big challenge. In order to obtain a robust direction estimation algorithm, we utilize the Fourier transform and propose a new algorithm. Numerical results show that the new direction estimation algorithm outperforms the one proposed in [14] under both impulse noise and Gaussian noise cases, and it is much more efficient due to the fast Fourier transform algorithm and non-iterative structure. With the estimated main direction, DTGV regularization is combined with the ℓ^1 data-fitting term. The minimization problem in the new variational model is solved by a primal-dual method [4]. The numerical results show that our method can successfully restore directional images by removing impulse noise and preserving the texture.

The rest of the paper is organized as follows. In Sect. 2, we briefly review DTGV regularization, and provide a new variational model for restoring directional images under impulse noise. Section 3 gives the new direction estimation algorithm, Sect. 4 gives a primal-dual algorithm for solving our restoration

model. The numerical results shown in Sect. 5 demonstrate the efficiency of the new method. Finally, conclusions are drawn in Sect. 6.

2 ℓ^1 -DTGV Model

In [14], the directional total generalized variation (DTGV) regularization, which is utilized to restore directional images, is proposed. Comparing with the TGV in [2], the idea behind DTGV relies on a change of the feasible set for the dual variable in the definition, i.e., the feasible set is turned from a spherical set into an elliptical set. This change leads to non-identical penalization along each directions. Further, in [14] it is shown that the change of the feasible set can be boiled down to the modification of the operators, which is much more implementation-friendly.

In this paper, we only consider the discrete case. Then, the discrete second order DTGV (DTGV_λ^2) of $u \in \mathbb{R}^{N \times N}$ can be written as:

$$\text{DTGV}_\lambda^2(u) = \min_{\mathbf{v} \in \mathbb{R}^{2N \times N}} \lambda_1 \sum_{i,j} |A_a R_{-\theta}(\nabla u)_{i,j} - \mathbf{v}_{i,j}|_2 + \lambda_0 \sum_{i,j} |(\tilde{\mathcal{E}}\mathbf{v})_{i,j}|_F \quad (1)$$

where $\mathbf{v} = (v_1^\top, v_2^\top)^\top \in \mathbb{R}^{2N \times N}$ with $v_1, v_2 \in \mathbb{R}^{N \times N}$, $|\cdot|_F$ denotes Frobenius norm, and $\lambda = (\lambda_1, \lambda_2)^\top$ are positive parameters. Furthermore, the discrete gradient operator $\nabla \in \mathbb{R}^{2N \times N}$ is defined as

$$\nabla u = \begin{pmatrix} \nabla_{x_1} u \\ \nabla_{x_2} u \end{pmatrix},$$

where ∇_{x_1} and ∇_{x_2} are the derivatives along x_1 and x_2 directions, which are obtained by applying the forward finite difference scheme with symmetric boundary condition. In addition, A_a and R_θ are the scaling and rotation matrices

$$R_\theta = \begin{pmatrix} \cos \theta & -\sin \theta \\ \sin \theta & \cos \theta \end{pmatrix} \quad \text{and} \quad A_a = \begin{pmatrix} 1 & 0 \\ 0 & a \end{pmatrix},$$

and $\tilde{\mathcal{E}}$ is the directional symmetrized derivative defined as:

$$(\tilde{\mathcal{E}}\mathbf{v})_{i,j} = -\frac{1}{2} \left[A_a R_{-\theta} \begin{pmatrix} (\nabla_{x_1}^\top v_1)_{i,j} & (\nabla_{x_2}^\top v_1)_{i,j} \\ (\nabla_{x_1}^\top v_2)_{i,j} & (\nabla_{x_2}^\top v_2)_{i,j} \end{pmatrix} + \begin{pmatrix} (\nabla_{x_1}^\top v_1)_{i,j} & (\nabla_{x_1}^\top v_2)_{i,j} \\ (\nabla_{x_2}^\top v_1)_{i,j} & (\nabla_{x_2}^\top v_2)_{i,j} \end{pmatrix} R_\theta A_a \right].$$

Due to the scaling and rotation matrices, DTGV is rotationally variant, whereas TGV is rotationally invariant.

To remove impulse noise, the ℓ^1 data-fitting term in variational methods has been shown to be suitable [20]. For restoring directional images, with the prior information of the main texture direction, we combine the ℓ^1 data-fitting term with DTGV regularization and obtain the ℓ^1 -DTGV model:

$$\min_{u \in \mathbb{R}^{N \times N}} \sum_{i,j} |(Au)_{i,j} - f_{i,j}| + \text{DTGV}_\lambda^2(u). \quad (2)$$

By using DTGV as regularization, the variances along the main direction θ will get more penalization than other directions.

3 Direction Estimation Algorithm

In DTGV, the directional parameter θ is very important. In [14] an algorithm for estimating the main direction from degraded images is presented, and it has been shown to work well for Gaussian noise up to a noise level around 30%. But since this algorithm has a lack of robustness with respect to high level Gaussian noise, it also cannot handle other more complicated types of noise, e.g. impulse noise. Moreover, this method requires solving a minimization problem iteratively, which reduces the computational efficiency. In this section, based on the Fourier transform we will propose a new direction estimation algorithm, which is much more robust with respect to noise and too more efficient.

The new algorithm is based on the fact that 2D Fourier basis functions can be seen as images with a significant main direction. After calculating the discrete 2D Fourier transform

$$c(\omega_1, \omega_2) = \mathcal{F}[f](\omega_1, \omega_2) = \sum_{i,j} f_{i,j} e^{-\frac{2i\pi}{N}(i\omega_1 + j\omega_2)} \quad (\text{imaginary unit : } i),$$

the magnitude of the complex coefficients, c , will provide information on the similarity between the image f and the individual directional basis-functions. If the image f indeed has one main direction, then it would resemble one or a combination of the basis-functions, and the amplitude(s) of the corresponding coefficient(s) would be relatively large. By finding the coefficients with the largest amplitude, we can obtain the main direction of the image. The Fourier based method is outlined in Algorithm 1.

Algorithm 1. Direction estimation algorithm

- 1: Input f .
 - 2: Calculate Fourier transform of f : $c(\omega_1, \omega_2) = \mathcal{F}[f](\omega_1, \omega_2)$.
 - 3: Find max-amplitude spatial frequencies: $(\omega_1^*, \omega_2^*) = \underset{(\omega_1, \omega_2)}{\operatorname{argmax}} |c(\omega_1, \omega_2)|$.
 - 4: Estimate the direction from the spatial frequencies: $\theta = \tan^{-1} \left(\frac{\omega_2^*}{\max(\omega_1^*, \epsilon)} \right)$.
 - 5: **return** θ .
-

Since a 2D Fourier transform is the only computational requirement, which can be calculated by the Fast Fourier transform, the new algorithm is highly efficient.

4 Numerical Algorithm

The objective function in (2) is convex, so convex optimization methods can be used to solve the minimization problem in (2). In this section, we apply a primal-dual method based on the work in [4] for solving (2).

According to the definition of DTGV_λ^2 in (1), we give the primal-dual formulation of (2):

$$\begin{aligned} \min_{u \in \mathcal{U}, \mathbf{v} \in \mathcal{V}} \max_{q \in \mathcal{Q}, \mathbf{p} \in \mathcal{P}, W \in \mathcal{W}} & \langle Au - f, q \rangle + \sum_{i,j} \langle A_a R_{-\theta} [\nabla u]_{i,j} - \mathbf{v}_{i,j}, \mathbf{p}_{i,j} \rangle \\ & + \sum_{i,j} \langle (\tilde{\mathcal{E}} \mathbf{v})_{i,j}, W_{i,j} \rangle, \end{aligned}$$

where $\mathcal{U} \in \mathbb{R}^{N \times N}$, $\mathcal{V} \in \mathbb{R}^{2N \times N}$, $\mathcal{Q} = \{q \in \mathcal{U} \mid |q_{i,j}| \leq 1 \text{ for } 1 \leq i, j \leq N\}$, $\mathcal{P} = \{\mathbf{p} \in \mathcal{V} \mid |\mathbf{p}_{i,j}|_2 \leq \lambda_1 \text{ for } 1 \leq i, j \leq N\}$, $\mathcal{W} = \{W \mid W_{i,j} \text{ is a 2-by-2 symmetric matrix and } |W_{i,j}|_F \leq \lambda_0 \text{ for } 1 \leq i, j \leq N\}$. This is a generic saddle-point problem, and in Algorithm 2 the primal-dual algorithm proposed in [4] is applied to solve the above optimization task.

In Algorithm 2, η is the dual step-size, τ is the primal step-size, A^* indicates the adjoint operator of A , and the projection operator is defined as

$$[\mathcal{S}_\lambda(\xi)]_{i,j} = \frac{\xi_{i,j}}{\max\left(1, \frac{|\xi_{i,j}|}{\lambda}\right)}.$$

If $\xi \in \mathcal{V}$, then $|\xi_{i,j}|$ is with 2-norm; and if $\xi \in \mathcal{W}$, then $|\xi_{i,j}|$ is with Frobenius norm.

5 Numerical Experiments

In this section, we provide numerical results to study the behavior of our method. We first compare the new direction estimation algorithm in Algorithm 1 with the one given in [14]. After this we compare our method, i.e., restoring directional images from the $\ell^1\text{-DTGV}_\lambda^2$ model, with the one based on the $\ell^1\text{-TGV}_\lambda^2$ model. All numerical experiments are carried out in Matlab on a laptop with a 2.9 GHz Intel Core i5 processor.

5.1 Direction Detection

Here, we use a simulated directional image as test image to compare the performance of the new direction estimation algorithm proposed in Algorithm 1 with the one from [14]. In Fig. 1 we test them on the image with up to 90% Gaussian noise, and in Fig. 2 we test them on the image with up to 90% random-valued impulse noise.

Clearly, the new direction estimation algorithm is much more robust with respect to both kinds of noise. Moreover, it is much more efficient. Average time from 1000 runs on a 256×256 images is only 9 ms by the new algorithm, comparing of 407 ms by the one in [14], which is almost 45 times faster.

Algorithm 2. Primal-dual algorithm for solving ℓ^1 -DTGV model

- 1: Require f, A, λ, a, θ and tol.
- 2: Estimate Lipschitz constant L , e.g. using power-method for A .
- 3: Initialize $u^0 = 0, \bar{u}^0 = 0, \mathbf{p}^0 = 0, q^0 = 0, \mathbf{v}^0 = 0, \bar{\mathbf{v}}^0 = 0, w^0 = 0, e^0 = 0, \eta < \frac{1}{\sqrt{L}}, \tau < \frac{1}{\sqrt{L}}$.
- 4: **while** $e^k > \text{tol}$ **do**

$$\begin{aligned}
\mathbf{p}^{k+1} &= \arg \max_{\mathbf{p} \in \mathcal{P}} \langle \tilde{\nabla} \bar{u}^k - \bar{\mathbf{v}}^k, \mathbf{p} \rangle - \frac{1}{2\eta} \|\mathbf{p} - \mathbf{p}^k\|_2^2 \\
&= \mathcal{S}_{\lambda_1} \left(\mathbf{p}^k + \eta \left(\tilde{\nabla} \bar{u}^k - \bar{\mathbf{v}}^k \right) \right) \\
W^{k+1} &= \arg \max_{W \in \mathcal{W}} \langle \tilde{\mathcal{E}} \bar{\mathbf{v}}^k, W \rangle - \frac{1}{2\eta} \|W - W^k\|_F^2 \\
&= \mathcal{S}_{\lambda_0} \left(W^k + \eta \tilde{\mathcal{E}} \bar{\mathbf{v}}^k \right) \\
q^{k+1} &= \arg \max_{q \in \mathcal{Q}} \langle A \bar{u}^k - f, q \rangle - \frac{1}{2\eta} \|q - q^k\|_2^2 \\
&= \mathcal{S}_1 \left(q^k + \eta (A \bar{u}^k - f) \right) \\
u^{k+1} &= \arg \min_{u \in \mathcal{U}} \langle Au, q^{k+1} \rangle + \langle \tilde{\nabla} u, \mathbf{p}^{k+1} \rangle + \frac{1}{2\tau} \|u - u^k\|_2^2 \\
&= u^k + \tau \left(\widetilde{\text{div}} \mathbf{p}^{k+1} - A^* q^{k+1} \right) \\
\mathbf{v}^{k+1} &= \arg \min_{\mathbf{v} \in \mathcal{V}} -\langle \mathbf{v}, \mathbf{p}^{k+1} \rangle + \langle \tilde{\mathcal{E}} \mathbf{v}, W^{k+1} \rangle + \frac{1}{2\tau} \|\mathbf{v} - \mathbf{v}^k\|_2^2 \\
&= \mathbf{v}^k + \tau \left(\mathbf{p}^{k+1} + \widetilde{\text{div}} W^{k+1} \right) \\
\bar{u}^{k+1} &= 2u^{k+1} - u^k \\
\bar{\mathbf{v}}^{k+1} &= 2\mathbf{v}^{k+1} - \mathbf{v}^k \\
e^{k+1} &= \frac{\|u^k - u^{k+1}\|_2}{\|u^k\|_2}
\end{aligned}$$

end while

- 5: **return** u^{k+1} .

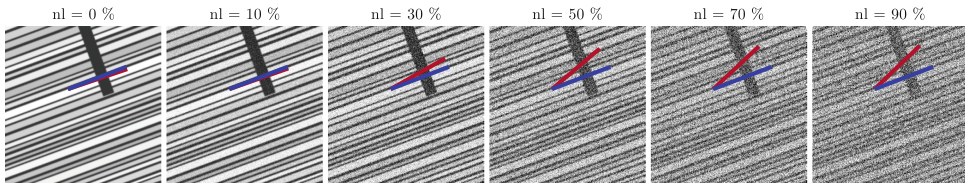


Fig. 1. Estimating the main direction in the test images with additive Gaussian noise (“nl” denotes the noise level). The colored lines indicates the estimated direction by using the method in [14] (red) and the new method (blue). (Color figure online)

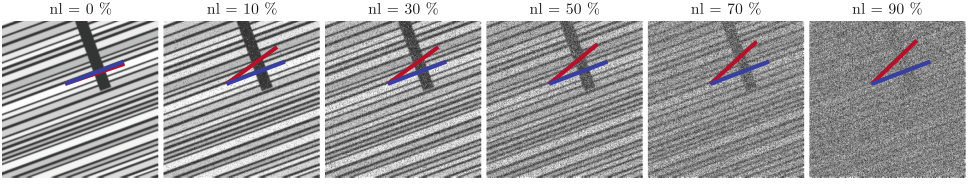


Fig. 2. Estimating the main direction in the test images with random-valued impulse noise (“nl” denotes the noise level). The colored lines indicates the estimated direction by using the method in [14] (red) and the new method (blue). (Color figure online)

5.2 Image Denoising and Deblurring

In this section, we examine the difference between using TGV_{λ}^2 and $DTGV_{\lambda}^2$ as regularizers combined with a ℓ^1 -data fidelity term for restoring images corrupted by impulse noise.

In DTGV, except the main direction parameter θ , there are another three parameters: the scaling parameter a and the regularization parameter $\lambda = (\lambda_0, \lambda_1)$. The scaling parameter a demonstrates to what extent the textures in images following the main direction. If $a = 1$, DTGV becomes identical to the rotation invariant TGV. Due to the good performance of the direction estimation algorithm, as suggested in [14] we choose a relatively small, saying $a < 0.3$. In addition, same as the TGV in [2], we fix the ratio $\frac{\lambda_0}{\lambda_1}$ as 2, which commonly yields good restoration results. All the numerical results shown here are the ones with the highest peak-signal-to-noise-ratio (PSNR) values after adjusting the parameters λ_1 and $a \in (0, 0.3)$.

The first denoising experiment is using a 512×512 test image, which is corrupted by the salt-and-pepper noise with the noise level as 30%, 50% and 70%, respectively. In Fig. 3 the restored results from both regularizers are presented. It is obvious that the DTGV regularizer provides better results, and the improvement of the PSNR values is even more than 10 dB. But in the dark region perpendicular to the main direction we see some artifacts from the DTGV regularization. It is due to the diffusion of the different intensities along the main direction.

In the second denoising experiment, a real bamboo image is used (253×253 pixels). In this image the main direction varies smoothly throughout the image within a range of about 15° . Here, we test our method and the one based on ℓ^1 -TGV model for removing random valued impulse noise, which is much more difficult than the salt-and-pepper noise. The best-PSNR results are shown in Fig. 4. As seen restoring a real image with random-valued impulse noise is a harder problem for both methods, but the improvement of using DTGV is again clear, both visually and quantitatively. Since in the DTGV regularizer we only consider one main direction, the variation of the directional is not taken into account, which leads to some line artifacts.

The deblurring and denoising experiment is also with the bamboo image. Here, we consider the Gaussian blurring with standard deviation $\sigma = 2$ and the

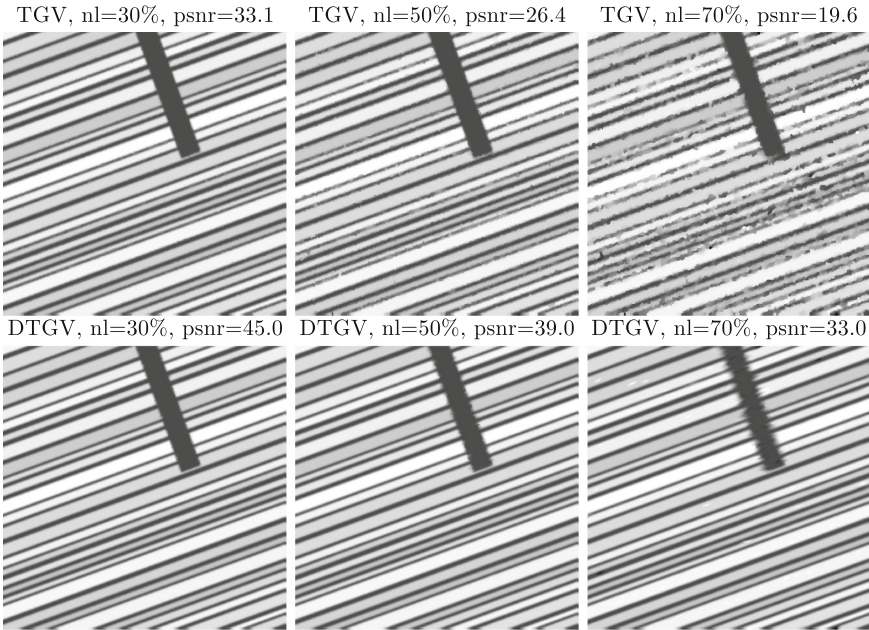


Fig. 3. Denoising results from the salt-and-pepper noise corrupted images.

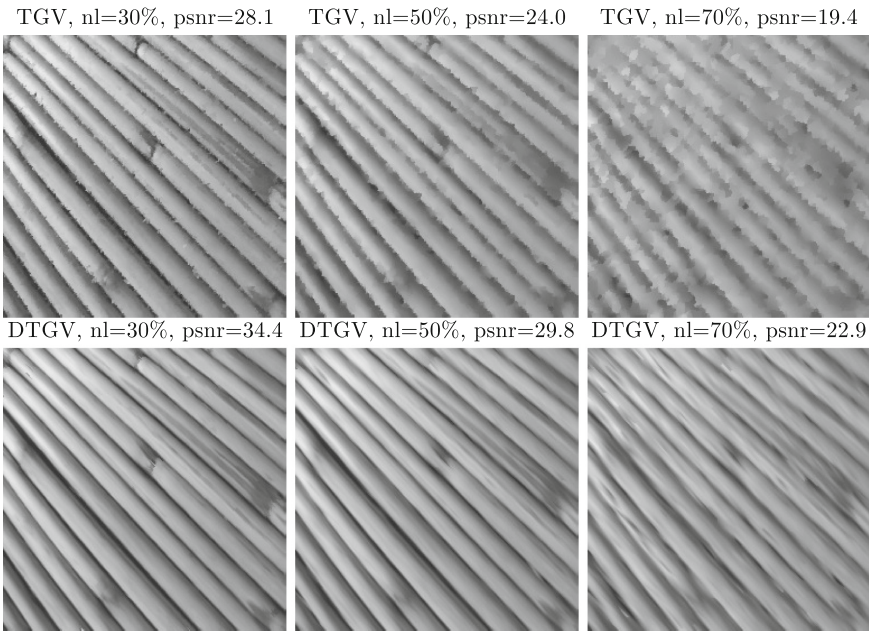


Fig. 4. Denoising results for a real image corrupted by random-valued impulse noise.

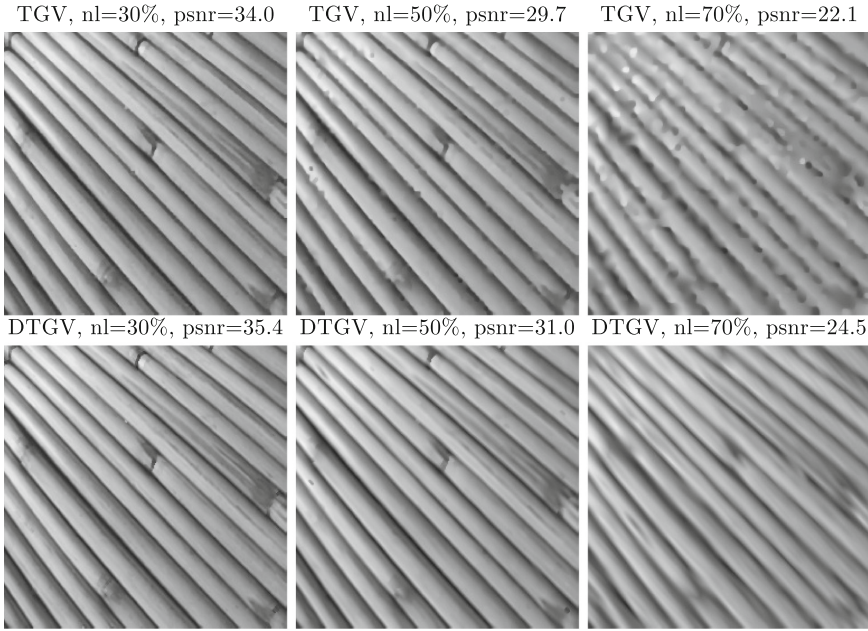


Fig. 5. Restoration results for blur images with random-valued impulse noise.

random valued impulse noise. The best-PSNR results are shown in Fig. 5. Our method with DTGV regularization gives the highest PSNR values in all three different noise level cases. The visual difference also can be observed, especially in high noise level cases.

6 Conclusions

In this paper, we apply a recently proposed directional regularization, DTGV, on image restoration under impulse noise. By combining DTGV with ℓ^1 data-fitting term, we give a new ℓ^1 -DTGV variational model. In order to estimate the main direction directly from impulse noise corrupted images, which is much more challenging than Gaussian noise case, we propose a new direction estimation algorithm based on the Fourier transform. The new algorithm is much more robust with respect to the noise, and furthermore also much more efficient than a previously suggested algorithm in [14]. The numerical results show that our DTGV-regularized method improve the TGV-based method on restoring impulse-noise-corrupted directional images significantly. Hence, there is a high advantage of incorporating the direction information into the regularization for directional image restoration.

In order to further improve the restoration results, especially in high noise level cases, in the future we intend to extend our method to the two-phase approach, referring to the work in [3, 5, 6, 21]. That is, in the first phase we distinguish the noisy pixels, and then in the second phase we utilize the variational method

to restore only noisy pixels from the detected noise-free pixels. The range of applications for this method could be extended by letting the direction vary spatially, which would require a reliable, e.g. adaptive, way to estimate local directions.

Acknowledgments. The authors would like to thank the reviewers for their comments and suggestions, which has helped to improve this article. The work was supported by Advanced Grant 291405 from the European Research Council.

References

1. Bayram, I., Kamasak, M.E.: A directional total variation. *Eur. Signal Process. Conf.* **19**(12), 265–269 (2012)
2. Bredies, K., Kunisch, K., Pock, T.: Total generalized variation. *SIAM J. Imaging Sci.* **3**(3), 492–526 (2010)
3. Cai, J.F., Chan, R.H., Nikolova, M.: Fast two-phase image deblurring under impulse noise. *J. Math. Imaging Vis.* **36**(1), 46–53 (2010)
4. Chambolle, A., Pock, T.: A first-order primal-dual algorithm for convex problems with applications to imaging. *J. Math. Imaging Vis.* **40**(1), 120–145 (2011)
5. Chan, R.H., Dong, Y., Hintermüller, M.: An efficient two-phase L^1 -TV method for restoring blurred images with impulse noise. *IEEE Trans. Image Process.* **19**(7), 1731–1739 (2010)
6. Chan, R.H., Ho, C.W., Nikolova, M.: Salt-and-pepper noise removal by median-type noise detectors and detail-preserving regularization. *IEEE Trans. Image Process.* **14**(10), 1479–1485 (2005)
7. Dong, Y., Hintermüller, M., Neri, M.: An efficient primal-dual method for L^1 TV image restoration. *SIAM J. Imaging Sci.* **2**(4), 1168–1189 (2009)
8. Easley, G.R., Labate, D., Colonna, F.: Shearlet-based total variation diffusion for denoising. *IEEE Trans. Image Process.* **18**(2), 260–268 (2009)
9. Estellers, V., Soatto, S., Bresson, X.: Adaptive regularization with the structure tensor. *IEEE Trans. Image Process.* **24**(6), 1777–1790 (2015)
10. Fei, X., Wei, Z., Xiao, L.: Iterative directional total variation refinement for compressive sensing image reconstruction. *Signal Process. Lett. IEEE* **20**(11), 1070–1073 (2013)
11. Ferstl, D., Reinbacher, C., Ranftl, R., Ruether, M., Bischof, H.: Image guided depth upsampling using anisotropic total generalized variation. *Proc. IEEE International Conference on Computer Vision*, pp. 993–1000 (2013)
12. Hafner, D., Schroers, C., Weickert, J.: Introducing maximal anisotropy into second order coupling models. *Ger. Conf. Pattern Recognit.* **9358**, 79–90 (2015)
13. Jespersen, K.M., Zangenberg, J., Lowe, T., Withers, P.J., Mikkelsen, L.P.: Fatigue damage assessment of uni-directional non-crimp fabric reinforced polyester composite using X-ray computed tomography. *Compos. Sci. Technol.* **136**, 94–103 (2016)
14. Kongskov, R.D., Dong, Y., Knudsen, K.: Directional Total Generalized Variation Regularization. submitted (2017). <http://arxiv.org/abs/1701.02675>
15. Lefkimiatis, S., Roussos, A., Maragos, P., Unser, M.: Structure tensor total variation. *SIAM J. Imaging Sci.* **8**(2), 1090–1122 (2015)
16. Ma, L., Ng, M., Yu, J., Zeng, T.: Efficient box-constrained TV-type-l1 algorithms for restoring images with impulse noise. *J. Comput. Math.* **31**(3), 249–270 (2013)

17. Ma, L., Yu, J., Zeng, T.: Sparse representation prior and total variation-based image deblurring under impulse noise. *SIAM J. Imaging Sci.* **6**(4), 2258–2284 (2013)
18. Mumford, D., Shah, J.: Optimal approximations by piecewise smooth functions and associated variational problems. *Commun. Pure Appl. Math.* **42**(5), 577–685 (1989)
19. Nikolova, M.: Minimizers of cost-functions involving nonsmooth data-fidelity terms. Application to the processing of outliers. *Siam J. Numer. Anal.* **40**(3), 965–994 (2003)
20. Nikolova, M.: A variational approach to remove outliers and impulse noise. *J. Math. Imaging Vis.* **20**(1–2), 99–120 (2004)
21. Nikolova, M., Chan, R.H., Cai, J.F.: Two-phase approach for deblurring images corrupted by impulse plus Gaussian noise. *Inverse Probl. Imaging* **2**(2), 187–204 (2008)
22. Ranftl, R., Gehrig, S., Pock, T., Bischof, H.: Pushing the limits of stereo using variational stereo estimation. *IEEE Intell. Veh. Symp. Proc.* **1**, 401–407 (2012)
23. Rudin, L.I., Osher, S., Fatemi, E.: Nonlinear total variation based noise removal algorithms. *Phys. D Nonlinear Phenom.* **60**(1–4), 259–268 (1992)
24. Sandoghchi, S.R., Jasion, G.T., Wheeler, N.V., Jain, S., Lian, Z., Wooler, J.P., Boardman, R.P., Baddela, N.K., Chen, Y., Hayes, J.R., Fokoua, E.N., Bradley, T., Gray, D.R., Mousavi, S.M., Petrovich, M.N., Poletti, F., Richardson, D.J.: X-ray tomography for structural analysis of microstructured and multimaterial optical fibers and preforms. *Opt. Express* **22**(21), 26181 (2014)
25. Tikhonov, A.N., Arsenin, V.I.: Solutions of ill-posed problems. Winston, Philadelphia (1977)
26. Turgay, E., Akar, G.B.: Directionally adaptive super-resolution. In: 2009 16th IEEE International Conference on Image Processing vol. 1, 1201–1204 (2009)
27. Zhang, Z., Hartwig, G.: Relation of damping and fatigue damage of unidirectional fibre composites. *Int. J. Fatigue* **24**(7), 713–718 (2002)

APPENDIX D

Tomographic Reconstruction Methods for Decomposing Directional Components

Submitted to Inverse Problems and Imaging

R. D. Kongskov, Y. Dong

Tomographic Reconstruction Methods for Decomposing Directional Components

Rasmus Dalgas Kongskov* Yiqiu Dong*

August 31, 2017

Abstract

The X-ray computed tomography technique has many different practical applications. In this paper, we propose two new reconstruction methods that can decompose and reconstruct objects at the same time. By incorporating direction information, the proposed methods can decompose objects into various directional components. Furthermore we propose a method to obtain the direction information in the objects directly from the measured sinogram data. We demonstrate the proposed methods on simulated and real samples to show their practical applicability. The numerical results show the differences between the two methods and the practical usefulness when dealing with fibre-crack decomposition problem.

1 Introduction

X-ray computed tomography (CT) is a highly used non-invasive imaging technique. Applications of this technique ranges from biological and chemical science, to structural and material science, where the resolution also varies from large scale (meters) to micro-scale (nano-meters). For the CT technique, reconstruction methods play a fundamental role, and very often after the reconstruction we need to segment or decompose the objects into different components. In this paper, we focus on directional objects, whose textures are mainly along one direction. One important example of directional objects is fibres, such as optical fibres, glass fibres, carbon fibres, etc. When analyzing fibre materials, CT scanners can be used to investigate interior properties, for example irregularities, see [22, 24, 12]. A specific irregularity that is often sought for in fibre materials are cracks. Both the fibres and the cracks can be regarded as directional components. Based on this application, we will propose new methods for reconstructing and decomposing directional components simultaneously.

The CT technique is based on the X-ray attenuation as X-rays pass through an object. According to Lambert-Beers law, the measured data, i.e. the sinogram in 2D, can be considered as line integrals of the attenuation coefficients of the object [18, 5]. In the continuous setting, this is integral corresponds to the Radon transform, and in the discrete setting we can write it as a linear equation:

$$Az \approx \mathbf{b}, \tag{1}$$

*Department of Applied Mathematics and Computer Science, Technical University of Denmark, 2800 Kgs. Lyngby, Denmark (rara@dtu.dk, yido@dtu.dk).

where $A \in \mathbb{R}^{N \times M^2}$ represents the CT process, $\mathbf{z} \in \mathbb{R}^{M^2}$ represents the object to be reconstructed, and $\mathbf{b} \in \mathbb{R}^N$ denotes the measured noisy data. The data is measured with N_ϕ scanning angles and N_t detector bins, which gives $N = N_\phi N_t$ rays in total. For simplicity we consider the 2D parallel beam geometry, the work introduced in this paper can be easily extended to fan beam geometry. In addition, we assume to have uniformly distributed scanning angles for the whole 180° .

The most widely used reconstruction method for CT is called Filtered Back-Projection (FBP) [21], which is based on the analytical formulation of inverse Radon transform. Therefore, FBP implicitly assumes to have continuously measured data from the whole 180° angular range. FBP is very efficient, and with sufficient measurements of a low noise level the method provides good results. But when we deal with noisy data and an underdetermined system, FBP will introduce many artifacts. In order to overcome this drawback from FBP and be able to deal with noisy and/or limited data, variational methods can be used. Variational methods have been used for many many different inverse problems, including CT, see [1, 25] for more details. In this paper, we assume that the sinogram data are corrupted by additive white Gaussian noise, which ends up with the following variational model

$$\min_{\mathbf{z}} \frac{1}{2} \|A\mathbf{z} - \mathbf{b}\|_2^2 + \mathcal{R}(\mathbf{z}). \quad (2)$$

In (2) $\mathcal{R}(\mathbf{z})$ is called as regularization term, which incorporates the prior information on the object \mathbf{z} . Many regularization techniques have been proposed, and one of the most commonly used for imaging problems is total variation (TV). TV was first introduced in [23] for image restoration and afterwards was used for CT reconstruction in e.g. [8, 26].

Image decomposition methods was first proposed in [6] by using infimal convolution. The idea is to define two convex functionals J_1 and J_2 with respect to two components z_1 and z_2 and their properties, then by solving the optimization problem

$$\inf \{J_1(z_1) + J_2(z_2)\} \quad \text{s.t.} \quad z = z_1 + z_2$$

a decomposition is achieved. Based on different applications, many image decomposition methods have been proposed, e.g. [17, 9, 27, 2, 3, 10, 11]. Recently, this technique is also applied to CT problems to decompose the reconstruction into the object component, limited data artifacts and the noise component [16].

In this paper, we propose two methods to decompose the objects into directional components. One method is motivated from the microlocal analysis results in [20], and decomposes the objects by splitting the sinogram directly. In order to suppress artifacts from the limited data, variational methods with proper regularizations are introduced. The other method is based on image decomposition by using infimal convolution. We compare the two methods by discussing their theoretical differences, and also demonstrate their performance through empirical examples. In addition, to define the directional components, we also introduce a method to estimate the main direction of an object directly from its sinogram.

The paper is organized as follows. In Section 2 we review a regularization technique proposed in [14] for incorporating direction information. Furthermore, we propose a method to estimate the main direction of an object directly from its

sinogram data. In Section 3 we introduce the sinogram splitting method, where by splitting the sinogram we are able to obtain components along different directions. In Section 4 a image decomposition method by using directional regularization is proposed to decompose directional components. Numerical experiments are carried out in Section 5, and in Section 6 conclusions are drawn.

2 Directional regularization in CT reconstruction

We start this section by reviewing a directional regularization, called directional total variation (DTV), proposed in [4, 14, 13]. This regularization is one kind of anisotropic TV, and very effective for reconstructing directional objects, whose textures are mainly along one specific direction. Afterwards taking the CT scanning geometry into account we propose a method to estimate the main direction of objects directly from the sinogram data.

2.1 Directional regularization

In order to incorporate direction information, a directional regularization, called directional total variation (DTV), was introduced for image denoising and deblurring in [4, 14, 13]. DTV builds on the prior that the object is piece-wise constant and its texture follows one main direction. For an image $\mathbf{z} \in \mathbb{R}^{M \times M}$, its DTV can be defined as

$$\text{DTV}_{\theta,a}(\mathbf{z}) = \sum_{i,j} |R_\theta \Lambda_a (\nabla \mathbf{z})_{i,j}|_2,$$

where

$$R_\theta = \begin{pmatrix} \cos \theta & -\sin \theta \\ \sin \theta & \cos \theta \end{pmatrix} \quad \text{and} \quad \Lambda_a = \begin{pmatrix} 1 & 0 \\ 0 & a \end{pmatrix}, \quad (3)$$

denote the rotation matrix with the angle $\theta \in (0, 2\pi]$ and the scaling matrix with the paramter $a \in (0, 1]$, respectively. In addition, the gradient operator $\nabla : \mathbb{R}^{M \times M} \rightarrow \mathbb{R}^{2M \times M}$ is defined as

$$\nabla \mathbf{z} = \begin{pmatrix} \nabla_{x_1} \mathbf{z} \\ \nabla_{x_2} \mathbf{z} \end{pmatrix} \quad \text{and} \quad (\nabla \mathbf{z})_{i,j} = \begin{pmatrix} (\nabla_{x_1} \mathbf{z})_{i,j} \\ (\nabla_{x_2} \mathbf{z})_{i,j} \end{pmatrix}$$

where ∇_{x_1} and ∇_{x_2} denote the derivatives along the two dimensions x_1 and x_2 , respectively, and can be obtained by applying a forward finite difference scheme with symmetric boundary condition, i.e.,

$$(\nabla_{x_1} \mathbf{z})_{i,j} = \begin{cases} z_{i+1,j} - z_{i,j}, & \text{if } i < M, \\ 0, & \text{if } i = M, \end{cases} \quad \text{and} \quad (\nabla_{x_2} \mathbf{z})_{i,j} = \begin{cases} z_{i,j+1} - z_{i,j}, & \text{if } j < M, \\ 0, & \text{if } j = M. \end{cases}$$

In Figure 1, we give an example to illustrate how the DTV regularization performs when reconstructing directional objects from CT data. In this example, the underdetermined rate, i.e., $\frac{N}{M^2}$, equals $\frac{2}{3}$, and the data are corrupted by 1% additive white Gaussian noise. We compare the result by using the DTV regularization in eqn:varprop with the one from FBP and the one by using total variation (TV) as regularization. It is obvious that the DTV result is superior both quantitatively, based on the peak signal-to-noise ratio (psnr) measure, and visually.

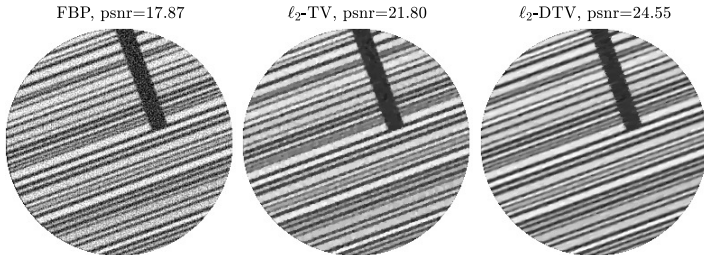


Figure 1: Comparison on simulated CT reconstruction problem. Regularization parameters for the ℓ_2 -TV and ℓ_2 -DTV methods are tuned to maximize the peak-signal-to-noise ratio (psnr). The parameters in DTV are chosen as $a = 0.15$ and $\theta = 20^\circ$.

2.2 Direction estimation from sinogram data

In order to use DTV as regularization we have to select the parameters a and θ . Based on the results in [14] with a good direction estimation $a = 0.15$ usually provides good results. In this section, we focus on the main direction estimation, and propose a method to estimate it directly from sinogram data.

In [13] a direction estimator based on Fourier transform was proposed. This estimator is according to the fact that 2D Fourier basis functions can be seen as images with a significant main direction. Therefore, if the textures of the image are mainly along one direction, the magnitude of the coefficients corresponding to the Fourier basis along the same direction will be relatively large. Although this estimator is robust with respect to the noise, it requires the information in image domain. But in CT reconstruction, we only have sinogram data. To avoid estimating the main direction θ from the reconstruction, we introduce a new direction estimator based on CT scanning geometry.

Since we scan the objects by rotation in CT, the measurements are strongly related with the scanning angle. If we consider the case that the scanning angle is relatively close to the main texture direction θ , then each projection line will only pass through one type of material. Hence, the measurements along θ will be oscillating. We can therefore utilize 1D Fourier transform to check if the measurements along each scanning angle are oscillating, and the largest magnitude of the Fourier coefficients should correspond to the main direction. The detailed algorithm for estimating the main direction is given in Algorithm 1. Note that this direction estimator is not limited to parallel-beam tomography, since a similar oscillating signal also appears when the fan-beam geometry is used.

In order to demonstrate the performance of our direction estimator, we test it on a simulated phantom and a real object from [12]. In both cases we simulate the projections and the noise. In Table 1 we list the estimated direction under different level of additive Gaussian noise, ρ , and in Figure 2 we show the two objects with their sinograms. Furthermore, we indicate the estimated direction from the noise-free sinogram and the sum of the magnitudes along each angle from Algorithm 1. Based on these empirical tests it is clear that up to 20% Gaussian noise the new direction estimator is robust with respect to the noise.

Algorithm 1 Main Direction Estimator

- 1: Input the sinogram data b and the measurement angles $\{\phi_m\}$.
- 2: Compute 1D Fourier transform along each angle ϕ_m :

$$\hat{b}_{\omega,m} = \sum_{l=0}^{N_t-1} b_{l,m} e^{-\frac{2\pi i \omega l}{N_t}}.$$

- 3: Calculate the sum of the magnitudes along each angle ϕ_m and find its maximizer:

$$h = \operatorname{argmax}_m \sum_{\omega} |\hat{b}_{\omega,m}|.$$

- 4: Return the main direction $\theta = \phi_h$.
-

ρ (%)	0	1	3	5	10	20	30	40
Phantom	20.1	20.1	20.1	20.1	20.1	20.1	20.1	31.7
Real	81.5	81.7	81.5	80.9	81.7	79.5	-1.1	-34.9

Table 1: Direction estimation results for the phantom and real objects shown in Figure 2. Note that the exact main direction for the phantom is 20° .

3 Sinogram Splitting Method

Microlocal analysis (MLA) have been used to determine which singular features, such as edges, we can expect to recover in a range of continuous tomography problems. In [20] the relation between singularities in a function f and singularities in its Radon transform $\mathcal{A}f$ is described. The paradigm that is described in [20] is further outlined in [15] as follows:

\mathcal{A} detects singularities of f perpendicular to the line of integration ("visible" singularities), but singularities of f in other ("invisible") directions do not create singularities of $\mathcal{A}f$ near the line of integration.

The fact that singularities only propagate when X-rays are perpendicular to them inspired us to split the sinogram in order to decompose the objects into several components along different directions. Here, each splitted part of the sinogram is related to an object component where the directions of the singularities, in the object-domain, are limited. In the following, we focus on a two-component split, which can be easily extended to decompose any integer amount of components with different directions.

Assume the two object components are \mathbf{u} and \mathbf{w} , and both are in \mathbb{R}^{M^2} . The textures of \mathbf{u} are mainly along the directions with the angles $\phi_u \in \mathbb{R}^K$, and \mathbf{w} mainly contains the textures along the other angles $\phi_w \in \mathbb{R}^{N-K}$. Based on MLA, we known that we need measurements along the same angles as the texture, in order to reconstruct it. We therefore split the sinogram and the system matrix according to ϕ_u and ϕ_w and obtain:

$$A_u \mathbf{u} \approx \mathbf{b}_u \quad \text{and} \quad A_w \mathbf{w} \approx \mathbf{b}_w, \quad (4)$$

where $A_u \in \mathbb{R}^{KN_t \times M^2}$ and $A_w \in \mathbb{R}^{(N-K)N_t \times M^2}$ are the splitted matrices, and $\mathbf{b}_u \in \mathbb{R}^{KN_t}$ and $\mathbf{b}_w \in \mathbb{R}^{(N-K)N_t}$ are the splitted noisy sinograms. Here, we

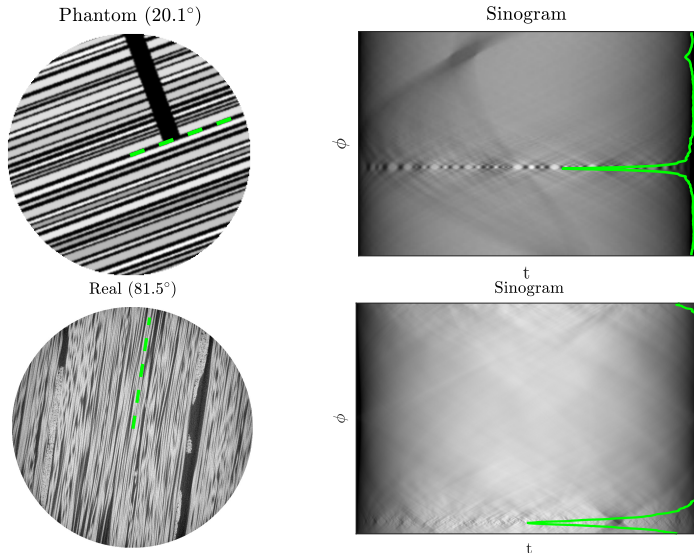


Figure 2: Left: the objects with estimated direction from the noise-free sinogram. Right: the noise-free sinogram overlaid with the plot of the sum of the magnitudes.

assume that K is a natural number and larger than 1 in order to avoid reconstructing \mathbf{u} from only a single-angle measurement.

To solve the linear systems in (4), we can use FBP. Since FBP is based on the analytic solution of the Radon transform in the continuous setting it requires continuous projections from all angles. With limited angle problems, the data according to the missing angles are implicitly filled by 0. For the systems (4) it is identical to the assumptions:

$$A_u \mathbf{w} = 0, \quad \text{and} \quad A_w \mathbf{u} = 0. \quad (5)$$

On one hand, due to the artificial singularities in the sinograms at the transition between the measured data and the assumed 0-data, artifacts will appear in both \mathbf{u} and \mathbf{w} ; on the other hand, according to the assumptions we have

$$\begin{bmatrix} A_u \\ A_w \end{bmatrix} (\mathbf{u} + \mathbf{w}) \approx \begin{bmatrix} \mathbf{b}_u \\ \mathbf{b}_w \end{bmatrix}, \quad (6)$$

which means that $\mathbf{u} + \mathbf{w}$ is reconstructed from the whole sinogram, and the limited angle artifacts in \mathbf{u} and \mathbf{w} will cancel each other.

Besides the limited angle artifacts appearing in reconstruction results from FBP, FBP is also very sensitive to the noise in the sinogram. In order to obtain good reconstructions from noisy data with limited angles, we can use variational methods by incorporating prior information on the individual components. Based

on the linear systems (4) we get the following two variational models for reconstructing \mathbf{u} and \mathbf{w} :

$$\min_{\mathbf{u} \geq 0} \frac{1}{2} \|A_u \mathbf{u} - \mathbf{b}_u\|_2^2 + \mathcal{R}_u(\mathbf{u}), \quad (7)$$

$$\min_{\mathbf{w} \geq 0} \frac{1}{2} \|A_w \mathbf{w} - \mathbf{b}_w\|_2^2 + \mathcal{R}_w(\mathbf{w}), \quad (8)$$

where the regularization terms \mathcal{R}_u and \mathcal{R}_w should depend on the prior information on each component. For example, for the fibre-crack decomposition problem, the prior for the fibre-component is that it is piecewise constant and its textures mainly follow one direction θ , however, the prior for the crack-component is that it is independent on the direction, piece-wise constant and sparse. Based on these priors we suggest the following regularizations:

$$\begin{aligned} \mathcal{R}_u(\mathbf{u}) &= \lambda_u \text{DTV}_{\theta, a_u}(\mathbf{u}), \\ \mathcal{R}_w(\mathbf{w}) &= \lambda_w \text{TV}(\mathbf{w}) + \beta \|\mathbf{w}\|_1, \end{aligned}$$

where λ_u and λ_w are positive regularization parameters, which control the balance between the fit to the data and the regularization. With these two regularizer choices, both optimization problems in (7) and (8) are convex, and many convex optimization methods can be used to solve them.

4 Image Decomposition Method

In [3, 10], texture-cartoon decomposition methods built on the infimal convolution technique are proposed. Based on this work, we introduce another method to decompose directional components from sinogram data in this section.

In many applications fibre-structures are analyzed with the aim to detect cracks and/or other types of deterioration. Whereas the texture of the fibre material follows one main direction θ , the deteriorated parts are mainly perpendicular, or close to perpendicular, to the main direction. Moreover the deteriorated parts are sparse in the object. Based on these observations we propose the following decomposition model:

$$\min_{\mathbf{u} \geq 0, \mathbf{w}} \frac{1}{2} \|A(\mathbf{u} + \mathbf{w}) - \mathbf{b}\|_2^2 + \lambda \left(\text{DTV}_{\theta, a_u}(\mathbf{u}) + \alpha \text{DTV}_{\theta^\perp, a_w}(\mathbf{w}) \right) + \beta \|\mathbf{w}\|_{\ell^1}, \quad (9)$$

where $\mathbf{u} \in \mathbb{R}^{M^2}$ represents the fibres, $\mathbf{w} \in \mathbb{R}^{M^2}$ the crack part, and $\lambda, \alpha, \beta > 0$ are regularization parameters. The model (9) is convex, which is desirable when we want to find a solution to the minimization problem. Furthermore the sparsity constraint is not only a reasonable regularization method for \mathbf{w} , it also makes (9) strictly convex, i.e. the minimizer will be unique.

We have introduced two different methods for combined decomposition and reconstruction, the sinogram splitting method and the image decomposition method, and now we sum up the relations and differences between these two methods. The sinogram splitting method has a risk to reconstruct incorrect attenuation coefficient values due to the splitting into two limited angle problems, which are much more complicated to solve. If we use the variational methods in (7) and (8) to reconstruct the components, the results are not summable. On the other hand, if we use FBP, based on (6) the components are summable, and the results are

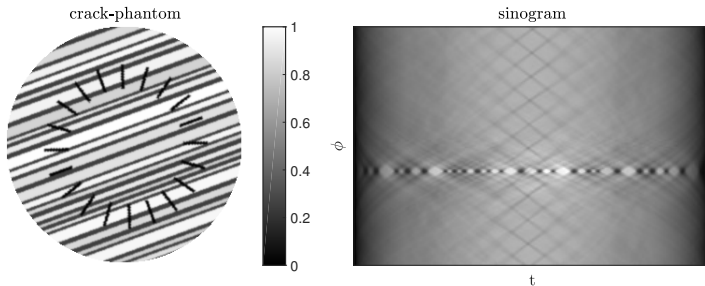


Figure 3: Left: fibre-crack phantom with fibres along the direction 20° and cracks in a circular pattern. Right: simulated noise-free sinogram.

identical to decompose the objects under the constraint (5). In addition, comparing with \mathcal{R}_u and \mathcal{R}_w in (7) and (8), the regularization in (9) plays a different role. In (7) and (8) the main purpose of utilizing regularization technique is to remove the limited angle artifacts that occur due to splitting the sinogram, but in (9) the regularization is used for decomposing the components.

5 Numerical Experiments

In this section we demonstrate the performance of the methods introduced in Section 3 and 4 on two simulated X-ray CT problems. In order to set the stage for the numerical experiments we first give some discretization and experiment details which are valid for the following tests.

We solve the variational optimization problems by using the Primal-Dual-Hybrid-Gradient (PDHG) method proposed in [7] with the stopping rule

$$\frac{|\mathcal{J}(\cdot_{k+1}) - \mathcal{J}(\cdot_k)|}{|\mathcal{J}(\cdot_k)|} < 10^{-5},$$

where \mathcal{J} denotes the objective function. For (9) we solve the subproblems with respect to \mathbf{u} and \mathbf{w} alternately by using PDHG method. All of the algorithms are implemented in Matlab, where we use the parallel beam GPU code described in [19] from the ASTRA toolbox, see [29, 28], to calculate Radon transform and its adjoint operator.

5.1 Sinogram splitting method

For the sinogram splitting method we compare the two reconstruction techniques presented in Section 3, namely FBP and the variational method. Both reconstruction methods are tested on a simulated fibre-crack phantom shown in Figure 3, which has cracks in a 360° circular pattern in order to illustrate the performance of decomposition. In the test, the sinogram is simulated with $N_t = 256$ detector bins, $N_\phi = 171$ scanning angles and the reconstruction grid-size is $M = 256$, which make the underdetermined rate as $\frac{N_\phi}{M^2} = \frac{2}{3}$. Further, the sinogram is corrupted with 1% additive white Gaussian noise. In Figure 4 we compare the two methods with a split parameter $K = 11$ and centered by the estimated main

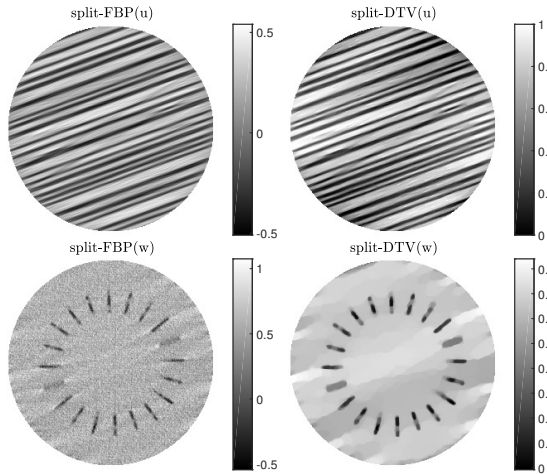


Figure 4: Comparison of two sinogram-splitting methods introduced in Section 3.

direction from Algorithm 1. For the variational method on splitted sinogram, we choose the optimal λ_u and λ_w based on visual inspection, i.e., the reconstructed \mathbf{u} has clear edges within similar intensity range as the ground truth and \mathbf{w} has a homogeneous background and sharp crack edges.

In Figure 4 we see that both reconstructed fibre components (\mathbf{u}) are visually similar, but the colorbar shows that the intensity range by FBP has an offset of around 0.5. Comparing the reconstructed crack components (\mathbf{w}) it is obvious that the result from FBP is much more noisy than the one from the variational method. In addition, all of the cracks are located in the crack components, which is due to a highly directional object and a good choice of the range-width index $K = 10$. An interesting observation is that the cracks along the main direction are also present in crack components, and the reason is that the boundaries of the cracks, which are perpendicular to the main direction, are present in \mathbf{b}_w .

To show the role of the parameter K , in Figure 5 we show the results from the variational method with different values of K . It is clear that a small K will result in some fibre elements falling into the crack-component, whereas a large K will result in some cracks appearing in the fibre component. The choice of K should be according to prior knowledge about the object, e.g. if the object is highly directional a relatively low value will be sufficient.

5.2 Image decomposition method

In the image decomposition model (9) several parameters need to be given. The main direction angle θ for fibre component is estimated by Algorithm 1, and a_u is fixed as 0.15 based on the empirical tests in [14]. For the crack component, θ^\perp is orthogonal to the main direction, and $a_w = 0.5$ in order to allow the model to decompose the cracks that are not strictly perpendicular to the main direction and still avoid ending up as TV. In order to avoid one feasible set from the two DTV terms fully covering the other, α should satisfy $a_u < \alpha < \frac{1}{a_w}$, i.e. $0.15 < \alpha < 2$.

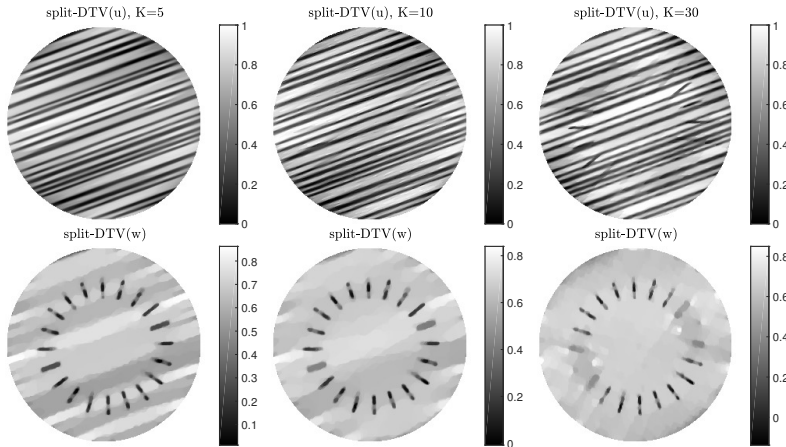


Figure 5: Influence of K on the results from the sinogram splitting method using DTV-regularized reconstruction.

In the numerical tests, we tune the parameters λ , α and β such that the psnr value of $\mathbf{u} + \mathbf{w}$ to the ground truth \mathbf{z} is maximum.

In Figure 6, we show the reconstruction results with different α values. To avoid that the sparsity constraint influences the results, we fix $\beta = 10^{-6}$. It is obvious that a small α will result in more details as well as noise in the crack component and a large α will leave many cracks in the fibre component.

In Figure 7, we demonstrate the improvement of including the sparsity constraint in the image decomposition method by comparing the results from $\beta = 10^{-6}$ and $\beta = 10^{-4}$. From the results we see a clear improvement on both components by using larger β . The intensity range for the fibre-component is much more accurate and cracks have much sharper edges. The improvement is also reflected by a slight increase of the psnr value.

5.3 Comparison of the sinogram splitting method with the image decomposition method

Comparing the results shown in Figure 4 and 7, we can see that the sinogram splitting method delivers a much more complete split between the fibres and the cracks along any given direction. From the sinogram splitting method the crack component contains a non-homogeneous background and some artifacts. Furthermore, some cracks are wider than they should be, which is due to the limited scanning angles and the smoothness from the regularization. The image decomposition method performs better on decomposing the cracks along the perpendicular direction to θ because of the regularization. When the sparsity constraint is enforced, we can see that the background of the crack component is homogeneous, while the edges of the cracks are still sharp.

Next, we compare the two methods on a real sample object, which is a carbon fibre sample and shown in Figure 8. The sample is with the size $M = 426$, and

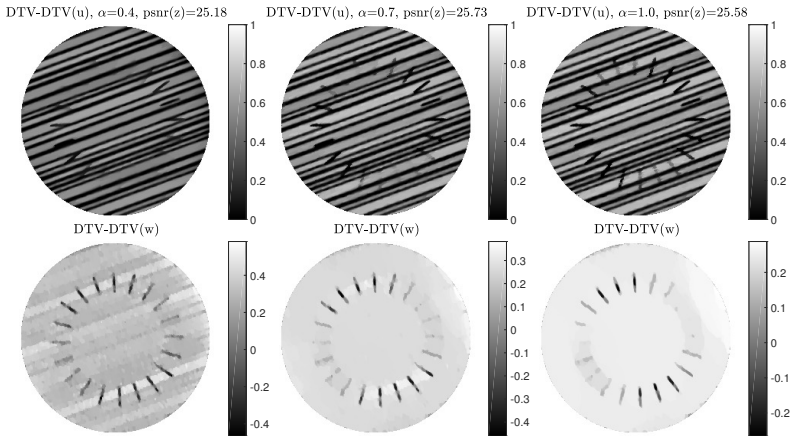


Figure 6: Comparison of the decomposition results from different α by using the image decomposition method.

we simulate $N_t = 426$ detector bins and $N_\phi = 284$ scanning angles with 1% Gaussian noise in the sinogram. In Figure 9 we show the results from FBP-based and variational-based sinogram splitting method as well as image decomposition method. The regularization parameters are tuned based on visual inspection, where we prioritize the decomposition of cracks. In addition, in the sinogram splitting method the range-width index K is set to 120, which is much larger than the one in Figure 4. The reason is to avoid fibre textures appearing in the crack component.

From Figure 9, we can see that the results from the FBP-based sinogram splitting method are clearly influenced by noise and limited angle artifacts. In the results from the variational-based sinogram splitting method the edges of the fibres along the main direction are sharp, but other edges are blurry due to the limited scanning angles. In addition, the crack component suffers from a non-homogeneous background and the stair-casing artifacts, which makes it difficult to distinguish cracks. Comparing with the results from the sinogram splitting method, the image decomposition method produces sharper edges in the fibre component and decomposes the parts that could be categorized as cracks to the crack component. Especially, the homogeneous background in the crack component will benefit distinguishing cracks.

6 Conclusions

We propose two new tomographic reconstruction methods and aim to decompose components including textures along different directions. We compare the two methods by discussing their theoretical differences, and also propose a new method for estimating the main object direction directly from measured computed tomography data. The proposed methods are compared empirically on both a simulated phantom and a real object. The simulated phantom is used for

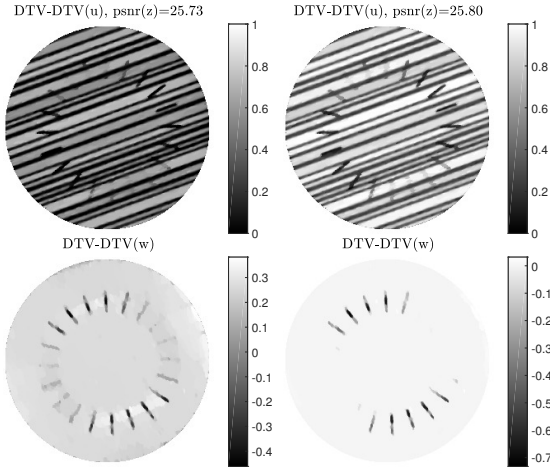


Figure 7: Comparison of the decomposition results from different β by using the image decomposition method. Here, we fixed $\alpha = 0.7$ and $\lambda = 0.0038$.

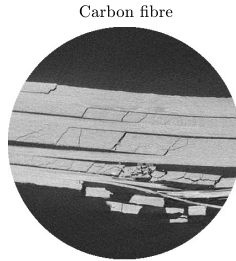


Figure 8: Carbon fibre sample from [22].

general performance tests of the methods. In these tests we demonstrate what can be achieved with the proposed methods. The real data sample tests show how well these methods perform in practice.

Acknowledgements

The work was supported by Advanced Grant 291405 from the European Research Council.

References

- [1] G. Aubert and P. Kornprobst. *Mathematical Problems in Image Processing: Partial Differential Equations and the Calculus of Variations*. Springer Science + Business Media, 2006.

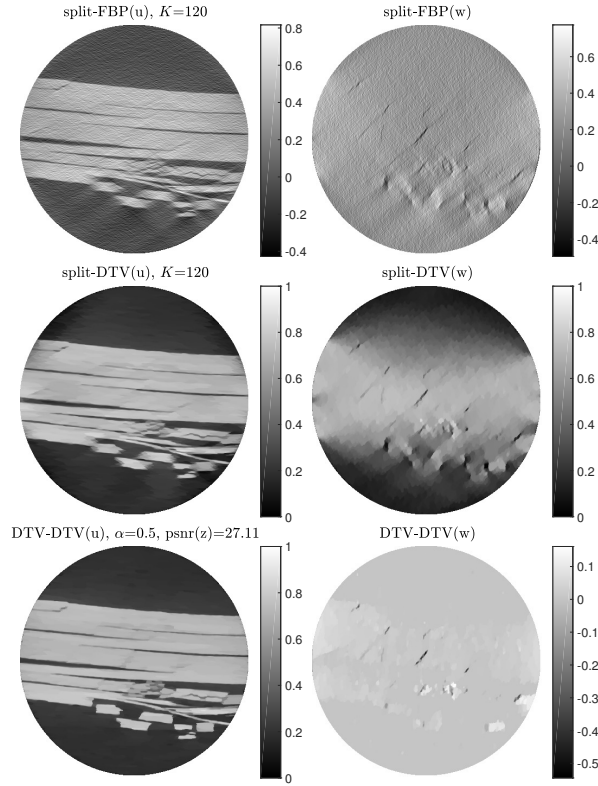


Figure 9: Comparison of the sinogram splitting method with the image decomposition method on real objects.

- [2] J. F. Aujol, G. Aubert, L. Blanc-Féraud, and A. Chambolle. Image decomposition into a bounded variation component and an oscillating component. *J. Math. Imaging Vis.*, 22(1):71–88, 2005.
- [3] J. F. Aujol, G. Gilboa, T. Chan, and S. Osher. Structure-texture image decomposition-modeling, algorithms, and parameter selection. *Int. J. Comput. Vis.*, 67(1):111–136, 2006.
- [4] I. Bayram and M. E. Kamasak. A directional total variation. *Eur. Signal Process. Conf.*, 19(12):265–269, 2012.
- [5] T. M. Buzug. *Computed Tomography : From Photon Statistics to Modern Cone-Beam CT*. Springer, 2008.
- [6] A. Chambolle and P.-L. Lions. Image recovery via total variation minimization and related problems. *Numer. Math.*, 76(2):167–188, 1997.

- [7] A. Chambolle and T. Pock. A first-order primal-dual algorithm for convex problems with applications to imaging. *J. Math. Imaging Vis.*, 40(1):120–145, dec 2011.
- [8] A. H. Delaney and Y. Bresler. Globally convergent edge-preserving regularized reconstruction: An application to limited-angle tomography. *IEEE Trans. Image Process.*, 7(2):204–221, 1998.
- [9] S. Esedoglu and S. J. Osher. Decomposition of images by the anisotropic Rudin-Osher-Fatemi model. *Commun. Pure Appl. Math.*, 57(12):1609–1626, 2004.
- [10] J. Gilles. Noisy image decomposition: A new structure, texture and noise model based on local adaptivity. *J. Math. Imaging Vis.*, 28(3):285–295, 2007.
- [11] M. Holler and K. Kunisch. On infimal convolution of total variation type functionals and applications. *SIAM J. Imaging Sci. J. Imaging Sci.*, 7(4):2258–2300, 2014.
- [12] K. M. Jespersen, J. Zangenberg, T. Lowe, P. J. Withers, and L. P. Mikkelsen. Fatigue damage assessment of uni-directional non-crimp fabric reinforced polyester composite using X-ray computed tomography. *Compos. Sci. Technol.*, 136:94–103, 2016.
- [13] R. D. Kongskov and Y. Dong. Directional total generalized variation regularization for impulse noise removal Rasmus. *Scale Sp. Var. Methods Comput. Vis. 2017*, 6667:221–231, 2017.
- [14] R. D. Kongskov, Y. Dong, and K. Knudsen. Directional total generalized variation regularization. <http://arxiv.org/abs/1701.02675>, 2017.
- [15] V. P. Krishnan and E. T. Quinto. *Handbook of Mathematical Methods in Imaging*. Springer Science + Business Media, 2015.
- [16] J. Li, C. Miao, Z. Shen, G. Wang, and H. Yu. Robust frame based x-ray ct reconstruction. *Journal of Computational Mathematics*, 34(6):683, 2016.
- [17] Y. Meyer. *Oscillating Patterns in Image Processing and Nonlinear Evolution Equations*, volume 22. American Mathematical Society, 2001.
- [18] F. Natterer. *The Mathematics of Computerized Tomography*, volume 29. John Wiley & Sons Ltd. and B G Teubner, Stuttgart, 1986.
- [19] W. J. Palenstijn, K. J. Batenburg, and J. Sijbers. Performance improvements for iterative electron tomography reconstruction using graphics processing units (GPUs). *J. Struct. Biol.*, 176(2):250–253, 2011.
- [20] E. T. Quinto. Singularities of the X-ray transform and limited data tomography in \mathbb{R}^2 and \mathbb{R}^3 . *SIAM J. Math. Anal.*, 24(5):1215–1225, 1993.
- [21] J. Radon. Über die Bestimmung von Funktionen durch ihre Integralwerte längs gewisser Mannigfaltigkeiten. *Akad. Wiss.*, 69:262–277, 1917.
- [22] J. E. Rouse. *Characterisation of Impact Damage in Carbon Fibre Reinforced Plastics by 3D X-Ray Tomography*. PhD thesis, University of Manchester, 2012.

- [23] L. I. Rudin, S. Osher, and E. Fatemi. Nonlinear total variation based noise removal algorithms. *Phys. D Nonlinear Phenom.*, 60(1-4):259–268, 1992.
- [24] S. R. Sandoghchi, G. T. Jasion, N. V. Wheeler, S. Jain, Z. Lian, J. P. Wooler, R. P. Boardman, N. K. Baddela, Y. Chen, J. R. Hayes, E. N. Fokoua, T. Bradley, D. R. Gray, S. M. Mousavi, M. N. Petrovich, F. Poletti, and D. J. Richardson. X-ray tomography for structural analysis of microstructured and multimaterial optical fibers and preforms. *Opt. Express*, 22(21):26181, 2014.
- [25] O. Scherzer. *Handbook of Mathematical Methods in Imaging*. Springer Science + Business Media, 2010.
- [26] E. Y. Sidky and X. Pan. Image reconstruction in circular cone-beam computed tomography by constrained, total-variation minimization. *Phys. Med. Biol.*, 53(17):4777–4807, sep 2008.
- [27] J. L. Starck, M. Elad, and D. L. Donoho. Image Decomposition via the combination of sparse representation and a variational approach. *IEEE Trans. Image Process.*, 14(10):1570–1582, 2005.
- [28] W. van Aarle, W. J. Palenstijn, J. Cant, E. Janssens, F. Bleichrodt, A. Dabravolski, J. De Beenhouwer, K. Joost Batenburg, and J. Sijbers. Fast and flexible X-ray tomography using the ASTRA toolbox. *Opt. Express*, 24(22):25129, 2016.
- [29] W. van Aarle, W. J. Palenstijn, J. De Beenhouwer, T. Altantzis, S. Bals, K. J. Batenburg, and J. Sijbers. The ASTRA Toolbox: A platform for advanced algorithm development in electron tomography. *Ultramicroscopy*, 157:35–47, 2015.

Bibliography

- [1] W. van Aarle et al. *Fast and flexible X-ray tomography using the ASTRA toolbox*. *Opt. Express* 24.(22) (2016), 25129. DOI: [10.1364/OE.24.025129](https://doi.org/10.1364/OE.24.025129).
- [2] J. Als-Nielsen and D. McMorrow. *Elements of Modern X-ray Physics: Second Edition*. 2011. DOI: [10.1002/9781119998365](https://doi.org/10.1002/9781119998365).
- [3] K. J. Arrow, L. Hurwicz, and H. Uzawa. *Studies in linear and non-linear programming*. *Econ. Rev.* 11.(3) (July 1958), 229.
- [4] G. Aubert and P. Kornprobst. *Mathematical Problems in Image Processing: Partial Differential Equations and the Calculus of Variations*. 2006.
- [5] J. F. Aujol, G. Gilboa, T. Chan, and S. Osher. *Structure-texture image decomposition-modeling, algorithms, and parameter selection*. *Int. J. Comput. Vis.* 67.(1) (2006), 111–136. DOI: [10.1007/s11263-006-4331-z](https://doi.org/10.1007/s11263-006-4331-z).
- [6] R. Bamler and P. Hartl. *Synthetic aperture radar interferometry*. *Inverse Probl.* 14.(4) (1998), 55. DOI: [10.1088/0266-5611/14/4/001](https://doi.org/10.1088/0266-5611/14/4/001).
- [7] J. Banhart et al. *Advanced Tomographic Methods in Materials Research and Engineering*. Vol. 51. 4. 2008, p. 461. DOI: [10.1093/acprof:oso/9780199213245.001.0001](https://doi.org/10.1093/acprof:oso/9780199213245.001.0001).
- [8] H. H. Barrett and K. J. Myers. *Foundations of Image Science*. 2004.
- [9] K. J. Batenburg and J. Sijbers. *DART: A practical reconstruction algorithm for discrete tomography*. *IEEE Trans. Image Process.* 20.(9) (2011), 2542–2553. DOI: [10.1109/TIP.2011.2131661](https://doi.org/10.1109/TIP.2011.2131661).

- [10] A. Beck and M. Teboulle. *A fast iterative shrinkage-thresholding algorithm for linear inverse problems*. *Soc. Ind. Appl. Math. J. Imaging Sci.* 2.(1) (Jan. 2009), 183–202. DOI: [10.1137/080716542](#).
- [11] S. Beucher and C. Lantuejoul. *Use of watersheds in contour detection*. 1979.
- [12] F. E. Boas and D. Fleischmann. *CT artifacts: Causes and reduction techniques*. *Imaging Med.* 4.(2) (2012), 229–240.
- [13] U. Bonse and M. Hart. *An X-ray interferometer*. *Appl. Phys. Lett.* 6.(8) (1965), 155–156. DOI: [10.1063/1.1754212](#).
- [14] L. Borcea. *Electrical impedance tomography*. *Inverse Probl.* 18.(6) (Dec. 2002), R99–R136. DOI: [10.1088/0266-5611/18/6/201](#).
- [15] M. Bosch de Basea et al. *Trends and patterns in the use of computed tomography in children and young adults in Catalonia — results from the EPI-CT study*. *Pediatr. Radiol.* 46.(1) (2016), 119–129. DOI: [10.1007/s00247-015-3434-5](#).
- [16] S. Boyd, N. Parikh, E. Chu, B. Peleato, and J. Eckstein. *Distributed optimization and statistical learning via the alternating direction method of multipliers*. *Found. Trends® Mach. Learn.* 3.(1) (2010), 1–122. DOI: [10.1561/22000000016](#).
- [17] S. Boyd and L. Vandenberghe. *Convex Optimization*. Cambridge: Cambridge University Press, 2004.
- [18] Y. Boykov, O. Veksler, and R. Zabih. *Fast approximate energy minimization via graph cuts*. *IEEE Trans. Pattern Anal. Mach. Intell.* 23.(11) (2001), 1222–1239. DOI: [10.1109/34.969114](#).
- [19] K. Bredies, K. Kunisch, and T. Pock. *Total generalized variation*. *SIAM J. Imaging Sci.* 3.(3) (2010), 492–526. DOI: [10.1137/090769521](#).
- [20] T. M. Buzug. *Computed Tomography: From Photon Statistics to Modern Cone-Beam CT*. Berlin: Springer, 2008.
- [21] R. H. Byrd, P. Lu, J. Nocedal, and C. Zhu. *A limited memory algorithm for bound constrained optimization*. *SIAM J. Sci. Comput.* 16.(5) (1995), 1190–1208. DOI: [10.1137/0916069](#).
- [22] E. J. Candès, J. K. Romberg, and T. Tao. *Stable signal recovery from incomplete and inaccurate measurements*. *Commun. Pure Appl. Math.* 59.(8) (2006), 1207–1223. DOI: [10.1002/cpa.20124](#).
- [23] E. Candès and J. Romberg. *Sparsity and incoherence in compressive sampling*. *Inverse Probl.* 23.(3) (2007), 969–985. DOI: [10.1088/0266-5611/23/3/008](#).
- [24] V. Caselles, R. Kimmel, and G. Sapiro. *Geodesic active contours*. *Proc. IEEE Int. Conf. Comput. Vis.* 10.(10) (2001), 694–699. DOI: [10.1109/ICCV.1995.466871](#).
- [25] A. Chambolle. *An algorithm for total variation minimization and applications*. *J. Math. Imaging Vis.* Vol. 20. (1-2). 2004, p. 89–97.

- [26] A. Chambolle and T. Pock. *A first-order primal-dual algorithm for convex problems with applications to imaging*. *J. Math. Imaging Vis.* 40.(1) (Dec. 2011), 120–145. DOI: [10.1007/s10851-010-0251-1](https://doi.org/10.1007/s10851-010-0251-1).
- [27] A. Chambolle and T. Pock. *An introduction to continuous optimization for imaging*. *Acta Numer.* 25.(2016) (2016), 161–319. DOI: [10.1017/S096249291600009X](https://doi.org/10.1017/S096249291600009X).
- [28] T. F. Chan and C. K. Wong. *Total variation blind deconvolution*. *IEEE Trans. Image Process.* 7.(3) (1998), 370–5. DOI: [10.1109/83.661187](https://doi.org/10.1109/83.661187).
- [29] T. Chan, A. Marquina, and P. Mulet. *High-order total variation-based image restoration*. *SIAM J. Sci. Comput.* 22.(2) (2000), 503–516. DOI: [10.1137/S1064827598344169](https://doi.org/10.1137/S1064827598344169).
- [30] D. Chapman et al. *Diffraction enhanced x-ray imaging*. *Phys. Med. Biol.* 42.(11) (1997), 2015–25.
- [31] C. David, B. Nöhammer, H. H. Solak, and E. Ziegler. *Differential x-ray phase contrast imaging using a shearing interferometer*. *Appl. Phys. Lett.* 81.(17) (2002), 3287–3289. DOI: [10.1063/1.1516611](https://doi.org/10.1063/1.1516611).
- [32] A. H. Delaney and Y. Bresler. *Globally convergent edge-preserving regularized reconstruction: An application to limited-angle tomography*. *IEEE Trans. Image Process.* 7.(2) (1998), 204–221. DOI: [10.1109/83.660997](https://doi.org/10.1109/83.660997).
- [33] Y. Dong, M. Hintermüller, and M. Neri. *An efficient primal-dual method for L^1 TV image restoration*. *SIAM J. Imaging Sci.* 2.(4) (2009), 1168–1189. DOI: [10.1137/090758490](https://doi.org/10.1137/090758490).
- [34] D. L. Donoho. *Compressed sensing*. *IEEE Trans. Inf. Theory* 52.(4) (2006), 1289–1306.
- [35] H. W. Engl, M. Hanke, and A. Neubauer. *Regularization of Inverse Problems*. Kluwer Academic Publishers, 1996, p. 321.
- [36] J. E. Esser. *Primal Dual Algorithms for Convex Models and Applications to Image Restoration, Registration and Nonlocal Inpainting*. *Methods* (2010).
- [37] J. A. Fessler. *Statistical image reconstruction methods for transmission tomography*. *Handb. Med. Imaging, Vol. 2. Med. Image Process. Anal.* (2000), 1–70. DOI: [10.1117/3.831079.ch1](https://doi.org/10.1117/3.831079.ch1).
- [38] M. A. Figueiredo and J. M. Bioucas-Dias. *Restoration of poissonian images using alternating direction optimization*. *IEEE Trans. Image Process.* 19.(12) (2010), 3133–3145. DOI: [10.1109/TIP.2010.2053941](https://doi.org/10.1109/TIP.2010.2053941).
- [39] A. S. Fraser. *Probability and Statistics: Theory and Applications*. Toronto: DAI Press, 1976.
- [40] J. Friel. *Sparse regularization in limited angle tomography*. *Appl. Comput. Harmon. Anal.* 34.(1) (2013), 117–141. DOI: [10.1016/j.acha.2012.03.005](https://doi.org/10.1016/j.acha.2012.03.005).
- [41] J. Friel and E. T. Quinto. *Characterization and reduction of artifacts in limited angle tomography*. *Inverse Probl.* 29.(12) (2013), 125007. DOI: [10.1088/0266-5611/29/12/125007](https://doi.org/10.1088/0266-5611/29/12/125007).

- [42] S. Geman and D. Geman. *Stochastic relaxation, Gibbs distributions, and the Bayesian restoration of images*. *IEEE Trans. Pattern Anal. Mach. Intell.* PAMI-6.(6) (1984), 721–741. DOI: [10.1109/TPAMI.1984.4767596](#).
- [43] G. Gilboa. *A total variation spectral framework for scale and texture analysis*. *SIAM J. Imaging Sci.* 7.(4) (2014), 1937–1961. DOI: [10.1137/130930704](#).
- [44] G. Gilboa and S. Osher. *Nonlocal operators with applications to image processing*. *Multiscale Model. Simul.* 7.(3) (2009), 1005–1028. DOI: [10.1137/070698592](#).
- [45] J. Gilles. *Noisy image decomposition: A new structure, texture and noise model based on local adaptivity*. *J. Math. Imaging Vis.* 28.(3) (2007), 285–295. DOI: [10.1007/s10851-007-0020-y](#).
- [46] M. Grasmair and F. Lenzen. *Anisotropic total variation filtering*. *Appl. Math. Optim.* 62.(3) (2010), 323–339. DOI: [10.1007/s00245-010-9105-x](#).
- [47] W. Guo, J. Qin, and W. Yin. *A new detail-preserving regularization scheme*. *SIAM J. Imaging Sci.* 7.(2) (2014), 1309–1334.
- [48] J. Hadamard. *Lectures on Cauchy’s Problem in Linear Partial Differential Equations*. New Haven, CT: Yale University Press, 1923.
- [49] J. Hale. *The Fundamentals of Radiological Science*. Thomas, 1974.
- [50] P. C. Hansen. *Discrete Inverse Problems: Insight and Algorithms*. Philadelphia, PA: SIAM, 2010. DOI: [10.1137/1.9780898718836](#).
- [51] P. C. Hansen. *Rank-deficient and Discrete Ill-posed Problems: Numerical Aspects of Linear Inversion*. Philadelphia, PA: SIAM, 1998.
- [52] P. C. Hansen and M. Saxild-Hansen. *AIR tools - A MATLAB package of algebraic iterative reconstruction methods*. *J. Comput. Appl. Math.* 236.(8) (2012), 2167–2178. DOI: [10.1016/j.cam.2011.09.039](#).
- [53] G. T. Herman. *Image Reconstruction From Projections*. New York: New York: Academic, 1980.
- [54] E. Jonsson, T. Chan, and S.-C. Huang. *Total variation regularization in positron emission tomography*. Tech. rep. Los Angeles.: Dept. Mathematics, Univ. California., 1998.
- [55] J. S. Jørgensen. *Sparse Image Reconstruction in Computed Tomography*. PhD thesis. Technical University of Denmark, 2013.
- [56] A. C. Kak and M. Slaney. *Principles of Computerized Tomographic Imaging*. Philadelphia, PA: IEEE Press, 1988, p. 327. DOI: [10.1118/1.1455742](#).
- [57] M. Kass, A. Witkin, and D. Terzopoulos. *Snakes: Active contour models*. *Int. J. Comput. Vis.* 331 (1988), 321–331. DOI: [10.1007/BF00133570](#).
- [58] J. Kim, A. Tsai, M. Cetin, and A. S. Willsky. *A curve evolution-based variational approach to simultaneous image restoration and segmentation*. *Proceedings. Int. Conf. Image Process.* Vol. 1. 2002, p. I–109–I–112 vol.1. DOI: [10.1109/ICIP.2002.1037971](#).

- [59] A. Kirsch. *An Introduction to the Mathematical Theory of Inverse Problems*. Vol. 120. Springer, 2011, pp. 1–323. DOI: [10.1007/978-1-4419-8474-6](#).
- [60] E. Klann, R. Ramlau, and W. Ring. *A Mumford-Shah level-set approach for the inversion and segmentation of SPECT/CT data*. *Inverse Probl. Imaging* (2011).
- [61] A. Kostenko. *Phase-Contrast X-ray Tomography for Soft and Hard Condensed Matter*. PhD thesis. Technical University of Delft, 2013.
- [62] M. Langer, P. Cloetens, J.-P. Guigay, and F. Peyrin. *Quantitative comparison of direct phase retrieval algorithms in in-line phase tomography*. *Med. Phys.* 35.(10) (2008), 4556. DOI: [10.1118/1.2975224](#).
- [63] S. Lefkimmiatis, A. Roussos, P. Maragos, and M. Unser. *Structure tensor total variation*. *SIAM J. Imaging Sci.* 8.(2) (2015), 1090–1122. DOI: [10.1137/14098154X](#).
- [64] T. Lei and W. Sewchand. *Statistical approach to X-ray CT imaging and its applications in image analysis. II. A new stochastic model-based image segmentation technique for X-ray CT image*. *IEEE Trans. Med. Imaging* 11.(1) (1992), 62–69. DOI: [10.1109/42.126911](#).
- [65] D. Liu and J. Yu. *Otsu method and K-means*. *Proc. - 2009 9th Int. Conf. Hybrid Intell. Syst. HIS 2009*. Vol. 1. 2009, p. 344–349. DOI: [10.1109/HIS.2009.74](#).
- [66] A. K. Louis and F. Natterer. *Mathematical problems of computerized tomography*. *Proc. IEEE* 71.(3) (1983), 379–389. DOI: [10.1109/PROC.1983.12596](#).
- [67] J. Mueller and S. Siltanen. *Linear and Nonlinear Inverse Problems with Practical Applications*. 2012, xiii, 351 pages.
- [68] D. Mumford and J. Shah. *Optimal approximations by piecewise smooth functions and associated variational problems*. *Commun. Pure Appl. Math.* 42.(5) (1989), 577–685. DOI: [10.1002/cpa.3160420503](#).
- [69] F. Natterer. *The Mathematics of Computerized Tomography*. John Wiley & Sons Ltd. and B G Teubner, Stuttgart, 1986. DOI: [10.1118/1.1429631](#).
- [70] F. Natterer and F. Wubbeling. *Mathematical Methods in Image Reconstruction*. 1 999. 2001, pp. 1–6. DOI: [10.1118/1.1455744](#).
- [71] Y. Nesterov. *Smooth minimization of non-smooth functions*. *Math. Program.* 103.(1) (May 2005), 127–152. DOI: [10.1007/s10107-004-0552-5](#).
- [72] M. Nikolova. *A variational approach to remove outliers and impulse noise*. *J. Math. Imaging Vis.* 20.(1-2) (2004), 99–120.
- [73] J. Nocedal and S. J. Wright. *Numerical Optimization*. Berlin, 2006.
- [74] P. Ochs, Y. Chen, T. Brox, and T. Pock. *iPiano: Inertial proximal algorithm for nonconvex optimization*. *SIAM J. Imaging Sci.* 7.(2) (2014), 1388–1419. DOI: [10.1137/130942954](#).

- [75] A. Olivo and R. Speller. *A coded-aperture technique allowing x-ray phase contrast imaging with conventional sources*. *Appl. Phys. Lett.* 91.(7) (2007). DOI: [10.1063/1.2772193](#).
- [76] S. Osher and J. A. Sethian. *Fronts propagating with curvature-dependent speed: Algorithms based on Hamilton-Jacobi formulations*. *J. Comput. Phys.* 79.(1) (1988), 12–49. DOI: [10.1016/0021-9991\(88\)90002-2](#).
- [77] N. Otsu. *A threshold selection method from gray-level histograms*. *IEEE Trans. Syst. Man. Cybern.* 20.(1) (1979), 62–66. DOI: [10.1109/TSMC.1979.4310076](#).
- [78] R. L. Parker. *Geophysical Inverse Theory*. Princeton university press, 1994.
- [79] D. L. Phillips. *A technique for the numerical solution of certain integral equations of the first kind*. *J. ACM* 9.(1) (Jan. 1962), 84–97. DOI: [10.1145/321105.321114](#).
- [80] T. Pock, D. Cremers, H. Bischof, and A. Chambolle. *An algorithm for minimizing the Mumford-Shah functional*. *Proc. IEEE Int. Conf. Comput. Vis.* (813396) (2009), 1133–1140. DOI: [10.1109/ICCV.2009.5459348](#).
- [81] J. Radon. *Über die Bestimmung von Funktionen durch ihre Integralwerte längs gewisser Mannigfaltigkeiten*. *Berichte der Sächsischen Akad. der Wiss.* 69 (1917), 262–277. DOI: [10.1090/psapm/027/692055](#).
- [82] R. Ramlau and W. Ring. *A Mumford–Shah level-set approach for the inversion and segmentation of X-ray tomography data*. *J. Comput. Phys.* 221.(2) (2007), 539–557.
- [83] M. Romanov, A. B. Dahl, Y. Dong, and P. C. Hansen. *Simultaneous tomographic reconstruction and segmentation with class priors*. *Inverse Probl. Sci. Eng.* 24.(8) (2016), 1432–1453. DOI: [10.1080/17415977.2015.1124428](#).
- [84] S. D. Rose, M. S. Andersen, E. Y. Sidky, and X. Pan. *TV-constrained incremental algorithms for low-intensity CT image reconstruction*. *Nucl. Sci. Symp. Med. Imaging Conf. (NSS/MIC), 2015 IEEE*. IEEE, 2015, p. 1–3.
- [85] J. E. Rouse. *Characterisation of Impact Damage in Carbon Fibre Reinforced Plastics by 3D X-ray Tomography*. PhD thesis. University of Manchester, 2012.
- [86] L. I. Rudin, S. Osher, and E. Fatemi. *Nonlinear total variation based noise removal algorithms*. *Phys. D Nonlinear Phenom.* 60.(1-4) (1992), 259–268. DOI: [10.1016/0167-2789\(92\)90242-F](#).
- [87] J. Sarvas. *Basic mathematical and electromagnetic concepts of the biomagnetic inverse problem*. *Phys. Med. Biol.* 32.(1) (1987), 11–22. DOI: [10.1088/0031-9155/32/1/004](#).
- [88] O. Scherzer. *Denoising with higher order derivatives of bounded variation and an application to parameter estimation*. *Computing* 60.(1) (1998), 1–27. DOI: [10.1007/BF02684327](#).

- [89] O. Scherzer, H. Grossauer, F. Lenzen, M. Grasmair, and M. Haltmeier. *Variational Methods in Imaging*. Vol. 167. Springer-Verlag New York, 2009, pp. 1–322. DOI: [10.1007/978-0-387-69277-7](https://doi.org/10.1007/978-0-387-69277-7).
- [90] F. Sciacchitano. *Image Reconstruction Under Non-Gaussian Noise*. PhD thesis. Technical University of Denmark, 2017.
- [91] S. Setzer, G. Steidl, and T. Teuber. *Deblurring Poissonian images by split Bregman techniques*. *J. Vis. Commun. Image Represent.* 21.(3) (2010), 193–199. DOI: [10.1016/j.jvcir.2009.10.006](https://doi.org/10.1016/j.jvcir.2009.10.006).
- [92] S. Setzer and G. Steidl. *Variational methods with higher order derivatives in image processing*. *Approx. Theory XII San Antonio 2007* (2008), 360–385.
- [93] E. Y. Sidky, J. H. Jørgensen, and X. Pan. *Convex optimization problem prototyping for image reconstruction in computed tomography with the Chambolle-Pock algorithm*. *Phys. Med. Biol.* 57.(10) (May 2012), 3065–91. DOI: [10.1088/0031-9155/57/10/3065](https://doi.org/10.1088/0031-9155/57/10/3065).
- [94] E. Y. Sidky and X. Pan. *Image reconstruction in circular cone-beam computed tomography by constrained, total-variation minimization*. *Phys. Med. Biol.* 53.(17) (Sept. 2008), 4777–4807. DOI: [10.1088/0031-9155/53/17/021](https://doi.org/10.1088/0031-9155/53/17/021).
- [95] S. Soltani, M. S. Andersen, and P. C. Hansen. *Tomographic image reconstruction using training images*. *J. Comput. Appl. Math.* 313 (2017), 243–258. DOI: [10.1016/j.cam.2016.09.019](https://doi.org/10.1016/j.cam.2016.09.019).
- [96] M. Storath, A. Weinmann, J. Friel, and M. Unser. *Joint image reconstruction and segmentation using the Potts model*. *Inverse Probl.* 31.(2) (2015), 025003. DOI: [10.1088/0266-5611/31/2/025003](https://doi.org/10.1088/0266-5611/31/2/025003).
- [97] M. M. Ter-Pogossian. *The physical aspects of diagnostic radiology*. Hoeber Medical Division, Harper & Row, 1967.
- [98] Z. Tian, X. Jia, K. Yuan, T. Pan, and S. B. Jiang. *Low-dose CT reconstruction via edge-preserving total variation regularization*. *Phys. Med. Biol.* 56.(18) (2011), 5949–67. DOI: [10.1088/0031-9155/56/18/011](https://doi.org/10.1088/0031-9155/56/18/011).
- [99] A. N. Tikhonov. *Solution of incorrectly formulated problems and the regularization method*. *Sov. Math. Dokl.* 4 (1963), 1035–1038.
- [100] A. N. Tikhonov and V. Y. Arsenin. *Solutions of Ill-Posed Problems*. 1978. DOI: [10.2307/2006360](https://doi.org/10.2307/2006360).
- [101] C. R. Vogel and M. E. Oman. *Iterative methods for total variation denoising*. *SIAM J. Sci. Comput.* 17.(1) (1996), 227–238. DOI: [10.1137/0917016](https://doi.org/10.1137/0917016).
- [102] Z. Wang, A. C. Bovik, H. R. Sheikh, and E. P. Simoncelli. *Image quality assessment: From error visibility to structural similarity*. *IEEE Trans. Image Process.* 13.(4) (2004), 600–612. DOI: [10.1109/TIP.2003.819861](https://doi.org/10.1109/TIP.2003.819861).
- [103] Y.-W. Wen, R. Chan, and T. Zeng. *Primal-dual algorithms for total variation based image restoration under Poisson noise*. *Sci. China Math* 56 (2013), 1–20. DOI: [10.1007/s11425-015-5079-0](https://doi.org/10.1007/s11425-015-5079-0).

